



Available online at www.sciencedirect.com

ScienceDirect

Comput. Methods Appl. Mech. Engrg. 314 (2017) 345–407

**Computer methods
in applied
mechanics and
engineering**

www.elsevier.com/locate/cma

Integrated Heart—Coupling multiscale and multiphysics models for the simulation of the cardiac function

Alfio Quarteroni^{a,b}, Toni Lassila^{a,c}, Simone Rossi^{a,d}, Ricardo Ruiz-Baier^{a,e,*}

^a Modelling and Scientific Computing, MATHICSE, École Polytechnique Fédérale de Lausanne, CH-1015 Lausanne, Switzerland

^b MOX - Modellistica e Calcolo Scientifico, Dipartimento di Matematica "F. Brioschi", Politecnico di Milano, via Bonardi 9, 20133 Milano, Italy¹

^c Center for Computational Imaging & Simulation Technologies in Biomedicine, University of Sheffield, Pam Liversidge Building, Mappin Street, Sheffield S1 3JD, United Kingdom²

^d Civil & Environmental Engineering, Mechanical Engineering & Material Science, Duke University, Durham, NC, USA³

^e Mathematical Institute, University of Oxford, A. Wiles Building, Radcliffe Observatory Quarter, Woodstock Road, Oxford OX2 6GG, United Kingdom⁴

Available online 6 June 2016

Abstract

Mathematical modeling of the human heart and its function can expand our understanding of various cardiac diseases, which remain the most common cause of death in the developed world. Like other physiological systems, the heart can be understood as a complex multiscale system involving interacting phenomena at the molecular, cellular, tissue, and organ levels. This article addresses the numerical modeling of many aspects of heart function, including the interaction of the cardiac electrophysiology system with contractile muscle tissue, the sub-cellular activation–contraction mechanisms, as well as the hemodynamics inside the heart chambers. Resolution of each of these sub-systems requires separate mathematical analysis and specially developed numerical algorithms, which we review in detail. By using specific sub-systems as examples, we also look at systemic stability, and explain for example how physiological concepts such as microscopic force generation in cardiac muscle cells, translate to coupled systems of differential equations, and how their stability properties influence the choice of numerical coupling algorithms. Several numerical examples illustrate three fundamental challenges of developing multiphysics and multiscale numerical models for simulating heart function, namely: (i) the correct upscaling from single-cell models to the entire cardiac muscle, (ii) the proper coupling of electrophysiology and tissue mechanics to simulate electromechanical feedback, and (iii) the stable simulation of ventricular hemodynamics during rapid valve opening and closure.

© 2016 Elsevier B.V. All rights reserved.

MSC: 65M60; 92C10; 76Z05; 35K57; 74F10; 74F25

Keywords: Coupling of multiphysics and multiscale models; Electrophysiology; Nonlinear elasticity; Navier–Stokes equations; Finite element methods; Simulation of cardiac diseases

* Corresponding author at: Mathematical Institute, University of Oxford, A. Wiles Building, Radcliffe Observatory Quarter, Woodstock Road, Oxford OX2 6GG, United Kingdom.

E-mail addresses: alfio.quarteroni@epfl.ch (A. Quarteroni), t.lassila@sheffield.ac.uk (T. Lassila), simone.rossi@duke.edu (S. Rossi), ruizbaier@maths.ox.ac.uk (R. Ruiz-Baier).

¹ On leave.

² Present address.

³ Present address.

⁴ Present address.

1. Introduction

Cardiovascular diseases represent one of the most important problems in public health, affecting millions of people each year (the World Health Organization, cf. <http://www.who.int>, gave an estimate of 17.5 million deaths in 2012). Advancing the experimental, theoretical, and computational understanding of the main processes of cardiac function can be of great help in the development and improvement of novel therapies and prognostic methods. However, many aspects of modeling cardiac function are of extreme complexity and a number of difficulties (including e.g. the mismatch of model parameters and spatio-temporal scales, associated to the extremely tough task of retrieving *in vivo* measurements from the tissue) arise when trying to simulate their joint behavior as a coupled multiphysics and multiscale problem (see e.g. [1]). Advances in the fields of experimental and theoretical biology, physics, mathematics and computer science have constantly contributed to an increasing level of details available for modeling and simulating cardiac processes to the extent that a comprehensive description at the full level of details is practically impossible. At the moment, many cardiac modeling studies at the whole heart level are still restricted to simulating particular components, such as, e.g., the electrophysiology or the electromechanics.

Nevertheless, there is increasing interest in multiphysics modeling of more complete cardiac processes, including also the effect of fluid dynamics and the blood-pumping function. A number of fully coupled electro-mechano-fluidic ventricle models [2,3] that incorporate highly detailed mechanical contraction models [4], crossbridge dynamics, and the interaction between the ventricles and the atria [5], have surfaced in recent years. While many of these “heart simulators” are constructed for the purposes of training cardiologists rather than performing clinically relevant studies, full-heart models are increasingly being targeted at patient-specific simulations by adding several degrees of personalization [6–8]. A coupled multiphysics model for total heart function could for example be used to study how a pathology in the electrical conduction system of the heart, e.g. a left bundle branch block, delays the mechanical contraction of the ventricles and influences the ejection pattern of blood. In order to realize this goal, more efficient parallel algorithms and solvers are constantly being developed, but also the issue of stable and efficient multiphysics coupling needs to be addressed.

The physiological function of the heart can be summarized as follows: an electrical potential propagates across the membrane of the heart muscle cells (cardiomyocytes) and induces complex biochemical reactions inside the cytosol that release calcium from the sarcoplasmic reticulum, resulting in the generation of force within the sarcomeres (the basic contractile units within cardiac muscle cells), and finally causing the individual cells to contract and the muscle to deform. The contraction of the muscle yields a rapid increase of pressure inside the ventricular cavities, which allows the heart valves to open and close in careful sequence and induces the periodic filling and ejection of blood from the ventricles and the atria (see further details in [9,10]). This physiological process is intrinsically of multiscale nature and so are the equations that govern each sub-mechanism. As a matter of fact, models describing ion channels on the cell membrane and the excitation–contraction mechanism are typically systems of ODEs to be solved for each individual cell (length scales of μm) and can have time scales of 10^{-4} ms. Fluid dynamics and solid mechanics of the tissue at the organ level (length scales of cm) are nonlinear partial-differential equations of either parabolic or parabolic–hyperbolic type with time scales of 0.1 ms.

Not only the different scales involved but also the type of coupling (strong vs. weak) that exists between the different sub-systems drives the choice of the best computational algorithm. A common choice for multiphysics coupling is to use loosely coupled algorithms, where each sub-system is simulated individually with its own internal time-step using a solver strategy specialized for that particular sub-problem. Then, information is exchanged through the coupling conditions at the interface, and the algorithm proceeds to the next time step. This approach can be computationally and implementationally attractive, but often suffers from instabilities when the sub-systems are strongly coupled. Its counterpart is the tightly coupled approach, where the sequential solutions of the sub-systems are iterated until sufficient coupling tolerance is achieved. This leads to the most stable algorithms in strongly coupled multiphysics problems, but the number of sub-iterations needed tends to make the parallelization of such algorithms inefficient. Finally, in the monolithic approach one attempts to solve the entire coupled system using Newton-type algorithms, but then considerable complexities arise when trying to implement the Jacobian computation for realistic models or when the sub-problems exhibit widely varying time scales. Despite the growing literature devoted to experimental and computational research of the different sub-systems of heart function (see e.g. the review papers [11,4,12]), there do not currently exist many computational simulators of total heart function that are able to incorporate together all the features (electrophysiology, tissue mechanics, fluid mechanics). We believe the aforementioned reasons are behind this.

The aim of this work is to present an integrated heart model to study the interaction between four basic fields related to the heart function: the ion–cell–muscle electrophysiological behavior, the sub-cellular activation mechanism, the deformation of the tissue, and the ventricular fluid mechanics. In order to tackle this problem with reasonable computational cost, several simplifying assumptions will be applied to each component of the coupled model, whilst still being able to draw some conclusions related to the dominant features of the problem. Most of the models used to describe the various sub-systems are not new; the reader is also provided an extensive list of references to past literature on the models used.

Outline

We have attempted to make our presentation useful for both the lay-mathematician without a background in cardiac physiology as well as the bio-engineer without an extensive background in numerical analysis. With that in mind, we have made the sections somewhat self-contained to allow the reader to skip certain sections whose content they are already familiar with, or which go too deep for their interests.

This work is organized as follows: Section 2 contains an introduction to concepts of cardiac physiology, including the basic constituents of the heart tissue and the main aspects of cardiac function. Readers intimately familiar with the function of the human cardiac physiology may freely skip this section. Section 3 describes in detail models used for the different sub-systems of the heart that together constitute the full integrated model. The reader can choose whether to read each sub-section or only the ones that are most relevant to his/her own interests, skimming over the others. In Section 4 a brief overview of mathematical results found in literature concerning well-posedness and existence of the equations for cardiac models is provided. This section is mainly for the interest of the mathematician and can be skipped by the bio-engineer. Next, Section 5 addresses ways of coupling together the different sub-systems to arrive at the coupled cardiac multiphysics problem, and a review of different algorithmic strategies is presented. Again, the reader with no interest in implementing his or her own cardiac multiphysics solver may skip this section. In Section 6 we provide some illustrative examples to show how the different sub-problems are discretized and solved in practice. These include studying the effect of spatial discretization on the discrete propagation velocity in electrophysiology, the application of prestress in cardiac mechanics simulations, the definition of rule-based fiber and sheet directions, the enforcement of isovolumic phases and the effect of increasing the preload in electromechanics simulations, the modeling of fluid dynamics in the left ventricle (LV) by including a simplified implementation of valve opening and closure using lumped parameter models, and finally the electromechanics simulation of the full biventricular human heart in a pathological left bundle branch block -case. All the solvers are implemented in the open source finite element library LifeV (www.lifev.org). Finally, the key challenges and future trends in whole-heart cardiac modeling are summarized in Section 7.

2. Overview of cardiac physiology

The human heart is a four-chambered muscular organ that drives the circulatory system. Its function is to maintain a constant supply of oxygenated blood through the systemic arteries and into the organs (systemic circulation), while simultaneously recycling the deoxygenated blood returning through the systemic veins into the lungs (pulmonary circulation) to be reoxygenated. This task is accomplished efficiently through a complex regulatory system that varies the cardiac output in response to experienced changes in the physiological conditions such as stress, physical exercise, and illness. The regular human heart maintains a pace of roughly 60–100 beats per minute and achieves a cardiac output between 5–6 litres of blood per minute for healthy adults. The highly specialized muscle tissue of the heart does not grow tired under stress, unlike skeletal muscle in the limbs, but requires a constant supply of oxygen itself and is easily damaged (infarcted) if the supply of oxygen is even temporarily reduced. Until recently it was believed that cardiac muscle cells did not get regrow after tissue damage, but recent studies have shown that some amount of regeneration (roughly 1% of the total volume per year) can take place [13].

The most important components of the human heart are the two main chambers called *ventricles* and the two antechambers called the *atria*. The heart is divided into two sides, *left heart* and *right heart*, where the right heart pumps deoxygenated blood into the pulmonary circulation, while the left heart pumps oxygenated blood into the systemic circulation. Both sides act in synchronized fashion. Both atria contract almost simultaneously and are responsible for the complete filling of the ventricles, which contract after a delay of roughly 120 ms and perform

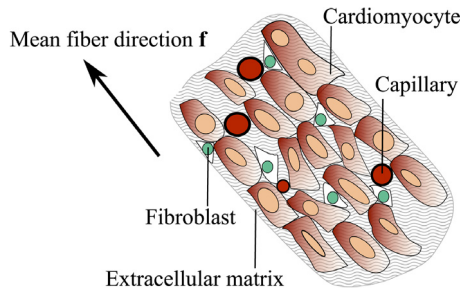


Fig. 2.1. Schematic representation of the arrangement of cardiomyocytes in the extracellular matrix synthesized by the fibroblasts. The cardiomyocytes are locally arranged in linear arrays with similar orientation. A network of capillaries perfuses the cardiomyocytes.
Source: Adapted from [14].

the main pumping function necessary to circulate the blood through the body. The ventricles and atria are electrically isolated from each other by the *fibrous skeleton* that provides some additional structure and prevents the electrical potential of one set of chambers from entering the other ones except through the *atrioventricular node*. In addition to the four chambers, the heart connects to the root of the *aorta* (large artery through which blood enters the systemic circulation), two *venae cavae* (large veins through which blood returns from the systemic circulation), *pulmonary arteries* and *pulmonary veins* (through which the blood enters and exits the pulmonary circulation), four heart valves (*pulmonary, tricuspid, mitral, and aortic*) that regulate the flow between the chambers and between the latter and the pulmonary artery/aorta, *coronary arteries* and *coronary veins* (responsible for oxygenating the heart muscle itself), and the *pericardium* (a double-layered membranous sac that surrounds the heart and damps its motion relative to the sternum and the other organs) [10].

2.1. Structure and mechanical function of cardiac tissue

The majority of cardiac tissue volume is occupied by *cardiomyocytes*. These are striated muscle cells specialized for the function of the heart. The cardiomyocytes are joined to one another in linear arrays by intercalated discs. Like all muscle cells they are excitable cells (see [9]). The gap junctions between individual cardiomyocytes permit an electrical potential to travel on the cellular membranes from cell to cell similarly if slightly more slowly than in other cells, such as nerve cells. Muscle cells are embedded in a fibrous extracellular matrix formed mainly of collagen protein that is constantly synthesized by cardiac *fibroblast cells*. These are the most numerous cells in the heart tissue and their task is to remodel the extracellular matrix in response to mechanical strain and external damage. Together they give rise to a fiber-reinforced structure where the cardiomyocytes are arranged in layers of laminar sheetlets. In addition, cardiac tissue contains vascular *smooth muscle cells* in the intramyocardial coronary arterioles and venules, *Purkinje fibers* that deliver the electrical signal from the ventricles' natural pacemaker to the muscle, and *endothelial cells* on the inner surface of the heart called the endocardium. A thin layer of connective tissue and fat, called epicardium, covers the exterior surface of the heart. Moreover, there exists a network of cardiomyocytes joined by intercalated discs, called cardiac syncytium (and divided between an atrial and a ventricular syncytium) that allows the fast propagation of electrical impulses, together with a synchronous contraction of the tissue and cells [9]. A schematic arrangement of myocardial cells is shown in Fig. 2.1. We use the word *fibers* to indicate the organization of the myocardial cells, which can be idealized as cylindrical objects with radius about a tenth of their longitudinal extension. Their longitudinal shape and the fact that adjacent cells tend to be oriented in roughly the same direction allows us to define the local orientation of the cells, the fiber direction. In most computational models individual cells are beyond the computational resolution, and therefore, in the following, the fibers direction must be understood as the average myocardial cells orientation in a sufficiently small control volume. As in any muscle, the direction along which fibers are aligned defines both the passive and active mechanical properties of the tissue.

Although the complex muscular architecture of the ventricles has been studied for centuries, only in the last fifty years has a comprehensive description of the macroscopic morphological structure of the cardiac muscle emerged. Torrent-Guasp [15,16] conjectured that both ventricles are formed by a single band of fibers, the Ventricular Myocardial Band (VMB), twisted into a helicoidal configuration with two spiral turns. Measurements of Streeter [17] showed a transmural variation of the fiber direction ranging from about -70° in the short-axis plane at the outer

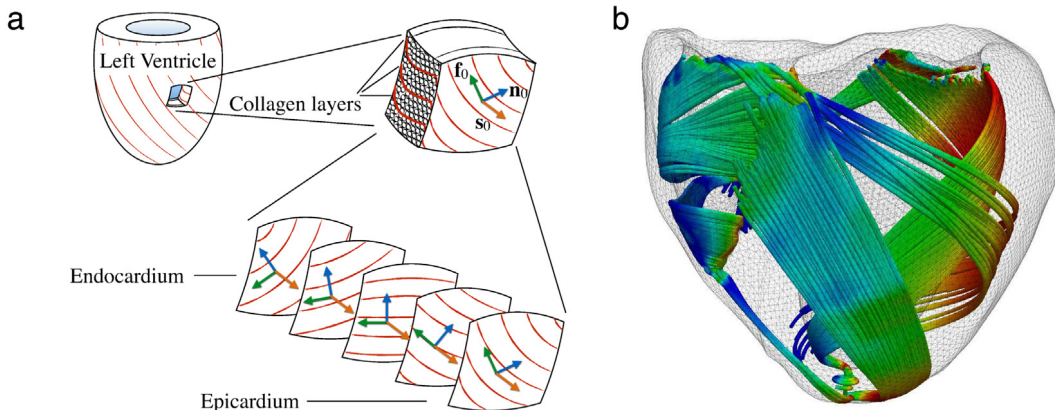


Fig. 2.2. (a) Schematic depiction of the transmural configuration of the muscle fibers and laminar sheets. (b) Rule-based fiber structure generated on a human biventricular geometry. The three orthogonal directions f_0 , s_0 , n_0 represent the local alignment of fibers, sheets and the cross-fiber (or sheet-normal) directions.

ventricular surface, the epicardium, to approximately $+80^\circ$ at the inner part of the wall, the endocardium. Idealizing the LV as a truncated prolate ellipsoid, it is possible to define analytically a fiber orientation [18,19]; the angles defined in this way can be optimized to represent more closely experimental data. Following the hypotheses that fibers follow geodesic paths on toroidal surfaces within the ventricular wall [17], Peskin defined a mathematical theory in which fibers orientation is described by approximate geodesics [20]. A different approach has been recently used in [21] where, following the VMB concept, the LV was described as a set of identical spiral surfaces defined as mappings of a half disc. The agreement of this rule-based description of the left ventricular anisotropy with experimental data from Streeter, mathematically supports the VMB theory proposed by Torrent-Guasp. Due to the fibers' configuration in the ventricles, a longitudinal (apex-to-base) shortening of about 15% from the diastolic configuration of the ventricles is experienced during contraction, while the LV wall thickens more than 30%. Moreover, their architecture greatly influences both the physiological and pathological electrical properties of the heart as it affects the local electrical conductivities and the excitation patterns. The importance of such an anisotropy is now well recognized and it is also supported by diffusion-tensor magnetic resonance imaging (DTMRI) [22].

The description of the ventricles by means of only the fiber orientation is not complete. In the last twenty years, strong evidence has been reported [23] showing a laminar structure of the myocardium. The muscle can be seen as an arrangement of myolaminae approximately four cells thick grouped together by perimysial collagen, as schematically shown in Fig. 2.2(a). In each of these laminae the myocytes are connected with each other and embedded in a skeleton of endomysial collagen, while cells in different laminae are not directly connected and therefore only loosely coupled. These laminar structures strongly influence the mechanical and electrical properties of the tissue and can be modeled as a locally orthotropic material, i.e. as exhibiting two or three orthogonal axes of rotational symmetry along which different mechanical properties are experienced in each preferred direction of deformation.

2.2. Electrophysiology and the rhythmic excitation of the heart

Cardiac pacing is driven by the sinoatrial node (located at the right atrium of the heart), a natural pacemaker that discharges electrical signals into the heart's conduction system at varying periods of pacing depending on the level of blood flow required to supply oxygen to the organs. These signals travel through the atria into the atrioventricular node, where a brief delay permits the atria to contract first before the signal enters the ventricular fast conduction system through the left and right bundle branches, finally traveling through the specialized conduction network (highly conductive specialized muscle cells) and junctions into the ventricular muscles. In the cardiac muscle the electrical potential travels more slowly along the cell membranes, opening voltage-sensitive protein channels (see Fig. 2.3) and allowing positively charged ions to enter the cells, causing them to become depolarized.

Once the entire muscle has been depolarized from its resting potential a slow process of repolarization begins, after which the muscle is ready to contract again. The normal sinus rhythm is sketched in Fig. 2.4(a).

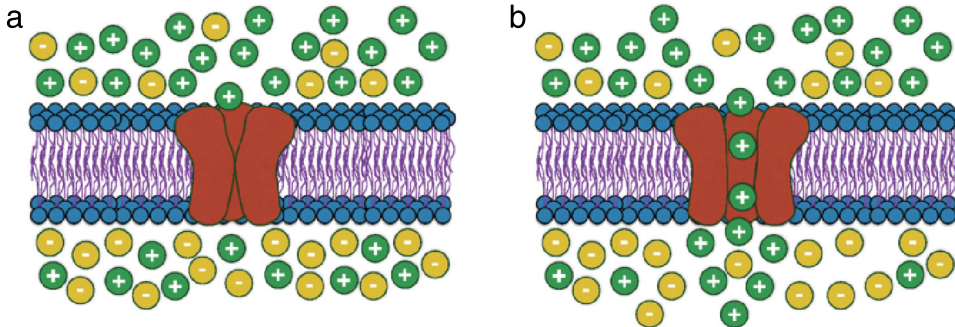


Fig. 2.3. Sketch of cellular membrane surrounded by ionic solution at different concentrations on each side. On the cellular membrane, specialized proteins act like channels for selected ionic species. The opening of such channel typically depends on the transmembrane voltage, but it can also depend on other factors, such as mechanical stretching. (a) The channel is closed and ions cannot pass through the membrane. (b) The channel is open and only specific ions can pass through the membrane.

Since the pumping of the heart is supposed to happen roughly at constant periodic rate, the cardiomyocytes enter a refractory period after the initial rapid depolarization during which no additional excitation can occur in order to avoid entering into an uncontrolled spurious contraction–relaxation pattern (fibrillation itself, and other complex states involving irregular rhythmic behavior, such as period doubling bifurcation or ectopic beats [24]). Because of that, the action potential duration (the period between the initial depolarization and the final repolarization) has to depend on the cardiac interval, following the so-called restitution curve that can be calibrated from experimental data (see Fig. 2.4(b)). This kind of plots show the relationship between the duration of a cardiac action potential and the length of the diastolic interval preceding it [10,25]. Besides the variable-period refractoriness of the cells, the timing of cardiac contraction is driven by the conduction velocity on the cell membranes and the general pattern of activation, both of which depend on the microstructure of the cells and the surrounding collagen matrix. An improper activation pattern can cause inefficient contraction and possibly alter the stability of the dynamical system by introducing stable quasi-periodic wavefronts or even chaotic fibrillation.

2.3. Sub-cellular tension generation mechanisms

Muscular contraction is a sub-cellular process initiated by the increase of intracellular calcium due to the opening of voltage-gated ion channels. Cardiomyocytes have a regular structure made of myofibrils, rod-like protein structures divided into basic contractile units called sarcomeres (see Fig. 2.5). The sarcomeres consist of two different kinds of long protein filaments, thin and thick filaments, that can attach to each other at certain binding sites. When a depolarization of the intracellular space increases the concentration of intracellular calcium, it triggers the release of cytosolic calcium stored in the sarcoplasmic reticulum, leading to the binding of Ca^{2+} with troponin-C, and finally the binding of myosin heads to the actin filaments. This is called the crossbridge mechanism that causes the filaments to slide against each other, leading to subsequent contraction of the sarcomeres (and consequently the entire cell). The crossbridge kinetics can be simulated by using a Monte Carlo method where the interaction of only a small number of molecules is considered [26]. A different approach, first proposed by Huxley [27], consists in writing a partial differential equation describing the evolution of the binding probabilities. At the organ level, both approaches are too expensive to be used, and therefore different solutions strategies have been proposed. Typically, the mean-field hypothesis is added to the Huxley model assuming that the interaction between actin and myosin can be described by one crossbridge representative of the whole distribution [28–31]. This assumption reduces the Huxley model to a set of inexpensive ordinary differential equations. Another method used to reduce the complexity of the system averages the distribution of crossbridges over a single cell [32]. For a more detailed description and discussion we refer the reader to [33].

2.4. Mechanical pumping function and dynamics of blood

The main mechanical function of the heart is the pumping of blood in the arteries. A major role in this is played by the atrioventricular valves that regulate the direction of the blood flow and, when simultaneously closed together with the semilunar valves, allow sufficient blood pressure to build up inside the ventricles during the isovolumic phase in

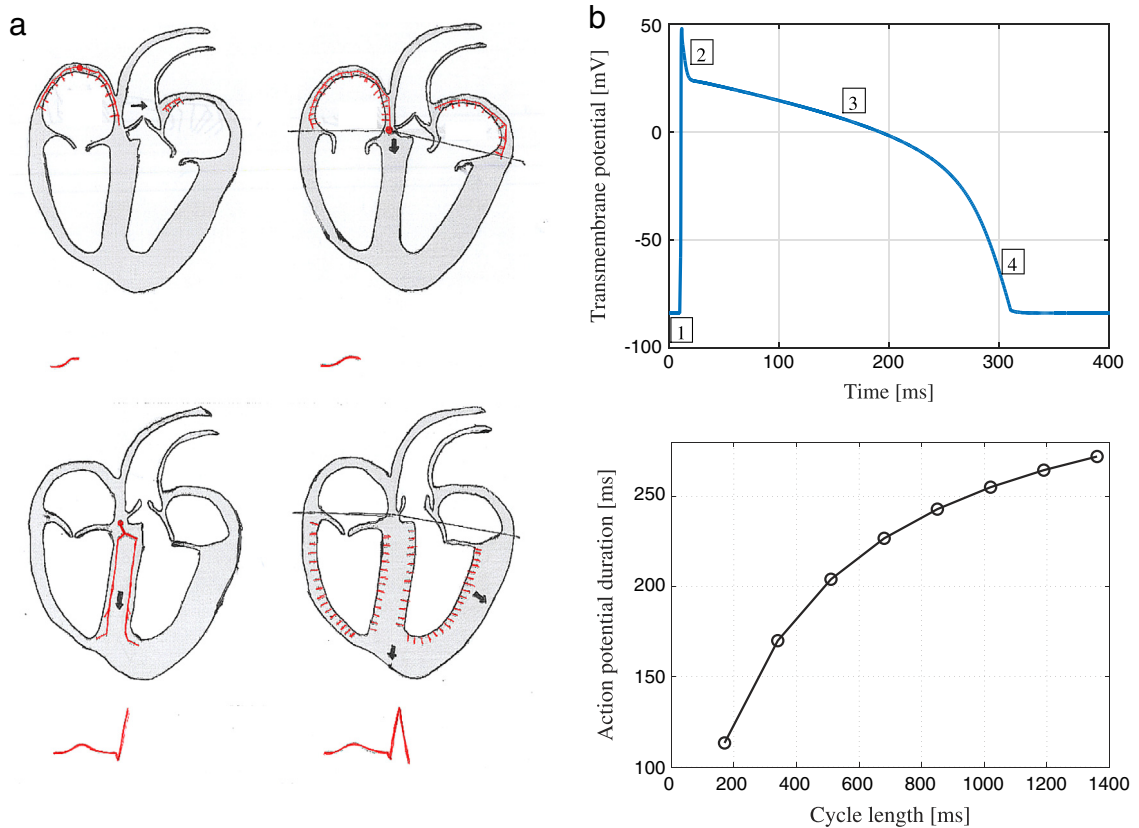


Fig. 2.4. (a) Phases of normal sinus rhythm. Activation starts from the sinoatrial node (top left), travels along both atria and reaches the atrioventricular node (top right), enters into the left and right bundle branches (bottom left) and finally into the myocardium through the Purkinje network (bottom right). Corresponding phases of the electrocardiogram depicted; (b) On top: Typical form of the action potential for ventricular cardiomyocytes. At rest the cellular membrane is polarized, with a positive ion concentration on the outside. When the signal excites the cell (1), the cell membrane undergoes an abrupt depolarization, where sodium ions enter the cell. This triggers the opening of certain channels allowing potassium to start moving out to the extracellular space, forming an early repolarization phase (2). Then, a plateau phase (3) takes place, where a complex Calcium kinetics slows down the repolarization and during which the cardiomyocyte contracts. After contraction (4), a final repolarization brings back the cellular membrane to its resting condition. Bottom: The typical restitution curve describing the dependence of action potential duration, that is the time between the initial depolarization and the final repolarization, on the cycle length of stimulation.

order to pump blood all the way to the extremities. Dysfunction of the heart valves (either regurgitation due to structural damage to the valve, or improper opening of the valve due to calcification of the leaflets) typically leads to either volume overload or pressure overload in one of the chambers. While the heart can successfully compensate for deviations from physiological pressure/stress conditions by both pumping harder and increasing the stiffness of the fibrous extracellular matrix (cardiac hypertrophy), in the long term such mechanisms can lead to heart failure unless treated.

There is a long-standing discussion on the physiological effects of hemodynamics on cardiac mechanical function. It is often stated [34] that ventricular contraction optimizes the swirling flow from an energetic point-of-view, allowing the muscle to perform the minimal work necessary to pump a fixed volume of blood. However, recent simulation studies have partially disproven this theory by indicating that the dissipation of the diastolic vortex has a negligible effect on the pumping function of the heart [35,36].

2.5. Spatial and temporal multiscale aspects of cardiac function

From molecular mechanisms to body functionality, each component of the heart function is strongly connected with biochemical and mechanical processes lying on highly dispersed spatial and temporal scales (see Fig. 2.6). A comprehensive understanding of the main multiscale properties of the heart physiology is therefore essential to achieve a successful modeling of the involved, intrinsically multiscale phenomena. For instance, over long

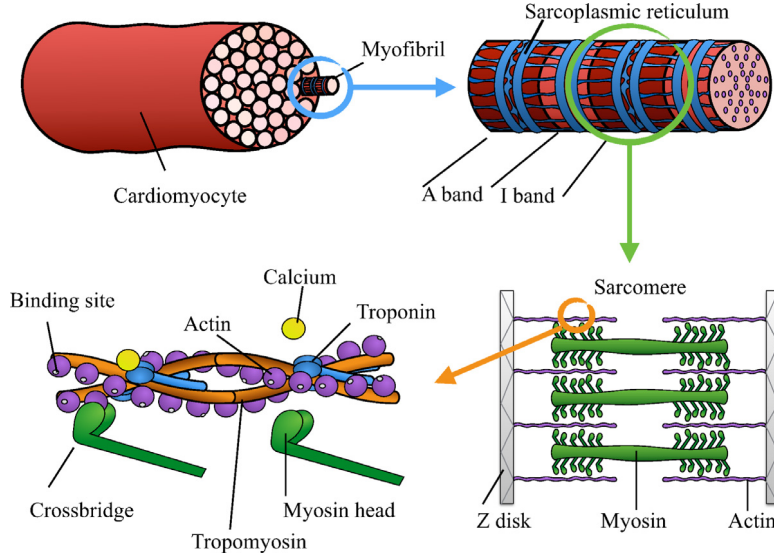


Fig. 2.5. Schematic representation of the cardiac cell contractile structure. Each cardiomyocyte is composed by myofibrils, long tubular structures surrounded by sarcoplasmic reticulum. Each myofibril has a regular structure, made of light and dark bands. In the A band the thick myosin protein and the thin actin protein overlap and the band looks darker than the I band where only actin is present. The A band is located at the center of the sarcomere, the cellular contractile unit. Each sarcomere is delimited by the Z disks on which actin is anchored. Between the thin actin filaments we find the thick myosin filaments. During electrical excitation, intracellular Calcium concentration increases, triggering the release of more Calcium ions stored in the sarcoplasmic reticulum. The released Calcium ions bind to Troponin forcing a change of configuration of Tropomyosin which exposes the binding sites. Then, myosin heads can bind to actin and generate a sliding motion between the two filaments. This sliding brings the Z disk closer to each other resulting in cellular contraction.

spatio-temporal scales, classical homogenization techniques have proven very helpful in describing the dynamics of electrophysiological tissue properties, however over smaller scales, the same approaches may lead to meaningless information. Other processes (such as heart tissue biomechanics or ventricular flow properties) and other multiscale representation approaches (including simple aggregating of responses from one scale to another or smoothing techniques) will fail if not designed carefully.

Some features of the multiscale nature of the heart function are shared by other related biological systems, as e.g. tissue growth: one of the main challenges resides in connecting macroscopic tissue level descriptions with classical sub-cellular models (in this respect, see the review [37]). Recent studies focusing on translating specific effects across spatio-temporal scales also include arrhythmia and cardiac alternans [33,38], or contraction mechanisms [39,40].

3. Mathematical models for individual cardiac subsystems

In view of setting up appropriate mathematical models for the components of cardiac functionality, we start by introducing some needed mathematical notation. Our multiphysics problem is set up on three bounded sub-domains of \mathbb{R}^3 : Ω_E , Ω_S , and Ω_F . The region Ω_E is the one in which we solve the electrophysiology sub-problem, the solid mechanics problem is solved on Ω_S , and the fluid dynamics sub-problem on Ω_F . We denote their boundaries by Γ_E , Γ_S , and Γ_F , respectively. In an abstract setting, we make the assumptions that $\Omega_E \subset \Omega_S$ (electrical activity takes place at least in some part of the deforming tissue such as ventricular wall), and that $(\overline{\Omega_S} \cap \overline{\Omega_F}) \subset (\Gamma_S \cap \Gamma_F)$ and $\overline{\Omega_S} \cap \overline{\Omega_F} \neq \emptyset$ (the fluid and solid domains are disjoint but their boundaries share a common nonempty part). The domains Ω_E and Ω_S differ if one regards the aortic root, pulmonary artery, or valves as part of deforming tissue where the propagation of electrical impulse may be discarded. By Γ_I we denote the fluid–solid interface $\partial\Omega_F \cap \partial\Omega_S$, and by \mathbf{n}_F , \mathbf{n}_S the outward unit normal direction of the fluid and solid domain boundaries, respectively. Fig. 3.1 provides a sketch of the three domains and their position with respect to the full heart geometry.

All three computational domains are moving during the cardiac cycle, independently of the given frame of reference. Here either a Lagrangian (for the solid and the electrophysiology) or an arbitrary Lagrangian–Eulerian (for the fluid) frame of reference can be adopted. Other approaches have also been proposed, for instance the immersed

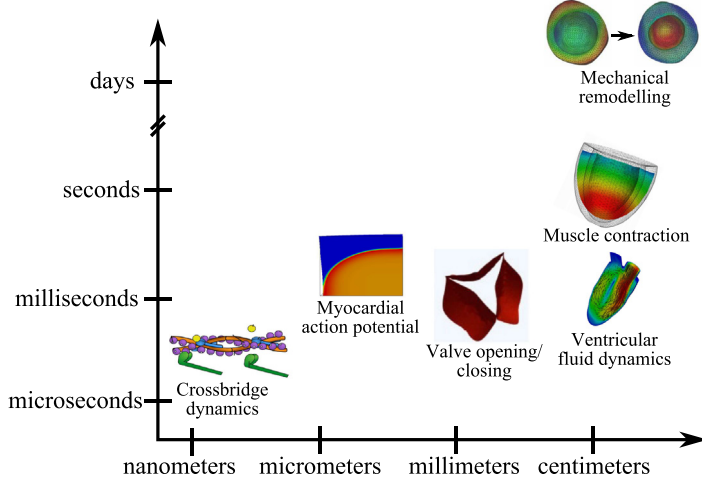


Fig. 2.6. Spatial scales (horizontal axis) and temporal scales (vertical axis) of mechanisms contributing to heart function. Some or all of these mechanisms may be coupled together in a total heart function model. Mechanical remodeling provides an example of a long-term biomechanical response mechanism to excessive loading conditions and occurs at time scales far above the others.

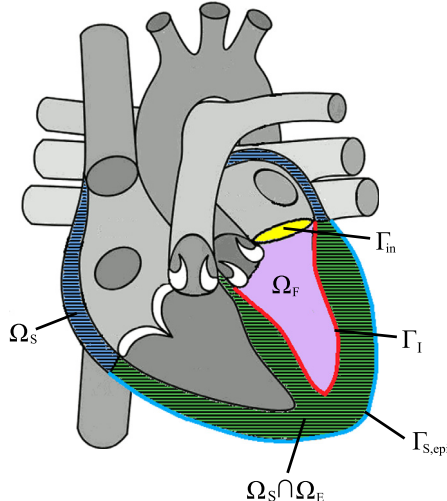


Fig. 3.1. The three computational domains (fluid domain Ω_F , solid mechanics domain Ω_S , electrophysiology domain Ω_E) considered in the cardiac multiphysics problem. In this example the electrophysiology problem is only considered in the ventricles, whereas the solid mechanics problem covers also the atria. Also pictured are the fluid–structure interface Γ_I inside the LV, the epicardial surface $\Gamma_{S,epi}$, and the mitral valve inlet surface Γ_{in} . See also Eqs. (3.23)–(3.25). In the sketch the domains Ω_E and Ω_S overlap within the ventricular part of the heart.

boundary (IB) method developed in [41] (see also [42]) for the modeling of cardiac mechanics and ventricular fluid dynamics.

For the sake of clarity, superscripts 0 and t will denote quantities in the reference configuration and current configuration at time t , respectively. By \mathbf{x}^t we denote the current position of a material particle of Ω^t that was originally placed at \mathbf{x}^0 in the reference configuration Ω^0 of a given domain. The solid body motion is defined using the smooth one-to-one map $\phi_S : \Omega_S^0 \rightarrow \Omega_S^t$, $\phi_S(\mathbf{x}^0) = \mathbf{x}^0 + \mathbf{d}_S(\mathbf{x}^0)$, where \mathbf{d}_S denotes the displacement vector $\mathbf{d}_S = \mathbf{x}^t - \mathbf{x}^0$. We denote by \mathbf{F} the deformation gradient tensor associated to the motion ϕ_S , whereas $\mathbf{C} = \mathbf{F}^T \mathbf{F}$ stands for the right Cauchy–Green strain tensor. By $J = \det \mathbf{F}$ we denote the solid volume map and the first isotropic invariant is $I_1(\mathbf{C}) = \text{tr } \mathbf{C}$. For a generic unitary vector \mathbf{f}_0 , the scalar $I_{4,f}(\mathbf{C}) = \mathbf{f}_0 \cdot (\mathbf{C} \mathbf{f}_0)$ denotes a direction-dependent pseudo-invariant of \mathbf{C} representing the stretch of the solid Ω_S along the direction \mathbf{f}_0 .

In the following sections we state the equations governing the different processes of the heart function; the electrophysiology, the excitation–contraction mechanism, the passive tissue mechanics, and the ventricular fluid

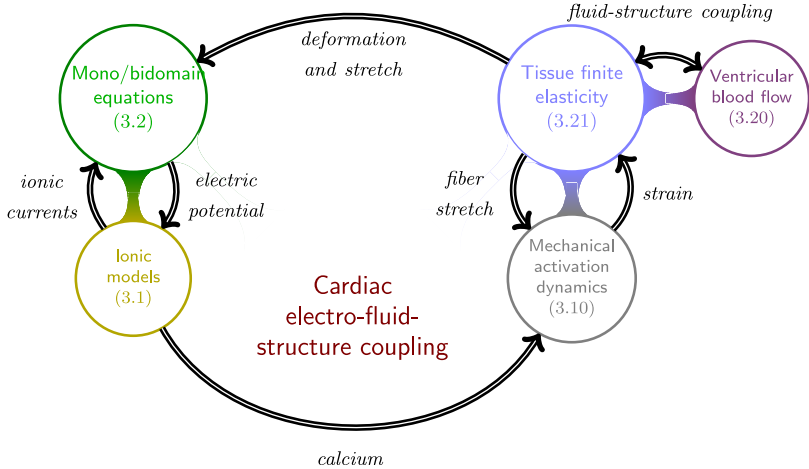


Fig. 3.2. Sketch of the proposed cardiac electro-fluid–structure coupling strategy. The references point to the governing equations of each sub-system.

dynamics of blood. Full details on the specific derivations of the models are omitted; the interested reader is directed to bibliographic references when appropriate. We limit the discussion on physiological and clinical aspects to the most important physiological features that are relevant when considering the choice models for individual sub-systems (and their coupling). These are summarized in Fig. 3.2.

3.1. Electrophysiology of the heart

Mathematical and computational models of cardiac electrophysiology have increased our understanding of arrhythmias mechanisms [43] and they have been used for diagnosis and interventions, both pharmacological and non-pharmacological. The cellular models are typically based on systems of ordinary differential equations that express conservation of current. Their general form reads [44]

$$\begin{cases} C_m \frac{dv}{dt} + i_{\text{ion}}(v, w, c) = i_{\text{app}}(t), \\ i_{\text{ion}}(v, w, c) = \sum_{k=1}^P g_k(c) \prod_{j=1}^M w_j^{p_{jk}} (v - v_k(c)) + I_0(v, c), \\ \frac{dw}{dt} = m_w(v, w, c), \quad \frac{dc}{dt} = m_c(v, w, c). \end{cases} \quad (3.1)$$

Here v denotes the local transmembrane potential between the intra- and the extra-cellular fluid, C_m is the local membrane capacitance, i_{app} is the applied external current; the ionic currents follow a Hodgkin–Huxley-type description for P different ionic species with v_k being the Nernst (or resting) potential of the k th ionic species; finally, w_j , with $j \in \{1, \dots, M\}$ are M so-called *gating variables* taking values in $[0, 1]$ that regulate the transmembrane currents and the intracellular concentrations $c = (c_k)_{k=1}^P$ of the P different ionic species. Many detailed membrane models for various species and types of cells can be found in literature and have been extensively validated in experiments at the single-cell level. Their suitability for the whole-heart simulation varies wildly. Concerning their numerical solution, a study on the choice of the time-stepping strategy was performed in [45], where it was found that most physiologically detailed membrane models are extremely stiff. This makes them difficult to use in organ-level simulations due to the need for a fully implicit time integration scheme [46,47]. In general, the best compromise between computational efficiency and clinical relevance of models has been obtained by considering simplifications of realistic cell models by first eliminating some internal variables to reduce the stiffness of the system [48,49], then treating only the potential v and the gating variables w implicitly (e.g. the Rush–Larsen scheme [50]).

All membrane models address cell excitation isolated from the rest of the cardiac function. At the macroscopic tissue level, the spatial counterpart of these models can be written after a homogenization procedure, leading to

so-called bidomain equations written in terms of the intra- and extracellular potentials v_i, v_e , respectively:

$$\begin{aligned}\chi C_m (\partial_t v + i_{\text{ion}}(v, \mathbf{w}, \mathbf{c})) - \nabla \cdot (\mathbf{D}_i \nabla v_i) &= \chi i_{\text{app}}^i(t), \\ \chi C_m (\partial_t v + i_{\text{ion}}(v, \mathbf{w}, \mathbf{c})) + \nabla \cdot (\mathbf{D}_e \nabla v_i) &= \chi i_{\text{app}}^e(t),\end{aligned}$$

that are coupled to the kinetic equations for the gating variables and ionic species. We recall that $v = v_i - v_e$ and $i_{\text{app}}^i, i_{\text{app}}^e$ stand for applied stimuli on the intra- and extracellular spaces, respectively. A less involved model is given by the classical *monodomain system*, where current conservation is written only in terms of the transmembrane potential (but is not able to describe repolarization patterns). In the reference undeformed domain, the equations – representing propagation of the membrane depolarization through the muscle – read:

$$\begin{cases} \chi [C_m \partial_t v + i_{\text{ion}}(v, \mathbf{w}, \mathbf{c}) - i_{\text{app}}(t)] = \frac{1}{J} \nabla \cdot (\mathbf{D}_0 \nabla v) & \text{in } \Omega_E^0 \times (0, T], \\ \frac{d\mathbf{w}}{dt} = m_w(v, \mathbf{w}, \mathbf{c}) & \text{in } \Omega_E^0 \times (0, T], \\ \frac{d\mathbf{c}}{dt} = m_c(v, \mathbf{w}, \mathbf{c}) & \text{in } \Omega_E^0 \times (0, T]. \end{cases} \quad (3.2)$$

Here \mathbf{D}_0 is the conductivity tensor (defined in a fixed reference state), χ is the ratio of membrane area per tissue volume and J is the determinant of the deformation gradient tensor (see Section 3.2). The monodomain approximation relies on the assumptions that cardiac tissue is a continuum and consists only of myocytes and extracellular space. It can also arise after assuming that the difference in conductivities inside and outside the cell membrane is negligible. See a detailed description in e.g. [51], and for a review of other possible modeling assumptions for cardiac electrophysiology we refer to [52].

Supposing that the tissue is electrically isolated from the surrounding matrix, zero-flux boundary conditions are applied on the whole boundary for the transmembrane voltage v :

$$\mathbf{F}^{-1} \mathbf{D} \mathbf{F}^{-T} \nabla v \cdot \mathbf{n}_S = 0 \quad \text{on } \partial \Omega_E^0 \times (0, T],$$

where \mathbf{D} denotes the conductivity tensor associated to the spatial configuration (see further details in Section 3.5).

Given that our study focuses on the analysis of muscle contraction and blood ejection, we will restrict ourselves to the phenomenological model of the human ventricular action potential from Bueno-Orovio et al. [53]. The model is able to reproduce most of the experimental quantities, e.g. restitution curves, conduction velocity, spiral dynamics, and alternans. The ionic currents consist of three general terms without particularization to the ionic species that carry them

$$i_{\text{ion}}(v, \mathbf{w}) = i_{\text{ion}}^{\text{fi}}(v, \mathbf{w}) + i_{\text{ion}}^{\text{si}}(v, \mathbf{w}) + i_{\text{ion}}^{\text{so}}(v, \mathbf{w}),$$

where the adimensional *fast inward*, *slow inward* and *slow outward* currents are respectively given by

$$\begin{aligned}\chi i_{\text{ion}}^{\text{fi}}(v, \mathbf{w}) &= -w_1 H(v - \theta_1)(v - \theta_1)(v_v - v)/\tau_{fi}, \\ \chi i_{\text{ion}}^{\text{si}}(v, \mathbf{w}) &= -H(v - \theta_2)w_2 w_3/\tau_{si}, \\ \chi i_{\text{ion}}^{\text{so}}(v, \mathbf{w}) &= (v - v_0)(1 - H(v - \theta_2))/\tau_o + H(v - \theta_2)/\tau_{so},\end{aligned}$$

and the kinetics of the gating variables w are given by

$$m_w(v, \mathbf{w}) = \begin{pmatrix} (1 - H(v - \theta_1))(w_{1,\text{inf}} - w_1)/\tau_1^- - H(v - \theta_1)w_1/\tau_1^+ \\ (1 - H(v - \theta_2))(w_{2,\text{inf}} - w_2)/\tau_2^- - H(v - \theta_2)w_2/\tau_2^+ \\ ((1 + \tanh(k_3(v - v_3)))/2 - w_3)/\tau_3 \end{pmatrix}.$$

Here H is the Heaviside function, and the time constants and infinite values are defined as:

$$\begin{aligned}\tau_1^- &= (1 - H(v - \theta_1^-))\tau_{1,1}^- + H(v - \theta_1^-)\tau_{1,2}^-, \quad \tau_2^- = \tau_{2,1}^- + (\tau_{2,2}^- - \tau_{2,1}^-)(1 + \tanh(k_2^-(v - v_2^-)))/2 \\ \tau_{so} &= \tau_{so,1} + (\tau_{so,2} - \tau_{so,1})(1 + \tanh(k_{so}(v - v_{so})))/2 \\ \tau_3 &= ((1 - H(v - \theta_2))\tau_{3,1}) + H(v - \theta_2)\tau_{3,2}, \quad \tau_o = ((1 - H(v - \theta_0))\tau_{o,1} + H(v - \theta_0)\tau_{o,2} \\ w_{1,\text{inf}} &= \begin{cases} 1, & v < \theta_1^- \\ 0, & u \geq \theta_1^+ \end{cases} \quad w_{2,\text{inf}} = ((1 - H(v - \theta_0))(1 - v/\tau_{2,\infty}) + H(v - \theta_0)w_{2,\infty}^*\end{aligned}$$

Model parameters were chosen in [53] to reproduce action potential (AP) shapes similar to that of the popular ten Tusscher–Panfilov model [49]. In addition to the features mentioned above, the flexibility of this “minimal model” is such that it can also be fitted to reproduce the reported AP shape changes in pathological conduction scenarios, such as ischemia [54]. It has also been used to fit experimental data of thermo-electrical coupling and bifurcation phenomena and to simulate tissue size effects [55,56]. Its main limitation is that it does not explicitly model the calcium dynamics that drives the generation of force by the crossbridges inside the sarcomeres. It is, however, mildly stiff, enabling time steps up to 0.01 ms to be used. As was done in [57], we use the variable w_3 as a surrogate for the intracellular calcium concentration.

In addition to these models, it is possible to exploit information of the Purkinje network to increase the accuracy of time-dependent boundary conditions at the endocardium (see e.g. [58,59]). We also mention the models including fractional diffusion and other nonlinear extensions to (3.2) introduced in [33,60,61].

3.2. Passive hyperelastic material models for cardiac tissue

In addition to the active force generation by the excitation–contraction model, we need to consider also the passive mechanical response of the tissue. The equations of motion for the cardiac tissue read

$$\rho_S \partial_t \mathbf{u}_S - \nabla \cdot \boldsymbol{\sigma}_S = \mathbf{0}, \quad \text{in } \Omega_S \times (0, T], \quad (3.3)$$

where boundary and initial conditions must be specified. Here ρ_S is deformation-dependent density of the tissue, \mathbf{u}_S is the velocity and $\boldsymbol{\sigma}_S$ is the Cauchy stress tensor. Although experimental studies indicate that the passive myocardium has viscoelastic effects and exhibits hysteresis even under moderate loads,⁵ the usual assumption considers only the quasistatic behavior. Therefore, it is possible to describe the tissue as hyperelastic. By typical thermodynamical considerations, the stress tensor is then obtained by differentiating a pseudo-strain energy \mathcal{W} with respect to strain. Another typical assumption is to consider the myocardium to be nearly incompressible under physiological loads, whereas in practice the volume of cardiac tissue is strongly driven by the perfusion of blood from the coronaries and its volume can vary as much as 7% during systolic contraction [63]. Usually the following simpler quasistatic problem is considered at each time iteration

$$-\nabla \cdot \boldsymbol{\sigma}_S = \mathbf{0}, \quad \text{in } \Omega_S, \quad (3.4)$$

with normal stress boundary conditions on the endocardium, and Robin-type boundary conditions everywhere else, except at the base. A commonly used boundary condition constrains the ventricles at the basal cut plane: such conditions stiffen the ventricular contraction/relaxation and create non-physiological deformation patterns. A more conservative choice constrains only the normal component of the displacement on the base of the ventricle.

Even though transversely isotropic or even fully isotropic materials have been proposed for modeling the constitutive behavior of the myocardium [64,65], it is by now well-accepted that orthotropic material models need to be incorporated in more realistic mechanical models of cardiac tissue. For the examples shown in Section 6, we employ the orthotropic Holzapfel–Ogden constitutive law [66], which extends several other nonlinear material models available from the literature. The elastic strain energy function is formulated in terms of the invariants of the right Cauchy–Green tensor $\mathbf{C} = \mathbf{F}^T \mathbf{F}$ and their isochoric counterparts, denoted with bars

$$\begin{cases} J = \det(\mathbf{F}) \\ I_1 = \text{tr}(\mathbf{C}), & \bar{I}_1 = J^{-2/3} I_1 \\ I_{4,f} = \mathbf{C} \mathbf{f}_0 \cdot \mathbf{f}_0, & \bar{I}_{4,f} = J^{-2/3} I_{4,f} \\ I_{4,s} = \mathbf{C} \mathbf{s}_0 \cdot \mathbf{s}_0, & \bar{I}_{4,s} = J^{-2/3} I_{4,s} \\ I_{8,f_s} = \mathbf{C} \mathbf{f}_0 \cdot \mathbf{s}_0, & \bar{I}_{8,f_s} = J^{-2/3} I_{8,f_s} \end{cases}$$

and is divided into three parts—the isotropic isochoric part, the isotropic volumetric part, and the orthotropic part:

$$\begin{aligned} \mathcal{W}(\mathbf{F}) = & \frac{a}{2b} \exp(b[\bar{I}_1 - 3]) + \frac{\kappa}{4}[(J - 1)^2 + (\ln J)^2] \\ & + \sum_{i=f,s} \frac{a_i}{2b_i} [\exp(b_i(\bar{I}_{4,i} - 1)^2) - 1] + \frac{a_{f_s}}{2b_{f_s}} [\exp(b_{f_s} \bar{I}_{8,f_s}^2) - 1], \end{aligned} \quad (3.5)$$

⁵ Viscoelastic behavior stems from the fact that the myocardium has roughly 76% of fluid content [62].

where the material parameters $a, a_f, a_s, a_{fs}, b, b_f, b_s, b_{fs}$ are experimentally fitted. The parameter κ is the bulk modulus that penalizes local volume changes in order to enforce incompressibility of the tissue. The notation $\langle x \rangle = \frac{1}{2}(x + |x|)$ indicates the positive part of x and is used on the two terms depending on the orthotropic invariants $\bar{I}_{4,f}$ and $\bar{I}_{4,s}$ in order to deactivate their contribution to the strain energy under compression. This prevents unphysical buckling-type phenomena from creating an ambiguity in the solution [66] (see also more recent contributions supporting the study of fiber stability in terms of statistical description of $\bar{I}_{4,f}$, e.g. [67–69]). Decomposition (3.5) for orthotropic fiber-reinforced materials is somewhat controversial as it can lead to unphysical spherical deformations under pure hydrostatic loads [70] or undesired volume growth during uniaxial tension [71]. In our experience, this issue can be mitigated by enforcing a large enough bulk modulus κ .

The incorporation of the microscopic active processes into the structural properties at the tissue level is a key aspect in the multiscale framework of the cardiac function. Here we adopt an *active strain* approach following [72–75], where one assumes a multiplicative decomposition of the solid deformation gradient as $\mathbf{F} = \mathbf{F}_E \mathbf{F}_A$, where \mathbf{F}_A is the active deformation induced by the contraction of the myofibrils in the reference configuration, and \mathbf{F}_E is the passive elastic deformation of the tissue in the fictitious intermediate configuration. Assuming incompressibility of the total deformation, $\det \mathbf{F} = 1$, and that of the passive elastic deformation, $\det \mathbf{F}_E = 1$, one can define a macroscopic active deformation using three scalar fields $\gamma_f, \gamma_s, \gamma_n$ that characterize locally the deformations along the three orthogonal directions $\mathbf{f}_0, \mathbf{s}_0, \mathbf{n}_0$ representing the local alignment of fibers, fiber sheets and the cross-fiber (or sheet-normal) directions. This yields a local active deformation gradient written in the general form

$$\mathbf{F}_A = \mathbf{I} + \gamma_f \mathbf{f}_0 \otimes \mathbf{f}_0 + \gamma_s \mathbf{s}_0 \otimes \mathbf{s}_0 + \gamma_n \mathbf{n}_0 \otimes \mathbf{n}_0, \quad (3.6)$$

for which our assumptions lead to local incompressibility also at the level of the active deformations, that is $\det \mathbf{F}_A = 1$.

To derive the total stress tensor including both the passive and active stress contributions, the strain energy function (3.5) is written in an intermediate virtual configuration

$$\widehat{\mathcal{W}} = \mathcal{W}(\mathbf{F}_E) = \mathcal{W}(\mathbf{F}\mathbf{F}_A^{-1}) \quad (3.7)$$

(see further details in Section 3.4), and by differentiating with respect to the strain \mathbf{F} the following general form for the Piola–Kirchhoff stress tensor is obtained:

$$\mathbf{P} = J\boldsymbol{\sigma}_S \mathbf{F}^{-T} = \frac{\partial \widehat{\mathcal{W}}}{\partial \mathbf{F}} = \mathcal{W}_1 \frac{\partial \bar{I}_1^E}{\partial \mathbf{F}} + \mathcal{W}_{4,f} \frac{\partial \bar{I}_{4,f}^E}{\partial \mathbf{F}} + \mathcal{W}_{4,s} \frac{\partial \bar{I}_{4,s}^E}{\partial \mathbf{F}} + \mathcal{W}_{8,fs} \frac{\partial \bar{I}_{8,fs}^E}{\partial \mathbf{F}}, \quad (3.8)$$

where the stored energy contributions to each stress term are given by

$$\begin{cases} \mathcal{W}_1 = \frac{a}{2} \exp(b[\bar{I}_1^E - 3]), \\ \mathcal{W}_{4,i} = a_i \langle \bar{I}_{4,i}^E - 1 \rangle [\exp(b_i \langle \bar{I}_{4,i}^E - 1 \rangle^2) - 1], \\ \mathcal{W}_{8,fs} = a_{fs} \bar{I}_{8,fs}^E [\exp(b_{fs} \bar{I}_{8,fs}^2) - 1], \end{cases}$$

for $i \in \{s, f\}$, and the invariants $\bar{I}_1^E, \bar{I}_{4,i}^E, \bar{I}_{8,fs}^E$ on the intermediate configuration depend on the particular choice of active strain model (see (3.6), above) and need to be explicitly derived by pulling back to the reference configuration and writing them in terms of the original invariants. We refer the reader to [76] for the specific formulas, but note that in general the first invariant on the intermediate configuration depends not only on the first invariant on the reference configuration, but on all the others as well

$$\bar{I}_1^E = \bar{I}_1^E(\bar{I}_1, \bar{I}_{4,f}, \bar{I}_{4,s}, \gamma_f),$$

and similarly for all the other invariants. This means that in the orthotropic active strain formulation the active contribution does not act only in the fiber directions, but also appears in the isotropic and isochoric part of the stress tensor. This makes its implementation slightly more involved, as existing passive mechanics solvers cannot be trivially modified by just adding the necessary terms.

3.3. Microscopic force generation in the sarcomeres

Our goal is to capture the essential aspects that drive the contraction of the cardiac muscle starting from the sarcomere level. We focus on the phenomenological excitation–contraction model introduced in [57], which does not specifically describes the kinetics of the crossbridges, but does include sarcomere length-dependency which is key for reproducing the well-known Frank–Starling effect of increased force generation under increased preloading (see e.g. [77]). In our model the active contraction of individual cells depends on the ionic concentrations c and on the local deformation gradient invariant $I_{4,f}$ in the myofiber direction (see Section 3.2 for its definition):

$$\partial_t \gamma_f - a(c, \gamma_f, I_{4,f}) = 0 \quad \text{in } \Omega_S^0 \times (0, T]. \quad (3.9)$$

The variable γ_f represents the strain in the myofiber direction induced by the contraction of single cardiomyocytes, that is, we consider an *active strain* formulation. More specifically, we assume the following form for (3.9):

$$\begin{cases} \partial_t \gamma_f = \frac{1}{\eta_A} \left[\left(\frac{\partial \mathcal{W}_A}{\partial I_1^E} + \frac{\partial \mathcal{W}_A}{\partial I_{4,f}^E} \right) \left(\hat{F}_A(c, I_{4,f}) - \frac{2I_{4,f}}{(1 + \gamma_f)^3} \right) - \frac{\partial \mathcal{W}_A}{\partial \mathbf{F}_A} : f_0 \otimes f_0 \right] \\ \hat{F}_A(c, I_{4,f}) = \alpha f(c) R_{F-L}(I_{4,f}), \end{cases} \quad (3.10)$$

where the \mathcal{W}_A is the *active* component of the free energy, and \mathbf{F}_A is the active deformation, precisely defined in Section 3.4. We realize that (3.10) can be derived by imposing irreversibility of the mechanical contraction by means of the second law of thermodynamics, under the assumption that the free energy can be decomposed into passive and active contributions: $\mathcal{W} = \mathcal{W}_P + \mathcal{W}_A$. In the following, we will assume the purely passive contribution to be negligible, setting $\mathcal{W}_P = 0$, and therefore make no distinction between \mathcal{W}_A and \mathcal{W} (see Section 3.2 for additional details). Although other choices for the definition of \mathcal{W}_P and \mathcal{W}_A are possible, see for example [78,79], we prefer the simplest case $\mathcal{W}_P = 0$. In fact \mathcal{W}_P represents the fraction of the tissue that cannot be mechanically activated. Setting $\mathcal{W}_P = 0$, the contribution to the passive behavior of the material is given only by the term \mathcal{W}_A . In fact, when the mechanical activation switches off, $\gamma_f = 0$, $\mathbf{F}_A = \mathbf{I}$, $\mathbf{F}_E = \mathbf{F}$ and the energy \mathcal{W}_A in (3.7) is exactly the underlying passive constitutive law.

The force \hat{F}_A represents the active tension generated within the sarcomeres, and it drives the macroscopic muscular contraction. While \hat{F}_A should be defined by some crossbridge model, we assume an empirical form for this force such that it depends on some ionic concentration (typically calcium) through the function $f(c)$. We also introduce the relationship between the generated force and the sarcomere elongation through the function R_{F-L} , as defined in [80], with α being a positive parameter. This smooth function is basically a fitting of observed sarcomere force–length relations. Derivation details of this formulation are provided in [57].

3.4. Excitation–contraction coupling

The main factor behind the ability of the heart to adapt itself to different physiological operating conditions is the Frank–Starling law: increasing the ventricular pre-load will increase the amount of force generated by the cardiac muscle. This provides a direct link between macroscopic stretch and the amount of microscopic force generated by the binding of crossbridges in the form of a force–length relationship. In our specific model (3.10) the microscopic active tension takes the form

$$\hat{F}_A(c, I_{4,f}) = \alpha f(c) R_{F-L}(I_{4,f}),$$

where the function $R_{F-L}(I_{4,f})$ represents the force–length relationship of intact cardiac cells (it is generally fitted from experimental data, e.g. from [81]) and $f(c)$ specifies the amount of force generated by the crossbridges in response to intracellular calcium release.

In addition to the force–length relationship, any muscle cell should follow Hill's relation [82]

$$(\hat{F}_A(t) + a)(v(t) + b) = \text{constant}, \quad (3.11)$$

where $\hat{F}_A(t)$ is the instantaneous force generated and $v(t)$ the velocity of contraction. The force–velocity relation was originally derived for isotonic macroscopic muscle contraction. Nevertheless, it is equally valid for microscopic

muscle fibers and the macroscopic contraction velocity $v(t)$ becomes the relative sliding velocity of the two filaments inside the sarcomere. In this case (of microscopic fibers), a constitutive relation linking the macroscopic strain and the microscopic sarcomere sliding velocity needs to be specified for example by assuming that the sarcomere rate-of-strain depends on the macroscopic strain, $v = v(I_{4,f})$, through some additional constitutive model, e.g. the Hill–Maxwell rheological model [83].

Moreover, we recall that the cell-level evolution law (3.9) for γ_f controls the rate of activation and relaxation of local strains and it uses calcium to link different scales (see also [84]). These kinetics need to be combined with additional constitutive relations to account for the cross-fiber deformation γ_n , whereas the sheet deformation γ_s can be determined, for instance, after the incompressibility relation $(1 + \gamma_s)(1 + \gamma_f)(1 + \gamma_n) = 1$. Experimental strain measurements on in vivo animals have shown that cardiac tissue contracts also in the cross-fiber direction, whereas large positive strains (thickening) are observed only in the transmural direction of the fiber sheets [85]. These considerations suggest that the active cross-fiber strains can be assumed proportional to the active fiber strains, $\gamma_n = \kappa \gamma_f$, where $\kappa > 0$ is a factor to be fitted according to experimental strain measurements.

3.5. Mechano-electric feedback

Like all muscle cells, cardiomyocytes are sensitive to mechanical stretch. Stretching a cell changes the shape of its membrane as well as the distance of the gap junctions between the cells, leading to changes in the ion channels and the conductivity of the action potential from cell to cell. This can be modeled in its simplest form by altering the first equation of (3.2) to become

$$\chi C_m \partial_t v - \frac{1}{J} \nabla \cdot (J \mathbf{F}^{-1} \mathbf{D} \mathbf{F}^{-T} \nabla v) + \chi [i_{\text{ion}}(v, \mathbf{w}, \mathbf{c}) + i_{\text{SAC}}(v, \mathbf{F})] = \chi i_{\text{app}}(t) \quad \text{in } \Omega_E^0 \times (0, T], \quad (3.12)$$

where an explicit dependence on the solid deformation tensor \mathbf{F} has entered in the conductivity tensor (accounting for the geometric feedback due to deformation of tissue structure) as well as an additional ionic current i_{SAC} (stretch-activated channels). The stretch-activated channels induce an additional inward current that adds to the depolarization in the form

$$i_{\text{SAC}}(v, \mathbf{F}) = g \left(\sqrt{I_{4,f}(\mathbf{F})} - 1 \right) (v - E), \quad (3.13)$$

where E and g are the reversal potential and the maximal conductance of the channels. This term becomes active only when positive strains are observed ($I_{4,f} \geq 1$). The effect of stretch-activated channels on cardiac action potential was studied in [86], where flattening of the restitution curve and lengthening of the action potential duration were among the effects observed. The importance of the stretch-activated channels in mechanically induced spiral-wave break-up was highlighted in [87] and was believed to be mainly due to stretch-induced conduction blocks giving rise to termination of spiral waves (see the seminal work [73]). If the goal is to study e.g. the termination of arrhythmias it is therefore necessary to consider the mechano-electric feedback, including the stretch-activated channels. In fact, as shown for example in [88,89], vulnerability to atrial fibrillation increases in acute atrial stretch and the block of SACs has been proposed to treat arrhythmias under elevated atrial pressure.

In addition to the physical mechano-electric feedback, Eq. (3.12) already shows a geometrical coupling which modifies the conductivity tensor. In general, we can define the conductivity tensor \mathbf{D}_0 in the reference configuration which is related to the current material configuration through the transformation

$$\mathbf{D}_0 = J \mathbf{F}^{-1} \mathbf{D} \mathbf{F}^{-T}, \quad (3.14)$$

where \mathbf{D} represents the spatial conductivity tensor. In computational models of cardiac electrophysiology where the domain is fixed, the conductivity tensor can be defined as

$$\mathbf{D} = \sigma_{f,X} \mathbf{f}_X \otimes \mathbf{f}_X + \sigma_{s,X} \mathbf{s}_X \otimes \mathbf{s}_X + \sigma_{n,X} \mathbf{n}_X \otimes \mathbf{n}_X, \quad (3.15)$$

where $\sigma_{f,X}$, $\sigma_{s,X}$ and $\sigma_{n,X}$ are the conductivities in the directions longitudinal and transversal to the mean myofiber direction \mathbf{f}_X . In (3.15) we used the subscript X to refer to the fixed configuration. When the electromechanical coupling is considered, it is necessary to understand in which configuration the conductivity coefficients are measured, as such

definition will greatly impact the conduction velocity in the reference and current configurations. In fact, assuming that in the reference configuration

$$\mathbf{D}_0 = \sigma_{f,0} \mathbf{f}_0 \otimes \mathbf{f}_0 + \sigma_{s,0} \mathbf{s}_0 \otimes \mathbf{s}_0 + \sigma_{n,0} \mathbf{n}_0 \otimes \mathbf{n}_0, \quad (3.16)$$

we obtain by a push forward operation to spatial coordinates,

$$\mathbf{D} = \sigma_f \mathbf{f} \otimes \mathbf{f} + \sigma_s \mathbf{s} \otimes \mathbf{s} + \sigma_n \mathbf{n} \otimes \mathbf{n}. \quad (3.17)$$

By direct comparison between (3.15) and (3.17), it is possible to identify $\sigma_{m,X} = J^{-1} I_{4,m} \sigma_{m,0}$, for $m = f, s, n$, and $\{\mathbf{f}_X, \mathbf{s}_X, \mathbf{n}_X\} = \left\{ \frac{\mathbf{f}}{\|\mathbf{f}\|}, \frac{\mathbf{s}}{\|\mathbf{s}\|}, \frac{\mathbf{n}}{\|\mathbf{n}\|} \right\}$. On the other hand, more commonly, it is assumed that $\sigma_{m,X} = \sigma_{m,0}$, for $m = f, s, n$, and $\{\mathbf{f}_X, \mathbf{s}_X, \mathbf{n}_X\} = \{\mathbf{f}_0, \mathbf{s}_0, \mathbf{n}_0\}$. This assumption implies that the conduction velocity will remain constant in the current material configuration (while decreasing in the reference configuration). In this case, for example, the observed activation times will tend to increase when the ventricle expands under increased volume loading.

To further clarify this point consider the following example: a single incompressible cylindrical fiber of length L_0 is pulled uniformly in its longitudinal direction to reach the length L , so that the associated deformation gradient tensor reads

$$\mathbf{F} = \frac{1}{\sqrt{\lambda}} \mathbf{I} + \left(\lambda - \frac{1}{\sqrt{\lambda}} \right) \mathbf{f}_0 \otimes \mathbf{f}_0,$$

where $\lambda = L/L_0$. For simplicity, let us also assume $\sigma_{s,0} = \sigma_{n,0}$, such that Eq. (3.16) can be written as

$$\mathbf{D}_0 = \sigma_{s,0} \mathbf{I} + (\sigma_{f,0} - \sigma_{s,0}) \mathbf{f}_0 \otimes \mathbf{f}_0. \quad (3.18)$$

Introducing the time T , as the time taken by the traveling pulse to travel along the cell in its longitudinal direction, we can define the conduction velocities in the reference and deformed configurations as $v_{f,0} = L_0/T$ and $v_f = L/T = L_0/T\lambda = v_{0,f}\lambda$. Since the longitudinal conduction velocity in material coordinates is proportional to $\sqrt{\sigma_{f,0}}$, the conduction velocity in the deformed frame v_f is proportional to $\sqrt{\sigma_{f,0}}\lambda$. In other words, the conduction velocity in the reference configuration is constant, while the one in the spatial configuration increases with the stretch. On the other hand, assuming

$$\mathbf{D} = \sigma_{s,0} \mathbf{I} + (\sigma_{f,0} - \sigma_{s,0}) \mathbf{f}_0 \otimes \mathbf{f}_0, \quad (3.19)$$

the reference conductivity tensor can be found by applying the pull-back (3.14):

$$\mathbf{D}_0 = \lambda \sigma_{s,0} \mathbf{I} + \left(\frac{\sigma_{f,0}}{\lambda^2} - \lambda \sigma_{f,0} \right) \mathbf{f}_0 \otimes \mathbf{f}_0.$$

In this case, the conduction velocity in the longitudinal direction in the reference configuration $v_{f,0}$ is proportional to the inverse of the stretch, that is $v_{f,0} \propto \sqrt{\sigma_{f,0}}/\lambda$. On the other hand, in the deformed configuration, the conduction velocity will not depend on the stretch as it is proportional only to $\sqrt{\sigma_{f,0}}$.

There is a long-standing debate about the behavior of the conduction velocity when cardiac tissue is mechanically stretched. Some experimental studies indicate an increase in the conduction velocity on cardiac Purkinje cells [90], while others report a decreased conduction velocity due to increased stretch in the epicardial cells [91], atrial cells [92], and myocardial cells [93]. The latter study attributed the altered conduction velocity to a reduction of inter-cellular resistance with a concurrent increase of effective membrane capacitance. It is also known that sufficiently large tissue stretch will lead to a total conduction block. In addition, the porous nature of the myocardial tissue will also have an influence on the conduction velocity, even in the absence of contraction (see e.g. [60,61]).

3.6. Ventricular fluid–structure interaction

Within the physiological regime, blood behaves as a mildly non-Newtonian fluid in the ventricles. Ventricular flow is indeed laminar but strongly vortical for large parts of the cardiac cycle, except during peak diastolic filling when transition to turbulence can occur as Reynolds numbers in the range 1500–2500 are reached. This explains why the Navier–Stokes equations (NSE) in a moving domain represent the most popular mathematical model used to describe ventricular hemodynamics. Since in the context of ventricular fluid–structure interaction neither small displacement

nor thin-wall assumptions hold, the only feasible formulations of the problem fall roughly in two categories: ones using a moving mesh approach with an Arbitrary Lagrangian–Eulerian (ALE) formulation to account for the domain velocity in the NSE [94–96,4,97,8,3], and those using the immersed boundary (IB) method [98,2] or related level-set based approaches [6]. The latter two approaches are known to be more convenient in that the moving ventricular wall does not need to be explicitly tracked and no remeshing needs to be performed even in the case of large displacements. In the seminal work of Peskin [41,42], a Cartesian mesh not necessarily conforming with the muscle geometry was used and the fluid patterns can be described as an effect of the motion of the immersed boundary and involving both Eulerian and Lagrangian variables coupled via a regular approximation of the Dirac delta function. In contrast, the ALE approach is more traditional and thus easier to implement, but requires dealing with large mesh deformations that are especially problematic if the motion of the valve leaflets needs to be captured.

In some computational studies the mutual interaction of the hemodynamics with the myocardial solid mechanics is also taken into account. This typically leads to considering a coupled fluid–structure interaction formulation. Tissue mechanics can play two roles in the fluid–structure interaction formulation. They can be considered in the passive sense only, in order to capture the physiological pressure–volume (PV) relation [94,99] to estimate the passive stresses experienced by the myocardium during diastolic filling. Alternatively, the full cycle of contraction and relaxation can be modeled by including an activated mechanics model for the myocardium [4,8].

The quantities solved for in a typical ventricular FSI model are the fluid velocity \mathbf{u}_F , the fluid pressure p_F , and the displacement of the solid \mathbf{d}_S . The fluid problem consists in the Navier–Stokes equations written in ALE formulation:

$$\begin{aligned} \rho_F (\partial_t \mathbf{u}_F|_{x^0} + (\mathbf{u}_F - \tilde{\mathbf{w}}_F) \cdot \nabla \mathbf{u}_F) - \nabla \cdot \boldsymbol{\sigma}_F &= \mathbf{0} \quad \text{in } \Omega_F^t \times (0, T], \\ \nabla \cdot \mathbf{u}_F &= 0 \quad \text{in } \Omega_F^t \times (0, T], \\ \mathbf{u}_F &= \bar{\mathbf{u}}_F \quad \text{in } \Omega_F^t, \quad t = 0. \end{aligned} \quad (3.20)$$

Here $\boldsymbol{\sigma}_F = 2\mu_F \boldsymbol{\epsilon}(\mathbf{u}_F)$ is the fluid Cauchy stress tensor, where $\boldsymbol{\epsilon}(\mathbf{v}) = \frac{1}{2}(\nabla \mathbf{v} + \nabla \mathbf{v}^T)$ is the symmetric part of the gradient of a vector field \mathbf{v} , μ_F , ρ_F are the fluid viscosity and density, respectively, $\bar{\mathbf{u}}_F$ is the initial velocity of the fluid, and $\tilde{\mathbf{w}}_F$ is the fluid domain velocity determined by an ALE map $\phi_F : \Omega_F^0 \rightarrow \Omega_F^t$, $x^0 \mapsto \phi_F(x^0) = x^0 + \mathbf{d}_F(x^0)$, satisfying $\Omega_F^t = \phi_F(\Omega_F^0)$.

The elastodynamic problem in the Lagrangian reference configuration can be written as

$$\begin{aligned} \rho_S \partial_{tt} \mathbf{d}_S - \nabla \cdot \boldsymbol{\sigma}_S &= \mathbf{0} \quad \text{in } \Omega_S^0 \times (0, T], \\ \mathbf{d}_S &= \bar{\mathbf{d}}_S \quad \text{in } \Omega_S^0, \quad t = 0, \\ \partial_t \mathbf{d}_S &= \bar{\mathbf{u}}_S \quad \text{in } \Omega_S^0, \quad t = 0, \end{aligned} \quad (3.21)$$

where ρ_S is the solid density, $\boldsymbol{\sigma}_S$ is the solid Cauchy stress and $\bar{\mathbf{d}}_S$, $\bar{\mathbf{u}}_S$ are the initial solid displacement and velocity, respectively. The motion of the fluid domain \mathbf{d}_F is recovered via the harmonic extension of \mathbf{d}_S to the interior of Ω_F^0 , that is,

$$\begin{aligned} -\Delta \mathbf{d}_F &= \mathbf{0} \quad \text{in } \Omega_F^0, \\ \mathbf{d}_F &= \mathbf{d}_S \quad \text{on } \Gamma_I^0, \\ \nabla \mathbf{d}_F \cdot \mathbf{n}_F &= \mathbf{0} \quad \text{on } \partial \Omega_F^0 \setminus \Gamma_I^0. \end{aligned} \quad (3.22)$$

Notice that the specific way $\boldsymbol{\sigma}_S$ relates with deformation and strain energy is characterized by $\boldsymbol{\sigma}_S = \mathbf{P} \mathbf{F}^T$, where \mathbf{P} is given in the constitutive relation (3.8). Also a dependence on the pressure of the solid can be established in case of incompressible materials. See e.g. [96] for further details on this coupled system.

3.7. Fluid–structure coupling and external tissue support

In addition to the geometric adherence condition (3.22)₂ that the fluid and solid domains must be conforming at the interface (equivalent to saying that the ventricles are at all times totally immersed with blood and that the blood does not penetrate into the tissue), the typical coupling conditions for FSI are the no-slip condition on the wall and the

continuity of normal stresses:

$$\begin{aligned} \mathbf{u}_F \circ \boldsymbol{\phi}_F - \partial_t \mathbf{d}_S &= \mathbf{0} \quad \text{on } \Gamma_I^0 \times (0, T], \\ \mathbf{P} \mathbf{n}_S^0 - J(\sigma_F \circ \boldsymbol{\phi}_F) \mathbf{F}^{-T} \mathbf{n}_S^0 &= \mathbf{0} \quad \text{on } \Gamma_I^0 \times (0, T]. \end{aligned} \quad (3.23)$$

The latter arises from the conservation of momentum across the interface, while the former is an extension of the physical no-slip condition of viscous fluids extended to moving walls. The introduction of the time derivative of displacement $\partial_t \mathbf{d}_S$ necessitates the use of inertial terms in the solid mechanics formulation, which turns the (quasi-)static elliptic tangent problem of solid mechanics into the time-dependent hyperbolic system (3.21).

During diastolic filling, when rapid inflow of blood with density ρ_F similar to the density of the solid ρ_S causes a sudden expansion of the ventricular chamber(s), the inertial forces may excite the modes corresponding to purely imaginary eigenvalues of the solid and lead to unphysiological vibration of the ventricle(s). A possible cure is to add some viscous damping either in the solid formulation, say to replace (3.21)₁ with

$$\rho_S \partial_{tt} \mathbf{d}_S + \eta \partial_t \mathbf{d}_S = \nabla \cdot \boldsymbol{\sigma}_S, \quad \text{in } \Omega_S^0 \times (0, T], \quad (3.24)$$

for a suitable positive coefficient η , or in the external boundary conditions in the form of a Robin term with viscous contribution (with constants $\beta_1, \beta_2 > 0$):

$$\beta_1 \mathbf{d}_S + \beta_2 \dot{\mathbf{d}}_S = p_{\text{ext}} \mathbf{n}_S, \quad \text{on } \Gamma_{S,\text{epi}}^0. \quad (3.25)$$

A final aspect of the fluid–solid mechanics coupling that is needed in order to recover the correct global motion of the heart is the incorporation of external tissue support in the model. The real heart is immersed in fluid and loosely supported by a flexible double-layered membrane called the pericardium. This means that enforcement of pointwise constraints and the elimination of rigid modes in the mathematical model will lead to unphysiological deformation modes. The correct physiological motion of the heart includes motion of the atrioventricular plane downwards during systolic contraction accompanied by significant long-axis shortening. Consequently, heart mechanics simulations reported in literature that resort to excessively rigid boundary conditions, such as fixing the atrioventricular plane, cannot recover the physiological contraction pattern of the heart. Spring-like external support enforced e.g. by Robin-type boundary conditions [100] can be tuned to mimic the global motion of the heart, but does not permit sliding contact between the heart and the pericardium. Explicitly solving a pericardium–heart contact problem has also been proposed [101].

3.8. From orifice flow to detailed valve dynamics models

Cardiac flow is controlled by four valves with stiff but compliant leaflets that prevent backflow between the chambers. They dictate both the fluid dynamics and the duration of the two isovolumic phases, and thus need to be considered in any ventricular fluid dynamics model. The mechanism driving the opening of a valve is the existence of a positive pressure difference between two of the chambers. For example, the mitral valve opens when the ventricular myocardium begins to relax during diastole and leads to a rapidly decreasing pressure inside the LV and a positive pressure gradient across the valve itself. The resulting volumetric flow rate $Q(t)$ through the valve can be modeled in the first approximation using the *Bernoulli equation* for orifice flow:

$$Q_{\text{mv}} |Q_{\text{mv}}| = \frac{CA^2}{\rho_F} \delta P, \quad (3.26)$$

where C is a dimensionless constant, $A(t)$ is the effective orifice area that depends on the configuration of the valve leaflets at any given time t , and $\delta P(t)$ is the pressure difference across the mitral valve. A similar model can be used for the aortic valve. It remains to provide a suitable model for the orifice area $A(t)$ to describe the dynamics of the valve leaflets. We identify three basic strategies with which the leaflet opening dynamics can be modeled:

Model A: The classical model for cardiac valves is the ideal diode model, which offers no resistance to the blood flow and opens and closes instantaneously in response to the changing of the pressure gradient sign and flow

direction:

$$Q_{\text{mv}} = \begin{cases} \frac{P_{\text{pv}} - P_{\text{lv}}}{R_{\text{la}}}, & \text{if } P_{\text{pv}} > P_{\text{lv}} \\ 0, & \text{if } P_{\text{pv}} \leq P_{\text{lv}}, \end{cases} \quad (3.27)$$

where P_{pv} and P_{lv} are the pulmonary and LV pressure respectively. This assumption is not entirely unreasonable, given that the biological valves open very rapidly within the time frame of a few milliseconds. Unfortunately, this simple model does not distinguish between healthy and pathological valves. Since this is insufficient to provide a complete set of Dirichlet data for the fluid equations inside the LV, (3.27) is in fact a *defective* boundary condition [102]. As such, condition (3.27) is imposed using Lagrange multipliers, which has the benefit that no explicit velocity profile needs to be imposed at the inflow, see [103]. In order to stabilize the velocity at the mitral valve due to flow reversal effects, the tangential component of the velocity field at the inlet, Γ_{in} has to be further constrained to zero (see [104] and the discussion therein), leading to the inflow boundary condition:

$$\int_{\Gamma_{\text{in}}} \mathbf{u}_F \cdot \mathbf{n}_F d\Gamma = 0, \quad (\mathbf{I} - \mathbf{n}_F \mathbf{n}_F^T) \mathbf{u}_F = \mathbf{0} \quad \text{on } \Gamma_{\text{in}}. \quad (3.28)$$

Model B: Is an extension of Model A that incorporates regurgitation and inertial effects of the valve on the fluid dynamics. In this model the flow rate is given by the Bernoulli's equation for flow through an orifice:

$$P_{\text{pv}} - P_{\text{lv}} = R_{\text{la}} Q_{\text{mv}} + B Q_{\text{mv}} |Q_{\text{mv}}| + L \frac{dQ_{\text{mv}}}{dt} \quad (3.29)$$

where $B = \rho/(2A_{\text{eff}}^2)$ is the Bernoulli resistance of the valve and $L = \rho\ell_{\text{eff}}/A_{\text{eff}}$ the blood inertance. This equation replaces (3.26). The coefficients L and B are determined by the effective orifice area A_{eff} that switches between open and closed valve configurations similarly to the ideal diode case:

$$A_{\text{eff}} = \begin{cases} A_{\text{max}}, & \text{if } P_{\text{pv}} > P_{\text{lv}} \\ A_{\text{min}}, & \text{if } P_{\text{pv}} \leq P_{\text{lv}}. \end{cases} \quad (3.30)$$

For $A_{\text{min}} > 0$ the model allows regurgitation to take place. A numerically stable time discretization is obtained for (3.29) by using the semi-implicit scheme at each Newton iteration k

$$Q_{\text{mv}}^{n,k} = \frac{Q_{\text{mv}}^{n-1} + \frac{\Delta t}{L} (P_{\text{pv}}^{n,k-1} - P_{\text{lv}}^{n,k-1})}{1 + \Delta t B/L |Q_{\text{mv}}^{n-1}|}, \quad \text{for each } k \geq 1, \quad (3.31)$$

where Δt is the timestep and the superscript n refers to the time level $t^n = n\Delta t$, $n \geq 0$. In this model the pressure P_{lv} is imposed as a normal stress boundary condition on the LV fluid problem along with the aforementioned tangential velocity stabilization condition, which now reads

$$\sigma_F \mathbf{n}_F \cdot \mathbf{n}_F = -P_{\text{lv}} \mathbf{n}_F \cdot \mathbf{n}_F \quad \text{on } \Gamma_{\text{in}}, \quad (\mathbf{I} - \mathbf{n}_F \mathbf{n}_F^T) \mathbf{u} = \mathbf{0} \quad \text{on } \Gamma_{\text{in}}. \quad (3.32)$$

Model C: To model more precisely the valve opening dynamics the lumped parameter model proposed in [105] can be used. It prescribes simple and smooth opening and closing dynamics for A_{eff} without explicitly modeling the valve leaflets. In this approach the flow rate through the mitral valve is again given by Bernoulli's equation (3.29) for flow through an orifice, which in turn depends on an internal variable $\zeta \in [0, 1]$ according to

$$A_{\text{eff}}(t) = [A_{\text{max}} - A_{\text{min}}] \zeta(t) + A_{\text{min}}, \quad (3.33)$$

whereas the internal variable evolves according to the rate equation

$$\frac{d\zeta}{dt} = \begin{cases} (1 - \zeta) K_{vo} (P_{\text{la}} - P_{\text{lv}}), & \text{if } P_{\text{la}} \geq P_{\text{lv}} \\ \zeta K_{vc} (P_{\text{la}} - P_{\text{lv}}), & \text{if } P_{\text{la}} \leq P_{\text{lv}}. \end{cases} \quad (3.34)$$

This model captures the valve opening dynamics and represents mitral insufficiency, but does not model the effect of the leaflets on the local flow pattern. The boundary conditions applied on the LV fluid problem are identical to (3.32).

More involved models for valve opening dynamics take into account the time-dependent shape of the aperture of each valve, and they can impose either velocity profiles [4] or pressure profiles [106,7,8], at the inlet and the outlet. Again the mathematical stability requirements should drive in the selection of the appropriate boundary condition. For example, when modeling the mitral valve as an inflow condition on the LV, using a pressure boundary condition on the Navier–Stokes equations (3.20) may lead to numerical instability if flow reversal is allowed and vortical flow develops at the inlet/outlet [104]. Similar instabilities may develop if the defective boundary conditions described in [102] are used to impose the inflow rate.

If an inflow boundary condition is not sufficient to capture the complex flow pattern inside the ventricles, e.g. in the case of pathological valves, it may be necessary to model the shape and dynamics of the valve leaflets explicitly. The level of detail for this model greatly influences the flow pattern inside the heart [107]. The valve leaflets are typically modeled either as immersed resistive surfaces [108,95,109,6] or by fully coupled fluid–valve interaction [110–114]. A dynamical 3-D simulation of the mechanics of the valve leaflets (including contact, coaptation, and chordae tendineae plus papillary muscles for the mitral/tricuspid valves) interacting with the fluid is still very challenging even for industrial-strength commercial solvers.

3.9. Ventricular afterload and coupling with the systemic circulation

Since the function of the heart is greatly influenced by the mechanical load under which it has to operate (according to the Frank–Starling law, see Section 3.4), it is necessary to complete the previously described mechano-fluidic models by prescribing physiological preload and afterload conditions to the heart. In the simplest case this can be achieved with lumped parameter models or “0-D models” that account for the characteristic arterial impedance and consist of coupled sub-systems of resistive, inductive and capacitive elements in accordance to the analogy between fluid networks and electrical circuits, see [103]. The standard approximation for the afterload produced by the systemic circulation is the three-element windkessel model [115]

$$\frac{dQ}{dt} = \frac{1}{R_a R_p C_a} \left[R_p C_a \frac{d}{dt} (P_{in} - P_{out}) + (P_{in} - P_{out}) - (R_p + R_a) Q \right], \quad (3.35)$$

where the two resistive components and the capacitive element correspond to different parts of the systemic circulation: R_a is the peripheral resistance mainly due to small arteries and arterioles, C_a the elastic compliance mainly due to the aorta and other large arteries, and R_a the characteristic resistance of the aorta. Eq. (3.35) is coupled to the heart model through the variables (P_{in} , Q) corresponding to the aortic pressure and flow rate respectively, whereas the venous pressure P_{out} is usually taken as constant parameter. This simple model is nevertheless able to produce reasonably accurate aortic pressure profiles for the simulation of an isolated heart, and can be improved by adding an impedance element in parallel with the aortic resistive element [116].

While lumped parameter models provide good predictions on aortic pressure and flow rates, they cannot represent the pressure wave propagation along the arterial tree nor the back-reflection of waves at bifurcations and junctions. For that, a description of the topology of the arterial tree as well as the major individual arteries is required; this includes measuring the length, radius, wall thickness, tapering, etc. of each artery and prescribing a coupled model to each arterial segment. In typical models the arteries are assumed to be straight 1-D segments and the flow velocity and pressure profiles are assumed to be radially symmetric. This leads, after averaging over each cross-section and applying a thin-wall assumption, to systems of 1-D hyperbolic equations to be used to model the pulse-wave propagation in large and medium-sized arteries [117]. Such models can readily be coupled to heart models for more accurate predictions of arterial hemodynamics than those offered by lumped parameter models. There has been much interest in recent years in constructing extremely detailed models of the human arterial tree (see [118–121] and the references therein) including aspects such as physiological vessel tapering, viscoelasticity, baroreflex autoregulation, and many others.

The issue of personalizing such detailed models of the arterial tree to be patient-specific is still open, but typical approaches include some type of global rescaling of vessel length/diameter and/or distal resistances to account for size and age of the person. It should be remarked that even the 1-D assumption of axisymmetric flow may fail in (i) large, strongly curved arteries such as the aorta; in (ii) non-tubular arteries, for example near a saccular aneurysm; or (iii) arteries that undergo external motion, especially the coronary arteries that experience the full motion of the heart. While advancements in constructing fully 3-D flow simulations in the arterial tree have recently been

made [122], nevertheless considerable difficulties arise in the personalization and calibration of such highly detailed models of patient-specific vasculature (see for instance the works on collagen fiber remodeling in cardiovascular tissues [123,124]). The three models (3-D, 1-D and lumped 0-D), however, can very effectively interplay to form the so-called geometrical multiscale models (see [96,125,103]).

4. Overview on mathematical analysis of sub-models

The mathematical analysis of macroscopic electrical cardiac models has been mainly restricted to the study of solvability and regularity of the monodomain and bidomain equations (generalization of the monodomain model, based on a multicontinuum approach, see e.g. [51,126]) and related formulations concerning the electrophysiology of cardiac tissue. Depending on the complexity of (3.1) and on the nonlinearities and discontinuities of the reaction and/or source terms, it can be quite difficult to derive global existence of solutions using energy methods. Results are available for 3-D cable equations coupled to FitzHugh–Nagumo, Mitchell–Schaeffer, Rogers–McCulloch, Aliev–Panfilov, Hodgkin–Huxley, and Luo–Rudy I ionic models (see [127–129,126,130–132] and the references therein), whereas the analysis of more recent ionic models is still beyond reach with current analytical tools. We also recall that apart from fixed point theorems, other techniques have been explored including e.g. variational principles [133].

On the other hand, existence theorems of general nonlinear elasticity [134,135] are typically based on classical arguments of polyconvexity of the strain energy and the implicit function theorems from [136], whereas applications of that theory to the particular case of hyperelastic materials and passive cardiac mechanics and their discretizations can be found in [137,66,138,139,76,140]. Apart from these isolated contributions, rigorous studies about solvability and stability of solutions for cardiac electromechanics are still not well established. Up to our knowledge, the only available existence results devoted specifically to cardiac electromechanics are to those by Pathmanathan et al. [141,142], who analyzed a general model where the activation depends on the local stretch rate, and the one by Andreianov et al. [143], where an active strain electromechanical model with linearized elasticity and truncated updated conductivity tensors is studied. In the latter, existence of weak solutions was derived by means of the Faedo–Galerkin method and compactness arguments, and uniqueness in a weak–strong comparison setting. Somewhat similar contributions, but more oriented to the study of traveling wave solutions for reaction–diffusion systems coupled with elasticity, can be found in [144,145].

An introduction to techniques used in existence proofs for fluid–structure interaction problems is provided in [146]. The Faedo–Galerkin method was originally applied to the FSI problem in [147], where a fixed-point theorem proving the existence of solutions in the finite-dimensional spaces was combined with a compactness argument to reach the continuous limit. A considerable technical difficulty arises since available compactness results require some conditions on the a priori unknown shape of the fluid domain. In [148] the existence of weak solutions for a three-dimensional viscous incompressible fluid interacting with a flexible elastic plate was proven in the case that an additional viscoelastic term was added to the structure. While the viscoelastic term is rarely added to the model in practice, it is physically motivated as real biological tissue is perfused with blood and other fluids and thus experiences strong viscoelastic effects. Instabilities due to insufficient viscous damping may also manifest themselves in numerical solution algorithms in the form of divergence of classical fixed-point algorithms [149]. Continuous and discrete fully mixed formulations of steady FSI problems have been recently analyzed in terms of extensions to the Babuška–Brezzi theory [150,151], and the existence of solutions to a transient simplified variational fluid–shell–structure model with transpiration boundary conditions was derived in [152]. Essentially all of these FSI-based studies rely on the assumption of infinitesimal strains, which suggest that non-standard theoretical techniques would be required in order to address solvability and regularity issues even for simplified electro-mechano-fluidic coupled problems.

5. Computational strategies for heart integration models

Apart from the intrinsic difficulties associated to the mathematical coupling of different functions of the heart (compatibility of model parameters, merging of different spatio-temporal scales, integrating multimodal information into the same frame of reference, solvability and regularity concerns, etc.), the numerical discretization of such a coupling entails several challenges in its own. Although the integration of multiphysics solvers is usually done employing already existing building blocks, at some point the missing pieces need to be implemented, and sooner or later, close attention needs to be paid to the discretization features of a particular system, including for instance stability of time

integrators, discrete inf–sup conditions for multi-field models, spatial convergence, or scalability performance. Even if all these issues are successfully tackled for each sub-system, it is evident that the mere gluing of these elements together will not necessarily result in a coupled system with the same stability properties as its building blocks.

The aim of this section is twofold: firstly, we present in detail some of the typical discretization schemes applied to each main sub-system of the total heart function, and secondly, to discuss both qualitatively and quantitatively the suitability of popular coupling strategies in the simulation of multiphysics problems, focusing on heart integration.

5.1. Spatial and temporal discretization schemes for electrophysiology

The system of nonlinear reaction–diffusion equations (3.2) features traveling wave solutions. Once a sufficiently large external stimulus current is applied, the ionic currents cause the transmembrane potential to rapidly increase from its resting potential to a depolarized plateau state. This action potential travels as a front across the tissue until the entire heart has been depolarized, followed by a slow repolarization phase where the potential recovers to its resting value (see Fig. 2.4(a)). In homogeneous tissue the solutions of the continuous equation are such that the wavefront travels at constant velocity that does not depend e.g. on the conductivity coefficient \mathbf{D}_0 . However, very different behavior is observed in a spatially discretized system. For instance, a standard second order finite difference method leads to a semi-discrete system whose front propagation velocity depends explicitly on the discretization parameter h . For large enough h the semi-discrete system exhibits standing wave solutions, which translate to total propagation failure [153]. Even if convergence of the propagation velocity is obtained as $h \rightarrow 0$, the discrete propagation velocity may be far from the physiological limit value unless h is chosen extremely small.⁶ Since the accuracy of the propagation velocity is tied to the accuracy of the front approximation this issue can be somewhat remedied by mesh adaptivity near the front, but since the front is moving the region of adaptation has to be constantly updated, leading to large overhead and complications in developing dynamic mesh adaptation algorithms [154,155]. A typical remedy when only computations on coarse meshes are available is to increase the conductivity values until correct activation times are achieved. If the interest is in the modeling of physiological monotone activation patterns, but not pathological re-entrant phenomena, then this may represent a valid compromise.

In a standard finite element approximation of (3.2) the computational domain $\Omega_{E,h}^0$ is obtained by a partition T_h of Ω_E^0 consisting in tetrahedral elements, and each component of the solution at every fixed time t (that we here denote by the generic scalar quantity v) is approximated as

$$v_h(\mathbf{x}, t) = \sum_i v_i(t) \psi_i(\mathbf{x}),$$

where the fields ψ_i are continuous and piecewise polynomial nodal basis functions and v_i are the nodal values of the finite element solution that comprise the unknowns of the discrete problem. By testing against the j th test function ψ_j and integrating by parts we get the semi-discrete formulation of the first equation of (3.2): for suitable finite element spaces X_h , Y_h , find $(v_h, \mathbf{w}_h, \mathbf{c}_h) \in X_h \times Y_h \times Y_h$ such that

$$\begin{cases} C_m \int_{\Omega_{E,h}^0} \dot{v}_h \psi_j \, d\mathbf{x} + \int_{\Omega_{E,h}^0} \mathbf{D}_0(\mathbf{x}) \nabla v_h \cdot \nabla \psi_j \, d\mathbf{x} + \chi \int_{\Omega_{E,h}^0} i_{\text{ion}}(v_h, \mathbf{w}_h, \mathbf{c}_h) \psi_j \, d\mathbf{x} = 0, & \forall j = 1, \dots, N \\ \int_{\Omega_{E,h}^0} \dot{\mathbf{w}}_h \psi_j \, d\mathbf{x} - \int_{\Omega_{E,h}^0} m_{\mathbf{w}}(v_h, \mathbf{w}_h, \mathbf{c}_h) \psi_j \, d\mathbf{x} = 0, & \forall j = 1, \dots, N \\ \int_{\Omega_{E,h}^0} \dot{\mathbf{c}}_h \psi_j \, d\mathbf{x} - \int_{\Omega_{E,h}^0} m_{\mathbf{c}}(v_h, \mathbf{w}_h, \mathbf{c}_h) \psi_j \, d\mathbf{x} = 0, & \forall j = 1, \dots, N \end{cases}$$

or, in matrix form,

$$\begin{cases} C_m \mathbb{M} \dot{V}_h + \mathbb{A} V_h + \chi I_h(V_h, W_h, C_h) = 0 \\ \mathbb{M} \dot{W}_h - m_{\mathbf{w}}(V_h, W_h, C_h) = 0 \\ \mathbb{M} \dot{C}_h - m_{\mathbf{c}}(V_h, W_h, C_h) = 0 \end{cases}$$

⁶ In a physiological full-heart simulation the generally accepted spatial accuracy of $h = 0.2$ mm leads to systems of 200 million and above degrees of freedom if uniform refinement is applied everywhere.

where \dot{v}_h , \dot{V}_h stand for $\partial_t v_h$, $\partial_t V_h$, respectively, $[\mathbb{A}]_{j,i} = \int_{\Omega_{E,h}^0} \mathbf{D}_0(\mathbf{x}) \nabla \psi_i \cdot \nabla \psi_j \, d\mathbf{x}$ are the elements of the anisotropic stiffness matrix, and $[\mathbb{M}]_{j,i} = \int_{\Omega_{E,h}^0} \psi_i \psi_j \, d\mathbf{x}$ are the elements of the mass matrix. The ionic currents in the discrete problem are obtained by using integration over all elements $K \in \mathcal{T}$ as:

$$[I_h]_j = \int_{\Omega_{E,h}^0} i_{\text{ion}}(v_h(\mathbf{x}), \mathbf{w}_h(\mathbf{x}), \mathbf{c}_h(\mathbf{x})) \psi_j(\mathbf{x}) \, d\mathbf{x} = \sum_{K \in \mathcal{T}_h} \int_K i_{\text{ion}}(v_h(\mathbf{x}), \mathbf{w}_h(\mathbf{x}), \mathbf{c}_h(\mathbf{x})) \psi_j(\mathbf{x}) \, d\mathbf{x}. \quad (5.1)$$

A quadrature approximation of (5.1) can proceed in three standard ways [156]: State-Variable Interpolation (SVI), Ionic Current Interpolation (ICI), and Lumped Ionic Current Interpolation (L-ICI):

$$[I_h^{\text{SVI}}]_j = \sum_{K \in \mathcal{T}} \sum_{p=1}^Q \omega_p i_{\text{ion}} \left(\sum_{i=1}^N v_i \psi_i(\mathbf{q}_{p,K}), \sum_{i=1}^N w_i \psi_i(\mathbf{q}_{p,K}), \sum_{i=1}^N c_i \psi_i(\mathbf{q}_{p,K}) \right) \psi_j(\mathbf{q}_{p,K}) \quad (\text{SVI})$$

$$[I_h^{\text{ICI}}]_j = \sum_{K \in \mathcal{T}} \sum_{p=1}^Q \omega_p \left(\sum_{i=1}^N i_{\text{ion}}(v_i, \mathbf{w}_i, \mathbf{c}_i) \psi_i(\mathbf{q}_{p,K}) \right) \psi_j(\mathbf{q}_{p,K}) = \sum_{i=1}^N [\mathbb{M}]_{j,i} i_{\text{ion}}(v_i, \mathbf{w}_i, \mathbf{c}_i) \quad (\text{ICI})$$

$$[I_h^{\text{L-ICI}}]_j = \sum_{K \in \mathcal{T}} \sum_{p=1}^Q \omega_p (i_{\text{ion}}(v_j, \mathbf{w}_j, \mathbf{c}_j) \sum_{i=1}^N \psi_i(\mathbf{q}_{p,K})) \psi_j(\mathbf{q}_{p,K}) = \left(\sum_{i=1}^N [\mathbb{M}]_{j,i} \right) i_{\text{ion}}(v_j, \mathbf{w}_j, \mathbf{c}_j) \quad (\text{L-ICI})$$

where $\mathbf{q}_{p,K}$ is the p th quadrature node in the element K , and ω_p its corresponding quadrature weight. The major difference between these approximations is that in SVI the ODE system for (w_i, c_i) given by the membrane model has to be solved at each quadrature point $\mathbf{q}_{p,K}$, whereas in ICI the ODE system is only solved at the nodal points. The L-ICI method is equivalent to first-order operator splitting, where a reaction step is taken first and followed by a diffusion step:

$$\text{Step 1: } \begin{cases} \dot{W}_h - m_w(V_h^n, W_h, C_h) = 0, & W_h^n = C_h^n, \quad t \in (t_n, t_{n+1}) \\ \dot{C}_h - m_c(V_h^n, W_h, C_h) = 0, & C_h^n = W_h^n, \quad W_h^* = W_h^{n+1}, \quad C_h^* = C_h^{n+1}, \end{cases}$$

$$\text{Step 2: } C_m \mathbb{M} \dot{V}_h + \mathbb{A} V_h + \chi I_h(V_h, W_h^*, C_h^*) = 0, \quad V_h(t_n) = C_h^n, \quad t \in (t_n, t_{n+1}).$$

Numerical studies [156–158] have investigated the stability and accuracy properties of first-order finite element approximations of the monodomain equations and the effects of operator splitting, various types of mass lumping, and several approaches for the computation of ionic currents. The outcome is that on coarse meshes, SVI gives conduction velocities that are too fast, whereas those of ICI/L-ICI are too slow. The case of L-ICI especially suffers from large errors on the speed of propagation on very coarse meshes, and is generally considered inaccurate. It should be noted that for higher-order polynomial approximations the situation may not be so clear and the convergence may not be monotone in the front velocity [159].

Maintaining the positivity of solutions of the reaction–diffusion equation (3.2) is important for preserving numerical stability and avoiding excessive over- and undershoots near the sharp AP front. The form of the reaction part of (3.1) and (3.2) is such that positivity is usually preserved for the gating variables and the ionic concentrations for reasonable time-integration schemes. Thus a violation of the principle of positivity of solutions can only come from solving the diffusive term with a method that does not satisfy a Discrete Maximum Principle (DMP). In the case of isotropic diffusion and linear finite elements, the DMP is only satisfied if mass lumping is used, all the angles in the mesh are strictly acute, and a severe time-step restriction is imposed [46]. For unstructured meshes that are often used for whole heart simulations, this is hardly feasible. In the case of anisotropic diffusion things get even worse, as the diffusion tensor may have negative off-diagonal elements depending on the local orientation of the fibers with respect to the principal coordinate axes, and so there is little hope of satisfying the DMP without modifying locally the FEM [160]. Lumping for the mass matrix is, nevertheless, recommended as it helps at least to reduce the violation of the DMP and the resulting undershoots near the potential front.

5.2. Discretization schemes for solid mechanics

The elastic response of soft tissues is highly nonlinear. Their deformations under working (internal) loads are intrinsically large, so that linear elasticity theory and the associated numerical techniques are, in principle, hardly

applicable. Numerical methods commonly used for (3.3) are constructed on the basis of the principle of virtual work, which entails the minimization of a total potential energy. At equilibrium, such energy can be written as the difference between internal and external (body and boundary) contributions in either Lagrangian or Eulerian form. Related possibilities include the three-fields Hu–Washizu formulation (employed for cardiac mechanics in [161]), the Lagrange multipliers and augmented formulations (applied to computational models of the heart in e.g. [162,163]), or approaches based on discrete descriptions of motion (see for instance [164]).

For sake of conciseness of the presentation, we will restrict ourselves to the case of a quasi (or nearly)-incompressible formulation for the strain energy function (3.5). For a given mechanical model, its quasi-incompressible counterpart can be derived from splitting both the strain energy and the deformation gradient into an isochoric and a pure volumetric contributions $\mathbf{F} = \mathbf{F}_{iso}\mathbf{F}_{vol}$, with $\mathbf{F}_{vol} = J^{1/3}\mathbf{I}$ and $\mathcal{W}(\mathbf{F}) = \mathcal{W}_{iso}(\mathbf{F}_{iso}) + \mathcal{W}_{vol}(\mathbf{F}_{vol})$, where \mathcal{W}_{iso} assumes the form of the Holzapfel–Ogden strain energy. The decomposition implies that the isochoric Cauchy–Green tensors are

$$\bar{\mathbf{C}} = J^{-\frac{2}{3}}\mathbf{C} = \mathcal{I}_3^{-\frac{1}{3}}\mathbf{C}, \quad \bar{\mathbf{B}} = J^{-\frac{2}{3}}\mathbf{B} = \mathcal{I}_3^{-\frac{1}{3}}\mathbf{B}$$

where we used the fact that $\mathcal{I}_3 = J^2$. Therefore, the first isochoric invariant is

$$\bar{\mathcal{I}}_1 = \text{tr } \bar{\mathbf{C}} = J^{-\frac{2}{3}}\mathcal{I}_1.$$

As suggested in [70], the main features of the decomposition can still be captured if the isochoric–volumetric decomposition is applied only to the isotropic terms. In such a case, the relevant part of the first Piola stress reads

$$\begin{aligned} \mathbf{P}_{iso} = & 2 \left[1 - \frac{\gamma_n(\gamma_n + 2)}{(\gamma_n + 1)^2} \right] \mathcal{W}_1^E J^{-\frac{2}{3}} \left(\mathbf{F} - \frac{\mathcal{I}_1}{3} \mathbf{F}^{-T} \right) \\ & + 2 \left\{ \left[\gamma_n \frac{\gamma_n + 2}{(\gamma_n + 1)^2} - \gamma_f \frac{\gamma_f + 2}{(\gamma_f + 1)^2} \right] \mathcal{W}_1^E + \frac{1}{(\gamma_f + 1)^2} \mathcal{W}_{4,f}^E \right\} \mathbf{f} \otimes \mathbf{f}_0 \\ & + 2 \left\{ \left[\gamma_n \frac{\gamma_n + 2}{(\gamma_n + 1)^2} - \gamma_s \frac{\gamma_s + 2}{(\gamma_s + 1)^2} \right] \mathcal{W}_1^E + \frac{1}{(\gamma_s + 1)^2} \mathcal{W}_{4,s}^E \right\} \mathbf{s} \otimes \mathbf{s}_0 \\ & + \frac{1}{(\gamma_f + 1)(\gamma_s + 1)} \mathcal{W}_{8,fs}^E (\mathbf{f} \otimes \mathbf{s}_0 + \mathbf{s} \otimes \mathbf{f}_0). \end{aligned}$$

The volumetric part of the energy can be specified in many ways, here we consider the case

$$\mathcal{W}_{vol}(\mathcal{I}_3) = \mathcal{W}_{vol}(J) = \frac{\kappa}{4} \left[(J - 1)^2 + \ln^2 J \right], \quad (5.2)$$

which gives the following expression for the volumetric part of the stress

$$\mathbf{P}_{vol} = \frac{\kappa}{2} [J(J - 1) + \ln J] \mathbf{F}^{-T},$$

for a bulk modulus κ .

A variational principle can then be formulated using \mathcal{W} , and, in turn, the Euler–Lagrange equations in weak form read: find $\mathbf{d}_S \in \mathbf{D}$ such that

$$\int_{\Omega_S^0} \mathbf{P}(\mathbf{d}_S) : \nabla \mathbf{v} d\mathbf{X} = \int_{\Gamma_S} \mathbf{t} \cdot \mathbf{v} ds \quad \forall \mathbf{v} \in \mathbf{D} = \mathbf{H}_{\Gamma_D}^1(\Omega_S^0), \quad (5.3)$$

where \mathbf{t} is a given traction term. Notice that this nonlinear problem is written in material coordinates. The same development can be applied using the current deformed state (as done e.g. in [165]). We next proceed to linearize (5.3) around a generic state $\hat{\mathbf{d}}_S$. Applying Gâteaux derivatives to the solution operator defining problem (5.3) gives a problem written in terms of the displacement increments: find $\delta \mathbf{d}_S \in \mathbf{D}$ such that

$$D(\delta \mathbf{d}_S, \mathbf{v}) = F(\mathbf{v}) - R_{\mathbf{d}_S}(\hat{\mathbf{d}}_S, \mathbf{v}) \quad \forall \mathbf{v} \in \mathbf{D}, \quad (5.4)$$

where the involved bilinear and linear forms read

$$D(\delta \mathbf{d}_S, \mathbf{v}) = \int_{\Omega_S^0} \left[\frac{\partial \mathbf{P}}{\partial \mathbf{F}}(\hat{\mathbf{d}}_S) : \nabla_0 \delta \mathbf{d}_S \right] : \nabla \mathbf{v} d\mathbf{X}, \quad F(\mathbf{v}) = \int_{\Gamma_S} \mathbf{t} \cdot \mathbf{v} ds, \quad R_{\mathbf{d}_S}(\hat{\mathbf{d}}_S, \mathbf{v}) = \int_{\Omega_S^0} \mathbf{P}(\hat{\mathbf{d}}_S) : \nabla \mathbf{v} d\mathbf{X}.$$

Recalling that the particular form assumed by the first Piola stress tensor depends on \mathcal{W}_{iso} (which in turn depends on a number of invariants) and \mathcal{W}_{vol} :

$$\mathbf{P} = \sum_i \mathbf{P}_i = \sum_i \frac{\partial \mathcal{W}_i}{\partial \mathbf{F}}, \quad i \in \{1, (4, f), (4, s), (8, fs), vol\}, \quad (5.5)$$

implies that the stress, for instance due to the isotropic contributions in \mathcal{W}_{iso} , can be written as

$$\mathbf{P}_{iso} = \frac{\partial \mathcal{W}_1}{\partial \tilde{\mathcal{I}}_1^E} \frac{\partial \tilde{\mathcal{I}}_1^E}{\partial \mathbf{F}} = \frac{\partial \mathcal{W}_1}{\partial \tilde{\mathcal{I}}_1^E} \left(\mathfrak{J}_{11} \frac{\partial \bar{\mathcal{I}}_1}{\partial \mathbf{F}} + \mathfrak{J}_{12} \frac{\partial \mathcal{I}_{4,f}}{\partial \mathbf{F}} + \mathfrak{J}_{13} \frac{\partial \mathcal{I}_{4,s}}{\partial \mathbf{F}} \right),$$

where $\tilde{\mathcal{I}}_1^E = \mathfrak{J}_{11} \bar{\mathcal{I}}_1 + \mathfrak{J}_{12} \mathcal{I}_{4,f} + \mathfrak{J}_{13} \mathcal{I}_{4,s}$ and

$$\mathfrak{J} = \begin{vmatrix} 1 - \frac{\gamma_n(\gamma_n+2)}{(\gamma_n+1)^2} & \gamma_n \frac{\gamma_n+2}{(\gamma_n+1)^2} - \gamma_f \frac{\gamma_f+2}{(\gamma_f+1)^2} & \gamma_n \frac{\gamma_n+2}{(\gamma_n+1)^2} - \gamma_s \frac{\gamma_s+2}{(\gamma_s+1)^2} & 0 \\ 0 & \frac{1}{(\gamma_f+1)^2} & 0 & 0 \\ 0 & 0 & \frac{1}{(\gamma_s+1)^2} & 0 \\ 0 & 0 & 0 & \frac{1}{(\gamma_f+1)(\gamma_s+1)} \end{vmatrix}.$$

Hence we obtain

$$\begin{aligned} \frac{\partial \mathbf{P}_1}{\partial \mathbf{F}} : \nabla_0 \delta \mathbf{u} &= \frac{\partial^2 \mathcal{W}_1}{\partial (\tilde{\mathcal{I}}_1^E)^2} \left[\left(\mathfrak{J}_{11} \frac{\partial \bar{\mathcal{I}}_1}{\partial \mathbf{F}} + \mathfrak{J}_{12} \frac{\partial \mathcal{I}_{4,f}}{\partial \mathbf{F}} + \mathfrak{J}_{13} \frac{\partial \mathcal{I}_{4,s}}{\partial \mathbf{F}} \right) : \nabla_0 \delta \mathbf{u} \right] \\ &\quad \times \left(\mathfrak{J}_{11} \frac{\partial \bar{\mathcal{I}}_1}{\partial \mathbf{F}} + \mathfrak{J}_{12} \frac{\partial \mathcal{I}_{4,f}}{\partial \mathbf{F}} + \mathfrak{J}_{13} \frac{\partial \mathcal{I}_{4,s}}{\partial \mathbf{F}} \right) \\ &\quad + \frac{\partial \mathcal{W}_1}{\partial \tilde{\mathcal{I}}_1^E} \left[\left(\mathfrak{J}_{11} \frac{\partial^2 \bar{\mathcal{I}}_1}{\partial \mathbf{F} \partial \mathbf{F}} + \mathfrak{J}_{12} \frac{\partial^2 \mathcal{I}_{4,f}}{\partial \mathbf{F} \partial \mathbf{F}} + \mathfrak{J}_{13} \frac{\partial^2 \mathcal{I}_{4,s}}{\partial \mathbf{F} \partial \mathbf{F}} \right) : \nabla_0 \delta \mathbf{d}_S \right], \end{aligned}$$

where $\mathbf{P}_1 = \frac{\partial \mathcal{W}_1}{\partial \mathbf{F}}$. In addition, recalling that for a Holzapfel–Ogden strain energy one has

$$\mathcal{W}_1 = \frac{a}{2b} e^{b(\tilde{\mathcal{I}}_1^E - 3)}, \quad \frac{\partial \mathcal{W}_1}{\partial \tilde{\mathcal{I}}_1^E} = \frac{a}{2} e^{b(\tilde{\mathcal{I}}_1^E - 3)}, \quad \frac{\partial^2 \mathcal{W}_1}{\partial (\tilde{\mathcal{I}}_1^E)^2} = \frac{ab}{2} e^{b(\tilde{\mathcal{I}}_1^E - 3)},$$

$$\frac{\partial \bar{\mathcal{I}}_1}{\partial \mathbf{F}} = 2J^{-\frac{2}{3}} \left(\mathbf{F} - \frac{\mathcal{I}_1}{3} \mathbf{F}^{-T} \right),$$

readily gives

$$\begin{aligned} \frac{\partial^2 \bar{\mathcal{I}}_1}{\partial \mathbf{F} \partial \mathbf{F}} : \nabla \delta \mathbf{d}_S &= 2 \frac{\partial}{\partial \mathbf{F}} \left[J^{-\frac{2}{3}} \left(\mathbf{F} - \frac{\mathcal{I}_1}{3} \mathbf{F}^{-T} \right) \right] : \nabla \delta \mathbf{d}_S \\ &= 2 \left(-\frac{2}{3} J^{-\frac{2}{3}} \mathbf{F}^{-T} : \nabla \delta \mathbf{d}_S \right) \left(\mathbf{F} - \frac{\mathcal{I}_1}{3} \mathbf{F}^{-T} \right) \\ &\quad + 2J^{-\frac{2}{3}} \left(\nabla_0 \mathbf{u} - \frac{2}{3} (\mathbf{F} : \nabla \delta \mathbf{d}_S) \mathbf{F}^{-T} + \frac{\mathcal{I}_1}{3} \mathbf{F}^{-T} (\nabla \delta \mathbf{d}_S)^T \mathbf{F}^{-T} \right). \end{aligned}$$

On the other hand, the term involving the volumetric part of the energy assumes the expression

$$\begin{aligned} \frac{\partial^2 \mathcal{W}_{vol}}{\partial \mathbf{F} \partial \mathbf{F}} : \nabla \delta \mathbf{u} &= \frac{\partial}{\partial \mathbf{F}} \left[J \mathcal{W}'_{vol} \mathbf{F}^{-T} \right] : \nabla_0 \delta \mathbf{d}_S \\ &= J \mathcal{W}'_{vol} \left(\mathbf{F}^{-T} : \nabla \delta \mathbf{d}_S \right) \mathbf{F}^{-T} + J^2 \mathcal{W}''_{vol} \left[\mathbf{F}^{-T} : \nabla \delta \mathbf{d}_S \right] \mathbf{F}^{-T} - J \mathcal{W}'_{vol} \mathbf{F}^{-T} (\nabla \delta \mathbf{d}_S)^T \mathbf{F}^{-T}, \end{aligned}$$

where the expressions \mathcal{W}'_{vol} , \mathcal{W}''_{vol} assume the form

$$\mathcal{W}'_{vol} = 2 \left(J - 1 + \frac{\ln J}{J} \right), \quad \mathcal{W}''_{vol} = \frac{2}{J^2} (1 - \ln J).$$

Notice that $D(\delta \mathbf{d}_S, \mathbf{v})$ can be regarded as a purely *constitutive* contribution. In contrast, the analysis under spatial coordinates adds a term coming from residual *geometrical* contributions.

The solvability of the linearized problem (5.4) hinges on the positivity (uniformly with respect to displacements) of the quadratic functional

$$\mathcal{H}(\delta \mathbf{d}_S) = \int_{\Omega_S^0} \left(\frac{\partial^2 \mathcal{W}_{vol}}{\partial \mathbf{F} \partial \mathbf{F}} : \nabla \delta \mathbf{d}_S \right) : \nabla \delta \mathbf{d}_S d\mathbf{X}.$$

A proof along with more details on the derivation above can be found in [166]. Even if (5.4) is uniquely solvable, it is often the case that initial guesses in the Newton algorithm are far from the actual solution. In these circumstances the Newton iterates require combination with continuation methods (see e.g. [167]). For instance, for pure contraction tests of activated cardiac tissue, a common strategy consists in applying incremental loads determined by the increments of the active strain, in order to ensure that the next incremental step will remain within the so-called region of attraction (cf. [76]).

Discretization of the linearized mechanical system. Consider a finite dimensional subspace $\mathbf{D}_h \subset \mathbf{D}$ where discrete displacements will be sought. A Galerkin finite element approximation of the tangent problem (5.4) is: find $\delta \mathbf{d}_{Sh} \in \mathbf{D}_h$ such that

$$D(\delta \mathbf{d}_{Sh}, \mathbf{v}_h) = F(\mathbf{v}_h) \quad \forall \mathbf{v}_h \in \mathbf{D}_h, \quad (5.6)$$

where notation has been abused by merging the discrete residual into the right hand side F . Once a basis $\{\phi_i\}_{i=1}^N$ for \mathbf{D}_h has been defined, with $N = \dim \mathbf{D}_h$, we can expand the solution as

$$\delta \mathbf{d}_{Sh}(\mathbf{X}) = \sum_{i=1}^N \delta d_{Sh}^i \phi_i(\mathbf{X}),$$

where the coefficients δd_{Sh}^i form a vector $\delta \mathbf{D}_S$ of unknowns which is determined from the linear algebraic system

$$\mathbb{D} \delta \mathbf{D}_S = \mathbf{F}, \quad (5.7)$$

with

$$F_i = F(\phi_i) - R_{dS}(\hat{d}_S, \phi_i), \quad D_{ij} = D(\phi_j, \phi_i), \quad 1 \leq i, j \leq N.$$

Now, let \mathcal{T}_h denote a partition of Ω_S^0 into regular tetrahedra K of maximum size h . Notice that some simulation packages targeted for biomechanics employ hexahedral grids and isoparametric elements (one of these examples is Chaste [168]). However we restrict ourselves to Lagrangian finite elements defined on tetrahedral meshes, which can be more commonly found in general-purpose simulation environments. A suitable choice for the basis functions will correspond to continuous element-wise polynomials of maximal degree l defined on the mesh \mathcal{T}_h :

$$\mathbf{D}_h = \{\mathbf{v}_h \in \mathbf{C}^0(\Omega_S^0) : \mathbf{v}_h|_K \in \mathbb{P}_l, \forall K \in \mathcal{T}_h\}, \quad l = 1, 2.$$

Fréchet derivatives of the solution operator can be computed explicitly, yielding a precise form of the tangent problem to be solved at each Newton–Raphson iteration. In many practical situations, the derivation of the exact Jacobian can be cumbersome and viable alternatives are to use automatic symbolic differentiation, or numerical differentiation providing inexact Jacobian block matrices requiring smart preconditioners (see the review [169]).

Another idea typically applied in combination with linearization procedures, is the reutilization of Jacobian blocks over a number of Newton steps (strategy a.k.a. Shamanskii's method [170]), or matrix-updating schemes based on Jacobian rank-one block updating. The approach we follow corresponds to a Newton–Krylov method for which the computational cost of the solution of the linear system is reduced (see also [171]). The solution $\delta\mathbf{D}_S$ of (5.7) is replaced by the approximate solution \mathbf{S} such that

$$\|r_k\| = \|\mathbb{D}_k \mathbf{S} - \mathbf{F}_k\| \leq \eta_k \|\mathbf{F}_k\|, \quad (5.8)$$

where the forcing parameter η_k measures how far the approximation \mathbf{S} is from $\delta\mathbf{D}_S$. When the solution of (5.6) is obtained via Krylov iterative methods, the stopping criterion typically corresponds to fixing η_k . The key idea in Newton–Krylov methods is to use a small tolerance for the Krylov iterations only when sufficiently close to the solution of the nonlinear problem. Following [171] a sequence of tolerances $\{\eta_k\}$ is defined by

$$\eta_{k+1} = \min \left[\eta_0, \max \left(\eta_{k+1}^{\text{safe}}, 0.5\epsilon \frac{\|r_k\|^2}{\|r_{k-1}\|^2} \right) \right], \quad k \geq 1,$$

with

$$\eta_{k+1}^{\text{safe}} = \begin{cases} \eta_0 & k = 0 \\ \max \left(\min \left(\frac{\eta_k}{2}, \eta_{k+1}^{\text{Res}} \right), \eta_{\min} \right) & k > 0, \gamma \eta_k^2 \leq 0.1, \\ \min \left[\frac{\eta_k}{2}, \max \left(\eta_{k+1}^{\text{Res}}, \gamma \eta_k^2 \right) \right] & k > 0, \gamma \eta_k^2 > 0.1, \end{cases} \quad \eta_{k+1}^{\text{Res}} = \gamma \frac{\|r_k\|^2}{\|r_{k-1}\|^2},$$

where $\gamma \in (0, 1]$ and η_{\min} are algorithmic parameters.

The phenomenon of numerical volumetric locking has been observed in many studies using incompressible and quasi-incompressible formulations with low order elements, also in the particular application to cardiac biomechanics [137]. Classical remedies include the use of high order elements, non-conforming methods, stabilized mixed formulations [172,173] or reformulations of the governing equations into three-field models [174], also related to Lagrange multiplier-based methods [162], or less invasive ones such as selective reduced integration, which imply that the main structure of the discrete problem remains unchanged. The amount of compressibility considered here is such that the locking phenomena cannot be appreciated when using linear finite elements. Further complications arise in case that large deformations are localized in particular regions. Classical methods will therefore suffer from severe mesh distortion and an intermediate step of remeshing or re-generation of the connectivity map may be needed, especially in case of FSI couplings.

5.3. Spatial and temporal discretization schemes for fluid dynamics

Fully developed turbulent blood flow is rarely observed in healthy humans [175]. Nevertheless, the flow in the aortic root can be in the transitional regime between laminar and turbulent flow, especially during the deceleration phase where flow instabilities occur. However, the deceleration period is not sufficiently long to enable a turbulent flow to develop [176]. Characteristic figures for maximum Reynolds number are: 2000 for pulmonary veins, 5000 for mitral valve and 5300 for the aortic valve. These ranges of Reynolds numbers and the pulsatile nature of the inlet flow clearly indicate that this complex cyclic flow may well be transitional. Modern imaging tools have shown that physiological blood flow has a spiral laminar behavior in the aorta [116], where it is believed that the spiral structure helps to protect the endoluminal surface of the aortic wall from damage by reducing the laterally directed forces [177].

From a numerical approximation standpoint, because of the transitional nature of the flow, Reynolds Averaged Navier–Stokes (RANS) approaches for modeling turbulence (e.g. $\kappa - \varepsilon$, $\kappa - \omega$ models, etc.) are not appropriate, as they are based on the assumption that the turbulence is fully developed and ergodic. When used to handle transition, they require the user to prescribe the transition location in advance. Generally speaking, Large Eddy Simulation (LES) approaches are more appropriate to handle transitional flow regimes. With LES, only the smallest scales (scales smaller than the mesh size) are modeled, while the large scales evolution is recovered by solving a filtered version of Navier–Stokes equations [178–180]. A sub-grid scale model will account for the effect of the unresolved scales on the dynamics of the resolved ones. This coarse–fine–coarse interaction is realized owing to the Variational Multiscale Method (VMS) that we briefly describe below.

VMS [181] additively separates the scales of interest in a predetermined number of groups, usually two, coarse (resolved) and fine (unresolved) scales, yielding two coupled equations that govern the dynamics of the coarse and fine scales. Coarse scales are typically identified with those resolved by the computational mesh, while fine unresolved (i.e., sub-grid) scales are not properly captured by the mesh, but their effect on the coarse scales needs to be accounted for. The problems that govern the unresolved scales are approximated with local problems that are linearized about the coarse scales and solved utilizing the concept of the “fine-scale Green’s function” (see [182]).

The approach that is presented here is the so-called residual-based VMS modeling approach proposed in [183,184]. Rather than emanating from fluid dynamics concepts, it exploits the mathematical structure of the Navier–Stokes equations and a multiscale decomposition of the space of its admissible solutions. When regarded under this perspective, VMS is potentially apt at solving all flow regimes governed by the Navier–Stokes problem.

For the sake of simplicity, we start by sketching the main steps of the residual-based VMS method on the Eulerian, conservative formulation of the Navier–Stokes equations in a non deformable domain Ω_F . Instead of (3.20) we therefore consider

$$\begin{aligned} \rho_F(\partial_t \mathbf{u}_F + \nabla \cdot (\mathbf{u}_F \otimes \mathbf{u}_F)) - \nabla \cdot \boldsymbol{\sigma}_F &= \mathbf{0} \quad \text{in } \Omega_F \times (0, T], \\ \nabla \cdot \mathbf{u}_F &= 0 \quad \text{in } \Omega_F \times (0, T]. \end{aligned} \quad (5.9)$$

After writing (5.9) under variational form we find the weak formulation of Navier–Stokes equations (for ease of notation we assume \mathbf{u}_F to vanish on the whole boundary $\partial\Omega_F$ of Ω_F):

for all $t > 0$ find $\mathbf{u}_F = \mathbf{u}_F(t) \in \mathbf{V} = (H_0^1(\Omega_F))^d$, $p_F = p_F(t) \in Q = L_0^2(\Omega_F) = \{q \in L^2(\Omega_F) : \int_{\Omega_F} q = 0\}$, such that, if $\mathbf{U} = (\mathbf{u}_F, p_F)$,

$$A(\mathbf{U}, \mathbf{W}) = 0 \quad \forall \mathbf{W} = (\mathbf{w}_F, q_F) \in \mathbf{V} \times Q, \quad (5.10)$$

with

$$A(\mathbf{U}, \mathbf{W}) = \rho_F(\partial_t \mathbf{u}_F, \mathbf{w}_F) - \rho_F(\mathbf{u}_F \otimes \mathbf{u}_F, \nabla \mathbf{w}_F) + (\nabla \cdot \mathbf{u}_F, q_F) - (\nabla \cdot \mathbf{w}_F, p_F) + (2\mu_F \boldsymbol{\varepsilon}(\mathbf{u}_F), \boldsymbol{\varepsilon}(\mathbf{w}_F)),$$

where (\cdot, \cdot) denotes the $L^2(\Omega_F)$ —inner product.

By setting $\mathcal{V} = \mathbf{V} \times Q$ and introducing a direct sum decomposition $\mathcal{V} = \mathcal{V}_h \oplus \mathcal{V}'$ into coarse-scale and fine-scale subspaces, respectively, being \mathcal{V}_h a finite dimensional space – typically, the Cartesian product of the finite element spaces \mathbf{V}_h and Q_h for velocity and pressure approximation – problem (5.10) breaks into the set of equations:

$$A(\mathbf{U}_h + \mathbf{U}', \mathbf{W}_h) = 0 \quad \forall \mathbf{W}_h \in \mathcal{V}_h, \quad (5.11)$$

$$A(\mathbf{U}_h + \mathbf{U}', \mathbf{W}') = 0 \quad \forall \mathbf{W}' \in \mathcal{V}', \quad (5.12)$$

where $\mathbf{U}_h = (\mathbf{u}_{Fh}, p_{Fh}) \in \mathcal{V}_h$ and $\mathbf{U}' = (\mathbf{u}'_F, p'_F) \in \mathcal{V}'$ represent the coarse (resolved) scale and the fine (unresolved) scale components of the solution, respectively. Eq. (5.11) yields

$$\begin{aligned} A(\mathbf{U}_h, \mathbf{W}_h) + \rho_F(\partial_t \mathbf{u}'_F, \mathbf{w}_{Fh}) - \rho_F(\mathbf{u}_{Fh} \otimes \mathbf{u}'_F, \nabla \mathbf{w}_{Fh}) - \rho_F(\mathbf{u}'_F \otimes \mathbf{u}_{Fh}, \nabla \mathbf{w}_{Fh}) \\ - \rho_F(\mathbf{u}'_F \otimes \mathbf{u}'_F, \nabla \mathbf{w}_{Fh}) + (\nabla \cdot \mathbf{u}'_F, q_{Fh}) - (\nabla \mathbf{w}_{Fh}, p'_F) + 2\mu(\boldsymbol{\varepsilon}(\mathbf{u}'_F), \boldsymbol{\varepsilon}(\mathbf{w}_{Fh})) = 0. \end{aligned} \quad (5.13)$$

The first term in (5.13) is called the Galerkin contribution. The second one is set to zero as \mathbf{u}'_F is often assumed to be time-independent (see however [185] for a dynamical model for the fluctuation velocity). The third and fourth terms represent the turbulent cross-stress while the fifth term is the turbulent Reynolds stress. The last term is also set to zero, because of the orthogonality of \mathbf{u}'_F to the coarse-scale velocity in the H^1 -seminorm. See [183] for a detailed derivation and for a comparative analysis with stabilized approximations (such as SUPG and GLS) of Navier–Stokes equations.

As of the fine-scale equation (5.12), it becomes

$$\begin{aligned} A(\mathbf{U}_h, \mathbf{W}') + \rho_F(\partial_t \mathbf{u}'_F, \mathbf{w}'_F) - \rho_F(\mathbf{u}_{Fh} \otimes \mathbf{u}'_F, \nabla \mathbf{w}'_F) - \rho_F(\mathbf{u}'_F \otimes \mathbf{u}_{Fh}, \nabla \mathbf{w}'_F) \\ - \rho_F(\mathbf{u}'_F \otimes \mathbf{u}'_F, \nabla \mathbf{w}'_F) + (\nabla \cdot \mathbf{u}'_F, q'_F) - (\nabla \mathbf{w}'_F, p'_F) + 2\mu(\boldsymbol{\varepsilon}(\mathbf{u}'_F), \boldsymbol{\varepsilon}(\mathbf{w}'_F)) = 0. \end{aligned}$$

After some algebraic manipulation we obtain

$$\begin{aligned} (\mathcal{L}_{\mathbf{u}_{Fh}} \mathbf{u}'_F + \rho_F(\mathbf{u}'_F \cdot \nabla(\mathbf{u}_{Fh} + \mathbf{u}'_F)) + \mathbf{r}_{\text{mom}}, \mathbf{w}'_F) \\ + \rho_f(\nabla \cdot \mathbf{u}_{Fh}(\mathbf{u}_{Fh} + \mathbf{u}'_F), \mathbf{w}'_F) + (\nabla \cdot \mathbf{u}'_F + r_{\text{cont}}, q'_F) - (\nabla \cdot \mathbf{w}'_F, p'_F) = 0, \end{aligned} \quad (5.14)$$

where we have set

$$\mathcal{L}_{\mathbf{u}_{\text{F}h}} \mathbf{u}'_{\text{F}} = \rho_F \partial_t \mathbf{u}'_{\text{F}} + \rho_F (\mathbf{u}_{\text{F}h} \cdot \nabla \mathbf{u}'_{\text{F}} + \nabla \cdot \mathbf{u}_{\text{F}h} \mathbf{u}'_{\text{F}}) - \nabla \cdot [2\mu \boldsymbol{\varepsilon}(\mathbf{u}'_{\text{F}})],$$

(and still we can assume that $\partial_t \mathbf{u}'_{\text{F}} = \mathbf{0}$),

$$\mathbf{r}_{\text{mom}}(\mathbf{u}_{\text{F}h}, p_{\text{F}h}) = \rho_F (\partial_t \mathbf{u}_{\text{F}h} + \mathbf{u}_{\text{F}h} \cdot \nabla \mathbf{u}_{\text{F}h}) + \nabla p_{\text{F}h} - \mu \Delta \mathbf{u}_{\text{F}h},$$

(residual of the coarse-scale momentum equation in non-divergence form), and

$$r_{\text{cont}}(\mathbf{u}_{\text{F}h}) = \nabla \cdot \mathbf{u}_{\text{F}h},$$

(residual of the coarse-scale continuity equation).

To further simplify (5.14) it is assumed that $\nabla \cdot \mathbf{u}'_{\text{F}} \approx 0$ and $\nabla \cdot \mathbf{w}'_{\text{F}} \approx 0$, yielding

$$(\mathcal{L}_{\mathbf{u}_{\text{F}h}} \mathbf{u}'_{\text{F}} + \rho_F \mathbf{u}'_{\text{F}} \cdot \nabla (\mathbf{u}_{\text{F}h} + \mathbf{u}'_{\text{F}}) + \mathbf{r}_{\text{mom}}, \mathbf{w}'_{\text{F}}) = 0, \quad (5.15)$$

which highlights the fact that the fine scales are evolving according to the residual of the coarse-scale momentum equation.

Note that since $\nabla \cdot \mathbf{u}_{\text{F}} = 0$ and $\nabla \cdot \mathbf{u}'_{\text{F}} \approx 0$, this gives $\nabla \cdot \mathbf{u}_{\text{F}h} \approx 0$, which explains why the term (r_{cont}, q_F) has disappeared when going from (5.14) to (5.15). At this stage, the fine scales are modeled as

$$\mathbf{U}' \approx -\boldsymbol{\tau} \mathbf{R}(\mathbf{U}_h),$$

where $\mathbf{R}(\mathbf{U}_h) = \{\mathbf{r}_{\text{mom}}^T(\mathbf{u}_{\text{F}h}, p_{\text{F}h}), r_{\text{cont}}(\mathbf{u}_{\text{F}h})\}^T$ is a 4×1 vector and $\boldsymbol{\tau} = \{\tau_M \mathbf{I}_{3 \times 3}, \tau_C\}$ is a 4×4 block-diagonal matrix where τ_M, τ_C are two constants that depend on $\mathbf{u}_{\text{F}h}$, the time step, the deformation gradient of the transformation between physical and parametric element coordinates and several other constants depending on the piecewise polynomial degree of the finite element velocity field (see [184]).

To sum-up, the final form of the VMS approximate problem writes:
for all $t \in (0, T]$, find $\mathbf{U}_h = \mathbf{U}_h(t) \in \mathcal{V}_h$ such that $\forall \mathbf{W}_h \in \mathcal{V}_h$,

$$\begin{aligned} A(\mathbf{U}_h, \mathbf{W}_h) + (\rho_F \mathbf{u}_{\text{F}h} \cdot \nabla \mathbf{w}_{\text{F}h} + \nabla q_{\text{F}h}, \tau_M \mathbf{r}_{\text{mom}}) + (\nabla \cdot \mathbf{w}_{\text{F}h}, \tau_C r_{\text{cont}}) \\ + (\rho_F \mathbf{u}_{\text{F}h} \cdot (\nabla \mathbf{w}_{\text{F}h})^T, \tau_M \mathbf{r}_{\text{mom}}) - (\nabla \mathbf{w}_{\text{F}h}, \tau_M \mathbf{r}_{\text{mom}} \otimes \tau_M \mathbf{r}_{\text{mom}}) = 0. \end{aligned} \quad (5.16)$$

The first term in (5.16) is the Galerkin contribution, the next two terms correspond to classical stabilization terms (as in SUPG and GLS, see e.g. [186]), the last two terms are peculiar to the VMS method.

These equations are typically advanced in time by the generalized- α method, see [187,188], or by backward differentiation formulas [189]. The extension of the VMS method to the NS problem in ALE formulation (3.20) is made by following the same setting and similar simplifying assumptions. For sake of space, we will not report it here. The reader is however referred to e.g. [190, Sect. 5.2].

5.4. Insights on stability of coupling algorithms using simplified models

Due to the extraordinary complexity of the coupled cardiac multiphysics problem, many simplified models have been proposed and analyzed in literature in order to derive qualitative insight into the features of the system as well as to aid in the calibration of more complicated models [191]. With this aim, we will briefly present a system of seven PDEs in one spatial dimension that contains all of the essential ingredients presented in Sections 3.1–3.2 and Sections 3.5–3.4. Our goal is to provide some insight on the various coupling and solution strategies that can be applied to the fully coupled cardiac multiphysics problem. Our simplified model deliberately omits to address the fluid dynamical aspects, mainly because the difficulty of representing inherently three-dimensional phenomena in just one spatial dimension, but also because in our 3-D problem the fluid and solid mechanics are treated as one monolithic block.

The variables of our simplified model are: v , the transmembrane potential; r , the recovery variable (which allows the dynamical system to repeatedly return to its resting state); k , the average crossbridge stiffness; σ , the average crossbridge tension; H , the macroscopic active stress; u , the displacement from reference configuration in the fiber

direction and \dot{v} its velocity. The resulting model reads as follows (see [192]):

$$\begin{cases} \partial_t v = \frac{\partial}{\partial x} \left(D(u) \frac{\partial v}{\partial x} \right) - kv(v-a)(v-1) - vr + i_{\text{app}} - i_{\text{SAC}}(v, u), & (x, t) \in I \times (t_0, t_f) \\ \partial_t r = \varepsilon(v, r)(-r - kv(v-a-1)) & (x, t) \in I \times (t_0, t_f) \\ v(x, t_0) = v_0(x), \quad r(x, t_0) = r_0(x) \end{cases} \quad (5.17)$$

(cable equation coupled with the Aliev–Panfilov ionic model, equivalent to (3.2) in 1-D)

$$\begin{cases} \partial_t k = - \left(|c(v)| + \left| \frac{\partial \dot{u}}{\partial x} \right| \right) k + k_0 c(v)^+ & (x, t) \in I \times (t_0, t_f) \\ \partial_t \sigma = - \left(|c(v)| + \left| \frac{\partial \dot{u}}{\partial x} \right| \right) \sigma + \sigma_0 \frac{c(v)^+}{2} + \frac{\sigma_0}{k_0} \frac{\partial \dot{u}}{\partial x} k & (x, t) \in I \times (t_0, t_f) \\ k(x, t_0) = k_0(x), \quad \sigma(x, t_0) = \sigma_0(x) \end{cases} \quad (5.18)$$

(the Bestel–Clément–Sorine [32]-model for crossbridge tension, a microscopic version of (3.4))

$$\begin{cases} \partial_t H = \frac{\nu}{\alpha} \sigma - \frac{1}{2} \frac{\sigma_{\max}}{\alpha} H \left(1 + \frac{\partial u}{\partial x} \right)^2 & (x, t) \in I \times (t_0, t_f) \\ H(x, t_0) = H_0(x) \end{cases} \quad (5.19)$$

(compare this *active stress* model to the active strain model (3.10))

$$\begin{cases} \partial_t u = \dot{u} & (x, t) \in I \times (t_0, t_f) \\ \partial_t \dot{u} = \frac{1}{\rho_0} \frac{\partial}{\partial x} \left(S(H, u) \left(1 + \frac{\partial u}{\partial x} \right) \right) & (x, t) \in I \times (t_0, t_f) \\ u(x, t_0) = u_0(x), \quad \dot{u}(x, t_0) = \dot{u}_0(x), \end{cases} \quad (5.20)$$

completed with the mechano-electric feedback and recovery terms

$$D(u) = \frac{\mu}{\left(1 + \frac{\partial u}{\partial x} \right)^2}, \quad i_{\text{SAC}}(v, u) = G_s \left[\frac{\partial u}{\partial x} \right]^+ (v - E_s), \quad \varepsilon(v, r) = \varepsilon_0 + \mu_1 r / (v + \mu_2), \quad (5.21)$$

the piecewise linear chemical reaction term

$$c(v) = \begin{cases} -k_{rs} & \text{if } v < v_{a1} \\ -k_{rs} + \frac{k_{atp} + k_{rs}}{v_{a2} - v_{a1}} (v - v_{a1}) & \text{if } v_{a1} \leq v < v_{a2} \\ k_{atp} & \text{if } v \geq v_{a2}, \end{cases} \quad (5.22)$$

and the total macroscopic stress term

$$S(H, u) = 2c_1 \left[1 - \frac{1}{\left(1 + \frac{\partial u}{\partial x} \right)^3} + \sigma_{\max} H^2 \right]. \quad (5.23)$$

The coupled multiphysics system (5.17)–(5.23) consists of the two-equation electrophysiology model of Aliev–Panfilov [193] equipped with the mechano-electric coupling terms from [194], the crossbridge force generation mechanism based on the distribution moment model from [32], an active stress model similar to those that were derived on thermodynamical principles in [57,78], and an isotropic Neo-Hookean passive material simplified to one-dimensional strains and stresses. For details and derivation of the sub-systems we refer to those works. Suggested parameters for the model (5.17)–(5.23) are given in Table 5.1.

While extremely simplified, this model captures: (i) the force–velocity relationship (3.11), (ii) the force–length relationship, and (iii) the restitution curve and also demonstrates the effects of mechano-electric feedback, which becomes evident when the system is equipped with periodic boundary conditions. In the periodic case the system exhibits two different types of traveling pulses—solutions where one pulse travels to the left and another pulse to the right until they meet (bidirectional solutions), and solutions where one pulse travels in only one direction

Table 5.1

Parameters of the simplified multiphysics model (5.17)–(5.23).

μ	0.001	k_0	0.6	$\text{g cm}^{-1} \text{ms}^{-2}$
k	8	σ_0	0.7	$\text{g cm}^{-1} \text{ms}^{-2}$
a	0.15	k_{rs}	0.02	ms^{-1}
G_s	0.5	k_{atp}	0.009	ms^{-1}
E_s	1	v_{a1}	0.8	
ε_0	0.002	v_{a2}	0.95	
μ_1	0.2	σ_{\max}	0.5	$\text{g cm}^{-1} \text{ms}^{-2}$
μ_2	0.3	c_1	0.02	$\text{g cm}^{-1} \text{ms}^{-2}$
		ρ_0	1	g cm^{-3}

(monodirectional solutions). If the system is periodically excited and forced to enter a monodirectional solution by artificially eliminating one of the traveling pulses, it will remain in this solution branch no matter how the stimulus period is chosen. However, if a sufficiently large external stretch is applied, the mechano-electric feedback term $i_{SAC}(v, u)$ will lead to a termination of the unidirectional pulse and during the next pacing cycle the solution will return to the natural (bidirectional) solution branch.

For the sake of synthesis and notation simplification, let

$$\dot{\mathbf{X}} = \mathbf{F}(\mathbf{X}), \quad (5.24)$$

denote the system obtained after spatial discretization of the Eqs. (5.17)–(5.23) as described in Sections 5.1–5.2. Of course, the solution operator \mathbf{F} is not to be confused with the tensor gradient of deformation. This nonlinear ODE system can be discretized in time using e.g. the standard θ -method

$$\mathbf{X}_n - \mathbf{X}_{n-1} = \theta \Delta t \mathbf{F}(\mathbf{X}_n) + (1 - \theta) \Delta t \mathbf{F}(\mathbf{X}_{n-1}), \quad n = 1, 2, \dots$$

and solved at each time step with a Newton-like solution procedure: given \mathbf{X}_{n-1} , the solution at time t_{n-1} , and the initial guess $\mathbf{X}_n^0 = \mathbf{X}_{n-1}$, solve \mathbf{X}_n^k for each $k = 1, 2, \dots$, such that

$$\left[I - \theta \Delta t \partial_{\mathbf{X}} \mathbf{F}(\mathbf{X}_n^{k-1}) \right] (\mathbf{X}_n^k - \mathbf{X}_n^{k-1}) = \mathbf{X}_{n-1} - \mathbf{X}_n^{k-1} + \Delta t (\theta \mathbf{F}(\mathbf{X}_n^{k-1}) + (1 - \theta) \mathbf{F}(\mathbf{X}_{n-1})) \quad (5.25)$$

or in short to iterate $\mathbf{X}_n^k = \mathbf{X}_n^{k-1} + \delta \mathbf{X}_n^{k-1}$ computed by solving

$$(\mathbb{I} - \mathbb{J}_n^k) \delta \mathbf{X}_n^{k-1} = -R(\mathbf{X}_n^{k-1}, \mathbf{X}_{n-1}),$$

where $\mathbb{J}_n^k = \theta \Delta t \partial_{\mathbf{X}} \mathbf{F}(\mathbf{X}_n^{k-1})$, until an adequate convergence criterion has been reached, where $\mathbf{X}_n = [v_n, r_n, k_n, \sigma_n, H_n, u_n, \dot{u}_n]$ is the global solution vector at time t_n and $\partial_{\mathbf{X}} \mathbf{F}$ denotes the Jacobian of \mathbf{F} .

5.5. Semi-implicit time-stepping algorithms for coupled problems

In practice, a fully implicit solution of the tangent problem (5.25) (see also (5.28)) is rarely performed for more realistic models. The derivation, computation and assembly of all the terms in the full Jacobian of the membrane model can be extremely time-consuming as the membrane model is a system of ODEs up to dozens of complex nonlinear equations with transcendental functions, etc.⁷

In a semi-implicit solution method some of the Jacobian terms are not recomputed at each Newton iteration and instead take their values (extrapolated) from the previous time step [197]. We assume an additive splitting of the system $\mathbf{F}(\mathbf{X}) = \mathbf{F}_1(\mathbf{X}) + \mathbf{F}_2(\mathbf{X})$ and replace the evaluation of the nonlinear right-hand side with an implicit-explicit splitting

$$\mathbf{F}(\mathbf{X}_n^{k-1}) \approx \mathbf{F}_1(\mathbf{X}_n^{k-1}) + \mathbf{F}_2(\mathbf{X}_{n-1}), \quad (5.26)$$

⁷ It is for this reason that the Rush–Larsen scheme [50] applies exponential integrators only on the (linear) differential equations for the gating variables while using explicit methods to update the other variables. This approach requires that the stiffness of the system is present in the gating variables [195], but can be generalized by applying exponential integrators on the entire diagonal of the membrane model equations [196].

where \mathbf{F}_1 is the part of the system that is treated implicitly (stiff component) and \mathbf{F}_2 is the part of the system that is treated explicitly (nonstiff component). For the purposes of constructing block-aware semi-implicit methods we assume the splitting is such that the Jacobian of the implicit part $\partial_{\mathbf{X}}\mathbf{F}_1$ has strictly fewer nonzero blocks than the full Jacobian $\partial_{\mathbf{X}}\mathbf{F}$.

The semi-implicit method obtained by substituting (5.26) into (5.25) is: given \mathbf{X}_{n-1} the solution at time t_{n-1} and the initial guess $\mathbf{X}_n^0 = \mathbf{X}_{n-1}$, solve \mathbf{X}_n^k for each $k = 1, 2, \dots$, such that

$$\begin{aligned} & \left[I - \theta \Delta t \partial_{\mathbf{X}}\mathbf{F}_1(\mathbf{X}_n^{k-1}) \right] (\mathbf{X}_n^k - \mathbf{X}_n^{k-1}) \\ &= \mathbf{X}_{n-1} - \mathbf{X}_n^{k-1} + \Delta t \left[(1 - \theta)\mathbf{F}(\mathbf{X}_n) + \theta(\mathbf{F}_1(\mathbf{X}_n^{k-1}) + \mathbf{F}_2(\mathbf{X}_{n-1})) \right]. \end{aligned} \quad (5.27)$$

In a fully implicit solution scheme for (5.17)–(5.23), the Jacobian \mathbb{J}_n^k in the tangent problem will have the following structure:

$$\mathbb{J}_n^k = \begin{pmatrix} J_{11} & J_{12} & & & & J_{16} \\ J_{21} & J_{22} & & & & \\ J_{31} & & J_{33} & & & J_{37} \\ J_{41} & & J_{43} & J_{44} & & J_{47} \\ & & J_{54} & J_{55} & J_{56} & \\ & & & J_{66} & J_{67} & \\ & & J_{75} & J_{76} & J_{77} & \end{pmatrix}, \quad (5.28)$$

where we have divided the matrix into sub-blocks according to the different sub-systems. Solving the fully implicit system with time step $\Delta t = 1$ ms leads to a convergent Newton method at each time step throughout the cardiac cycle and a stable implicit time-stepping scheme using both the implicit midpoint ($\theta = 1/2$) and the implicit Euler's ($\theta = 1$) method.

As an example of the stability issues that can appear when semi-implicit time-stepping algorithms are used for some of the coupling terms, we consider a splitting such that

$$\partial_{\mathbf{X}}\mathbf{F}_1 = \begin{pmatrix} J_{11} & J_{12} & & & & J_{16} \\ J_{21} & J_{22} & & & & \\ J_{31} & & J_{33} & & & J_{37} \\ J_{41} & & J_{43} & J_{44} & & \\ & & J_{55} & J_{56} & & \\ & & & J_{66} & J_{67} & \\ & & & J_{76} & J_{77} & \end{pmatrix}, \quad \partial_{\mathbf{X}}\mathbf{F}_2 = \begin{pmatrix} & & & & \\ & & & & \\ & & & & \\ & & & & J_{47} \\ & & & J_{54} & \\ & & & & \\ & & & & J_{75} \end{pmatrix} \quad (5.29)$$

that corresponds to the explicit treatment of the coupling terms J_{47} , J_{54} , J_{75} corresponding to the effect of the strain velocity on the average crossbridge tension, the effect of the crossbridge tension on the macroscopic active stress, and the effect of the macroscopic active stress on the rate-of-strain. This represents only a partial decoupling of the crossbridge model from the solid mechanics, as the coupling blocks J_{16} , J_{37} , J_{56} are still updated at each Newton iteration. The numerical solution behavior of this partially decoupled approximation are presented in Fig. 5.1 for both the implicit midpoint ($\theta = 1/2$) and the implicit Euler's ($\theta = 1$) method. Notice that, since we are considering a decoupling of \mathbf{F} where all terms associated to \mathbf{F}_2 are treated explicitly independently of the implicit scheme used for \mathbf{F}_1 (midpoint, Euler), the overall method is indeed semi-implicit. Numerical instabilities clearly manifest when using the implicit midpoint method. The inherent lack of damping for $\theta = 1/2$ means that oscillations start to appear in the crossbridge stress variable σ when the system enters the depolarization phase. After decreasing Δt to 0.1 ms both methods converge and their solutions are nearly identical to the one computed by solving the fully implicit problem (5.25).

5.6. Block-preconditioners from algebraic splitting methods

The standard strategy for solving the tangent problem (5.25) (or its relaxation version (5.27)) relies on using an iterative method plus an efficient preconditioner \mathbb{P} that exploits the block structure of the system. Two main strategies for constructing block-aware preconditioners can be identified:

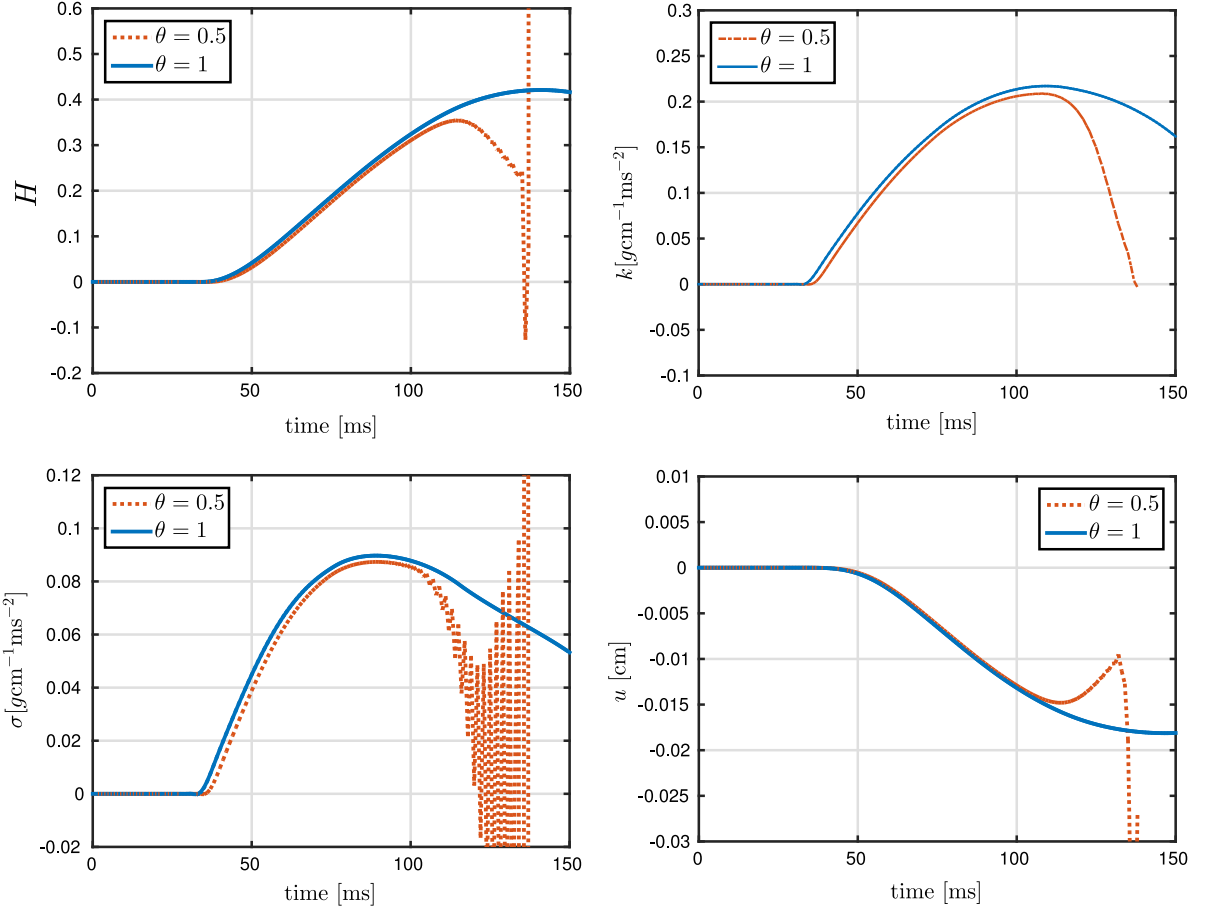


Fig. 5.1. Numerical solution of the system (5.17)–(5.20) using the semi-implicit scheme (5.27) based on the additive splitting (5.29). The implicit Euler's method ($\theta = 1$) retains its stability, whereas the implicit midpoint method ($\theta = 1/2$) suffers from catastrophic instability.

1. (Approximate) block factorizations, e.g. of the form $(\mathbb{I} - \mathbb{J}) \approx \mathbb{L}\mathbb{U}$, where \mathbb{L} and \mathbb{U} are block lower- and upper-triangular respectively, relatively easily invertible so that they may be used as preconditioners in the following way:

$$\begin{cases} 1. \mathbb{L}Y = -R(\mathbf{X}_n^{m-1}, \mathbf{X}_{n-1}) & (\text{by block forward substitution}) \\ 2. \mathbb{U}Z = Y & (\text{by block backward substitution}) \\ 3. \mathbb{U}^{-1}\mathbb{L}^{-1}(\mathbb{I} - \mathbb{J})\mathbf{X}_n^m = Z & (\text{by an iterative method}). \end{cases}$$

Approximate factorization preconditioners have been extensively studied in recent years in the case $N = 2$ (where N stands for the number of blocks in the system) for the Navier–Stokes equations [198,199], and in the case $N = 3$ for fluid–structure interaction equations [200–202] and in general for domain decomposition methods [203,204]. For general multiphysics problems with $N \geq 4$ suitable block factorizations may become rather involved due to filling in of the blocks, requiring either the inversion of many sub-problems or the approximation of many Schur-complement-like blocks.

2. Algebraic splitting methods, where the preconditioner is obtained by a regular splitting of the matrix, $\mathbb{A} = \mathbb{P} + (\mathbb{A} - \mathbb{P})$, where \mathbb{P} is an invertible matrix with block structure inherited from the original problem. In this case the iterative method is

$$\mathbb{P}\mathbf{X}_n^m = (\mathbb{P} - \mathbb{A})\mathbf{X}_n^{m-1} - R(\mathbf{X}_n^{m-1}), \quad (5.30)$$

typically with some sort of relaxation applied to improve the convergence. These methods can be regarded as the block versions of classical iterative methods such as SOR, Gauss–Seidel, Jacobi, etc. [205,47,206].

We focus on the second class of block-preconditioners. Let $\alpha \in \mathbb{Z}_2^{N \times N}$ be a binary matrix that determines the block structure of the preconditioner, and define a corresponding iterative scheme (5.30) with preconditioner $\mathbb{P}(\alpha)$ as

$$\begin{aligned} & \begin{bmatrix} I + \alpha_{11}A_{11} & \alpha_{12}A_{12} & \dots & \alpha_{1N}A_{1N} \\ \alpha_{21}A_{21} & I + \alpha_{22}A_{22} & & \alpha_{2N}A_{2N} \\ \vdots & & \ddots & \vdots \\ \alpha_{N1}A_{N1} & \alpha_{N2}A_{N2} & \dots & I + \alpha_{NN}A_{NN} \end{bmatrix} \begin{bmatrix} X_1^m \\ X_2^m \\ \vdots \\ X_N^m \end{bmatrix} \\ &= \begin{bmatrix} (\alpha_{11} - 1)A_{11} & (\alpha_{12} - 1)A_{12} & \dots & (\alpha_{1N} - 1)A_{1N} \\ (\alpha_{21} - 1)A_{21} & (\alpha_{22} - 1)A_{22} & & (\alpha_{2N} - 1)A_{2N} \\ \vdots & & \ddots & \vdots \\ (\alpha_{N1} - 1)A_{N1} & (\alpha_{N2} - 1)A_{N2} & \dots & (\alpha_{NN} - 1)A_{NN} \end{bmatrix} \begin{bmatrix} X_1^{m-1} \\ X_2^{m-1} \\ \vdots \\ X_N^{m-1} \end{bmatrix} - \begin{bmatrix} R_1 \\ R_2 \\ \vdots \\ R_N \end{bmatrix}. \end{aligned} \quad (5.31)$$

In general, for a problem of N blocks we can have up to $2^{O(N)}$ different choices of such block-preconditioners $\mathbb{P}(\alpha)$. This rather simple choice of the block-preconditioner nevertheless covers a large number of classical iterative methods:

1. For the choice $\alpha = I$, the algorithm corresponds to a block Jacobi iteration or *parallel loosely coupled scheme*, where each sub-system is solved independently and in parallel, solution information is exchanged, and the algorithm is iterated until convergence. This algorithm is the most parallel one, but it only works if the effects of all the coupling blocks are weak compared to the diagonal blocks. To our knowledge there exists no successful block Jacobi implementation of the coupled multiphysics problem of cardiac electromechanics.
2. For the choice $\alpha = \text{LowerDiag}(1)$, the algorithm corresponds to a block Gauss–Seidel iteration or *serial loosely coupled scheme*, where each sub-system is solved sequentially and the solution is used to initialize the next sub-system until all the sub-systems have been solved, and the algorithm is iterated until convergence. This algorithm can work if all the couplings in the upper-diagonal part of the matrix are weak: this includes the stretch-activated currents, the mechanoelectric feedback, the enforcement of a force–length relationship, and the effect of the ventricular pressure on the solid deformation.
3. For the choice $\alpha = 1$, the algorithm corresponds to direct solution of the global Newton tangent problem or *monolithic coupling scheme*. Practical algorithms for monolithic solution schemes often rely on partitioned preconditioners, approximate solves, the omission of some coupling blocks or other techniques that reduce the effective amount of information that needs to be computed and transferred between parallel processes. These approximate preconditioners sometimes (but not always) reduce to the first two cases discussed here. The monolithic approach is the most stable approach for strongly coupled multiphysics problems. The price to pay is that existing solvers for the sub-problems cannot be used directly, but must be adapted to the particular strategy chosen.

The block Gauss–Seidel iteration has the benefit that the application of the preconditioner \mathbb{P} can be performed by back block substitution, which means that only solvers for individual sub-problems (the actions of the inverses A_n^{-1}) are needed. Naturally, applying the block Gauss–Seidel iteration to the standard form of the system is not the only option—for different row–column permutations of the equation system (5.31) we find different block Gauss–Seidel iterations. A possible approach is then to search for α such that the left-hand side of the system (5.31) can be permuted to a block-triangular form among all those α that satisfy the necessary and sufficient contractility criterion for the preconditioned iterative method depending on the spectral radius of the iteration matrix:

$$\rho(I - \mathbb{P}^{-1}(\alpha)\mathbb{A}) < 1,$$

ρ being the spectral radius matrix function. This motivates the following definition (see also [207]):

Definition 5.1. The problem $\mathbb{A}\mathbf{X} = -\mathbf{R}$ contains a *strongly coupled* sub-system if there exists no reducible $N \times N$ matrix⁸ α such that $\rho(I - \mathbb{P}^{-1}(\alpha)\mathbb{A}) < 1$. A system that contains no strongly coupled sub-systems is called *weakly coupled*.

⁸ A matrix X is reducible if there exists a permutation matrix P such that $PXP^T = U$, where U is an upper-triangular matrix. If a matrix is not reducible, it is irreducible.

If the system (5.31) contains no purely algebraic equations (e.g. no quasi-static approximation for the solid mechanics is applied) then for sufficiently small timestep Δt the system is block-diagonally dominant and consequently weakly coupled.

For weakly coupled systems we can therefore find at least one simultaneous row and column permutation of the system \mathbb{A} such that the preconditioner matrix $\mathbb{P}(\alpha)$ of the permuted system can be applied by back block substitution in a serial loosely coupled way. In theory, for linear problems with small N the possible choices of α can be enumerated and the corresponding spectral radii can be checked to first eliminate all the non-convergent algorithms ($\rho \geq 1$), after which the iteration matrix with the least spectral radius provided an optimal choice of the solution method. This becomes unfeasible for $N > 3$ if all the coupling blocks are active, but can still be used for $N = 4$ provided that at most $O(N)$ coupling blocks are nonzero. For coupled systems with $N \geq 5$ and for nonlinear coupled systems where the matrix \mathbb{A} is changing at each Newton iteration such enumeration schemes are not feasible.

In practice, most implementations of coupling algorithms for cardiac electromechanics opt for some compromise between the three aforementioned approaches: strongly coupled sub-systems are grouped together in one block and solved monolithically while the remaining terms are loosely coupled. It is also known that, as far as fluid mechanics inside the ventricle are considered, monolithic schemes are superior in performance to serial tightly coupled schemes due to the large deformations and the large added mass effect (see e.g. [208]).

6. Numerical results

This section is devoted to the presentation of several numerical tests serving as validation of the mathematical models that have been proposed for the different cardiac sub-systems, as well as verification of the associated numerical methods. We start with the issue of reconstructing fibers and sheets of collagen of the myocardium.

For idealized LV shapes one can rely on an analytical description of the fiber fields based on Streeter's famous description of fiber orientations, on bi-ventricular domains a reconstruction algorithm has to be suitably devised. This is the purpose of Section 6.1. In Section 6.2 we test the activation time computed by our monodomain model on a benchmark problem set up in a slab of myocardial tissue that is electrically excited in a corner. Because of the anisotropic propagation of the electrical signal, the use of anisotropic conductivity tensors is mandatory. Section 6.3 deals with the issue of how to recover the natural, stress-free configuration, that is typically unknown in actual computations. We recall that the natural configuration of the cardiac tissue represents the starting point which the constitutive law (3.8) applies to and from which the deformation is computed. The algorithm that we propose is tested on a three-dimensional cubic slab under traction. The electromechanics coupled model is first tested on a three-dimensional slab in Section 6.4 and then on an idealized ventricle in Section 6.5, all along the four phases of ventricular contraction, ventricular blood ejection, ventricular relaxation, and ventricular blood filling. In Section 6.6 the bi-ventricular geometry of a real human heart is considered. The electromechanics model is used to simulate both a physiological and a pathological electrical field propagation. The latter refers to the so-called LBBB (left bundle branch block) conduction defect that leads to delays in the electrical activation of the LV and to an asymmetric ventricular contraction (dyssynchrony). Section 6.7 addresses the case of a patient specific fluid dynamics valve insufficiency simulation in the LV. The ventricular deformation is imposed by an external law, while valves are modeled using three different approaches. The scope of this test is to detect potential numerical instabilities due to flow reversal and the fast valve dynamics. Finally, let us stress that we will not include simulations incorporating SAC models. For the level of complexity of the coupled models at hand, qualitative effects expected by SAC terms can readily be emulated with other sub-model compartments. However, if focusing on fine tuning of electromechanical feedbacks, these terms cannot be discarded (see e.g. [89]).

6.1. Rule-based fiber and sheet reconstruction

As discussed in Section 2.1, the configuration of the fiber and sheet fields in the ventricles plays an important role in the mechanical response during both relaxation and contraction. While on idealized representation of the LV an analytical description of the fiber field can be given [64,21], on biventricular patient-specific domains one needs to employ a reconstruction algorithm. To this aim, several algorithms have been proposed [209–212], and the one we employ herein, originally proposed in [57], is presented below. Myocardial fiber orientations can in principle be recovered *in vivo* from diffusion magnetic resonance imaging by identifying the dominant direction of diffusion as

that of the mean fiber direction. However, cardiac motion artifacts mean that the recovered fiber fields are very noisy and therefore the subject-specific imaging-based fiber fields typically need to be smoothed and/or augmented by some synthetic rule-based description.

In order to define the local frame of reference, representing the direction of anisotropy, the core idea is to compute numerically the transmural distance. Such distance has two important purposes: (1) its gradient is directly associated with the direction of the collagen sheets; (2) it allows to define the transmural angle of rotation of the fiber field.

The first step is to define a pseudo-distance ϕ by solving a simple Laplace problem with the proper boundary conditions:

$$\begin{aligned}\Delta\phi &= 0 \quad \text{in } \Omega_S, \\ \phi &= g \quad \text{on } \Gamma_D, \\ \frac{\partial\phi}{\partial\mathbf{n}} &= h \quad \text{on } \Gamma_N.\end{aligned}\tag{6.1}$$

On a left ventricular model, usually one sets $h = 0$ on Γ_N , the ventricular base, while we set $g = 0$ and $g = 1$ on the endocardial and epicardial surfaces respectively. On a biventricular, patient-specific domain, the specification of the boundary conditions may not be so simple. The idea is to maintain the same boundary conditions for the LV, while adjusting the one for the RV accordingly. In practice, we can still set $g = 0$ on the left endocardial surface and $g = 1$ on the epicardial surface, but we need to define two separate regions on the right endocardial surface such that $g = 1$ on the right septum and $g = 0$ elsewhere. It is easier to understand such configuration, by looking at Fig. 6.1, where we show the solution of problem (6.1) for a biventricular domain and the reconstructed fiber field.

Once the pseudo-distance $\phi(\mathbf{X})$ is known, a local frame of reference can be built in each element, or node, of the mesh. We make the assumption that the sheet field direction can be approximated by using the following relation

$$\mathbf{s}_0 = \frac{\nabla\phi}{\|\nabla\phi\|},$$

that is the sheets are aligned with the transmural direction. This approximation is effective as our activation model assumes that wall thickening takes place in the “radial” direction.

For each element, we can find the plane orthogonal to the sheet direction and we can form a local orthogonal frame of reference by picking two orthogonal vectors in this plane. Our choice is to define an initial “flat” fiber field $\tilde{\mathbf{f}}_0$, such that it is everywhere orthogonal to the centerline of the LV. With this goal, let us define \mathbf{k} , the vector parallel to the left ventricular centerline pointing apex-to-base. Then its projection \mathbf{k}_p on the plane orthogonal to \mathbf{s}_0 is given by

$$\mathbf{k}_p = \mathbf{k} - (\mathbf{k} \cdot \mathbf{s}_0) \mathbf{s}_0$$

and the initial “flat” fiber field is found by

$$\tilde{\mathbf{f}}_0 = \mathbf{s}_0 \times (\mathbf{k}_p / \|\mathbf{k}_p\|).$$

Finally, we can define the fiber direction \mathbf{f}_0 by rotating $\tilde{\mathbf{f}}_0$ with respect to the \mathbf{s}_0 axis

$$\mathbf{f}_0 = \mathbf{R}_{\mathbf{s}_0}(\theta) \tilde{\mathbf{f}}_0.\tag{6.2}$$

We have introduced the rotation matrix $\mathbf{R}_{\mathbf{s}_0}(\theta)$ assuming a one-to-one correspondence between the rotation angle θ and the pseudo-distance ϕ

$$\theta = (\theta_{epi} - \theta_{endo})\phi + \theta_{endo},\tag{6.3}$$

where θ_{endo} and θ_{epi} are the endocardial and epicardial angles of rotation in the sense of [17]. The rotation matrix is computed using Rodrigues’ rotation formula

$$\mathbf{R}_{\mathbf{s}_0}(\theta) = \mathbf{I} + \sin(\theta) [\mathbf{s}_0]_{\times} + 2 \sin^2(\theta/2) [\mathbf{s}_0 \otimes \mathbf{s}_0 - \mathbf{I}],$$

where $[\mathbf{s}_0]_{\times}$ is the cross-product matrix defined as

$$[\mathbf{s}_0]_{\times} = \begin{pmatrix} 0 & -s_{0,z} & s_{0,y} \\ s_{0,z} & 0 & -s_{0,x} \\ -s_{0,y} & s_{0,x} & 0 \end{pmatrix}.$$

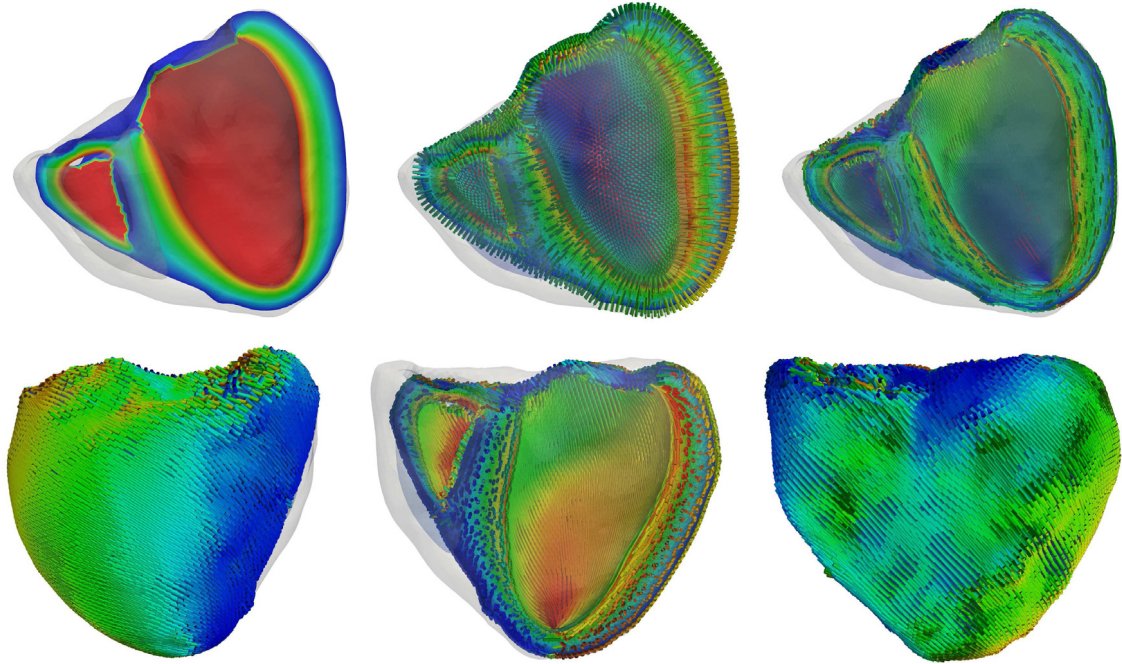


Fig. 6.1. Sheet and fiber field reconstruction on a biventricular geometry. First row, from left to right: Solution of problem (6.1), sheet field, projection of the LV centerline. Second row: views of the fiber field with -45° / $+75^\circ$ fiber angles—colors represent the variation of the z -component. (For interpretation of the references to colour in this figure legend, the reader is referred to the web version of this article.)

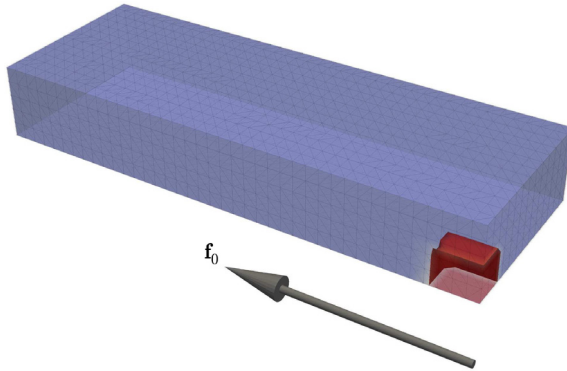


Fig. 6.2. Initial condition for the electrophysiological benchmark on the coarsest mesh with $h_1 = 0.5$ mm. The computational domain is a cuboid of $20 \times 7 \times 3$ mm where fibers are aligned with the long axis.

The above procedure creates a rule-based fiber field that can be used on any geometry. An example of the computed sheet and fiber fields is shown in Fig. 6.1 for a biventricular domain.

6.2. Electrophysiology—numerical effects of front propagation velocity

A benchmark test for the approximation of the transversely isotropic monodomain model was proposed in [157]. This benchmark, performed on rigid domains, highlights the strong dependence of the accuracy of the conduction velocity on the spatial discretization. The initial settings of the benchmark problem consider a slab of myocardial tissue electrically excited in a corner, as shown in Fig. 6.2. Following the benchmark specifications, the fibers here do not exhibit a rotation anisotropy in the thickness, but they are aligned with the long axis. The arrival times at which the tissue is electrically activated (i.e., the time at which the action potential reaches a value that is the average between the plateaux and the rest ones) is registered in the whole domain and the conduction velocity can therefore

be measured. In the benchmark, the slab of myocardial tissue has size $20 \text{ mm} \times 7 \text{ mm} \times 3 \text{ mm}$ and it is electrically stimulated in a region with dimensions $1.5 \text{ mm} \times 1.5 \text{ mm} \times 1.5 \text{ mm}$. In [157], eleven different implementations were tested to evaluate the activation times measured using different codes and spatial discretizations. For such simulations, the authors used the monodomain model coupled with the Ten Tusscher ionic model [49]. Three mesh sizes were used: $h_1 = 0.5 \text{ mm}$, $h_2 = 0.2 \text{ mm}$ and $h_3 = 0.1 \text{ mm}$. While the conduction velocity was found to converge in all implementations as the mesh size h was decreased, for $h = h_1$, nine out of eleven codes underestimated the conduction velocity by about 30%. In order to understand the differences obtained by the different codes, one has to look at the numerical methods used in each simulation. Although in the benchmark paper [157] the specific schemes of each code were not described in detail, thanks to the comparison performed in [213], it is possible to recognize the underlying numerical methods in the finite element codes. In fact, as discussed in this section, the convergence properties of the spatio-temporal approximations presented in Section 5.1, where different numerical integration schemes for the ionic currents are used, can help to identify the adopted method. These methods are: state variable interpolation (SVI); ionic current interpolation (ICI); lumped ionic current interpolation (L-ICI) and operator splitting. Since first order operator splitting and L-ICI methods can be shown to be equivalent, we will describe results only for the L-ICI method. In [213,156], the use of the ICI method was presented as a trade-off between computational cost and accuracy. In fact, at already $h = h_1$, this method seems to be able to reproduce conduction velocities better than L-ICI and SVI. On the other hand, at coarser mesh sizes the method suffers the same shortcomings as the L-ICI method, the presence of conduction failure. As our experience indicates, the choice of the method depends on the solution strategy used for considering the appropriate spatial resolution. For example, as the following convergence test demonstrates, on coarse meshes the SVI and ICI methods cannot give good approximations of the conduction velocities, not even when using effective conductivity coefficients. Moreover, to prove that the same results hold for other ionic models, we shall substitute the ionic model with the simplified minimal model for human tissue [53].

In Fig. 6.4 we show the activation times using the different schemes presented in Section 5.1. As in the original work [157], L-ICI underestimates conduction velocities for coarse meshes, while SVI and ICI overestimate them. In Fig. 6.3 we show the evolution of the wavefronts in the different cases. In the L-ICI case, for $h = h_1$, the anisotropy is greatly increased as the wavefront describes a slow plane wave in the cross-fiber direction. Mesh refinement cures this numerical artifact. On the other hand, in the ICI and SVI cases we experienced the opposite behavior, so that the anisotropy is largely reduced.

The anisotropic propagation of the electrical signal requires the use of anisotropic conductivity tensors. As reported in several studies [214], the ratio in the conductivity coefficients is about 4:2:1 in the fiber:sheet:normal directions, respectively. Ventricular activation is initiated effectively from a series of point sources (Purkinje-muscle junctions in the sub-endocardium [59]) and will locally resemble an ellipsoidal front with axes equal to the directions of anisotropy until it reaches the other point source wavefronts to form the main propagation front (moving apex-to-base and endo-to-epi in direction of the fibers). Therefore, in physiological conditions the activation pattern can travel in all possible directions, not simply the mean fiber direction, and will experience varying velocities of propagation between the upper and lower bounds given by the longitudinal and transversal conduction velocities. Even more importantly, the correct spatial resolution must be used when studying pathological cases, such as myocardial infarction and subsequent scarring. The conduction velocity in some regions may be a fraction of the physiological one [215], necessitating further mesh refinement. Moreover, the adequate representation of conduction velocities will influence dispersion of repolarization, spatio-temporal alternans onset and bifurcation (see e.g. [216,10]). Again, note that the benchmark test does not consider rotational anisotropy, which according to [217], is key in obtaining reasonable accuracy in all directions of propagation (see also [218]).

According to [219,12], a spatial resolution of approximately 0.25–0.3 mm is appropriate for linear finite element approximations of human ventricular electrophysiology under a monodomain description. Although, such an estimate seems to be in accordance with the results shown in the benchmark test, a simple convergence test shows that it is an optimistic estimate. In order to represent physiological conduction velocities with an error smaller than 5% in the sheet and cross-fiber directions, the mesh size should be decreased by at least one order of magnitude. In fact, in the benchmark problem, the domain has the largest size in the fibers direction and, therefore, we are mainly focusing on the convergence of the conduction velocity restricted to this direction.

At $h = h_3$, the approximation of the signal propagation in the direction orthogonal to the fibers is still inaccurate. In Fig. 6.5 we show the spatial convergence of the conduction velocity for L-ICI, ICI and SVI. The SVI and ICI methods converge to the true conduction velocity from above while L-ICI converges from below. Moreover, we show

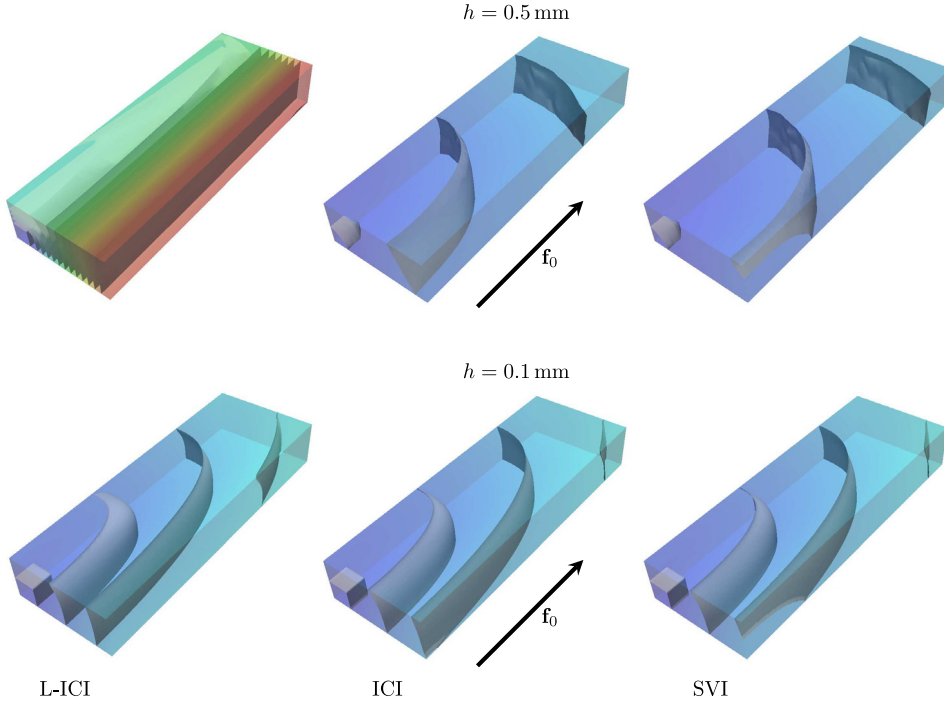


Fig. 6.3. Activation times using Lumped ICI, ICI and SVI for mesh sizes $h_1 = 0.5$ mm and $h_3 = 0.1$ mm. The parameters used are: membrane capacitance $C_m = 1 \mu\text{F cm}^{-2}$; surface area to volume ratio $\chi = 1400 \text{ cm}^{-1}$; longitudinal conductivity $\sigma_f = 1.3342 \text{ k}\Omega^{-1} \text{ cm}^{-1}$; transversal conductivity $\sigma_s = 0.17606 \text{ k}\Omega^{-1} \text{ cm}^{-1}$.

in Fig. 6.5 that while the conduction velocity in the fibers direction is well approximated at $h = h_3$, in the transversal direction it is not, since the conductivity coefficient is smaller. We stopped the refinement process when the relative difference of conduction velocities between two mesh sizes was under 5%. In the transverse direction this is achieved at $h = 0.01$ mm, while in the fibers direction this condition was met at $h = 0.05$ mm.

Such spatial resolution, for a human ventricular geometry of about 150 cm^3 , is usually too expensive to be used. If a uniform mesh is used, a simple calculation leads to the following estimates: for a mesh size $h = 0.25$ mm, the ventricle is discretized using about 100 K elements; for $h = 0.1$ mm, about 1 M elements are needed; for $h = 0.05$ mm, about 10 M elements are needed; for $h = 0.01$ mm, about 1 billion elements are required.

In order to reduce the computational cost needed for such resolutions, the following strategies can be used: (1) anisotropic meshes, (2) adaptive mesh refinements, (3) higher-order spatial discretizations, or (4) modifying the effective conductivity coefficients to correct the conduction velocities to mesh size effects. While anisotropic meshes are difficult to obtain for a complex organ as the heart, adaptive mesh refinement has been successfully used by some authors [155,220–222]. Although not really as robust as mesh adaptivity, the modification of effective conductivity coefficients according to mesh size is usually the preferred choice (however it is often not explicitly mentioned in the literature).

From the point of view of temporal discretization, the largest usable timestep is usually dictated by stability conditions, as typical for a stiff system of equations. As noted in [223], the relative difference in conduction velocity using $\Delta t = 0.02$ ms and $\Delta t = 0.0001$ ms is smaller than 5%.

The results of this convergence test give us several indications about the method to choose. The SVI method is not suitable on coarse meshes, as it would greatly overestimate the conduction velocity. Moreover, due to the increased computational cost, the method has limited practical use, even for sufficiently fine meshes. On the other hand, artificially increasing the conductivity coefficient in the L-ICI method could easily solve the problem of slow conduction velocities for coarse meshes. The ICI method instead is a combination of the SVI and L-ICI methods: although it generally overestimates the conduction velocities, for sufficiently large mesh sizes the conduction velocity goes to zero. Practically, the ICI method adds some numerical diffusion to the L-ICI method. Since this contribution is due to a consistent mass matrix on the right hand side of the equation, it cannot capture the underlying anisotropy.

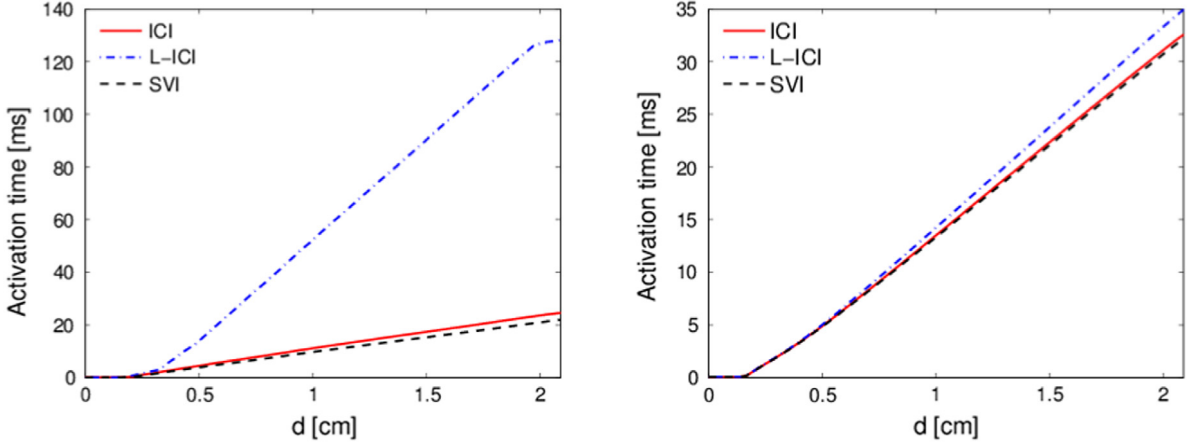


Fig. 6.4. Activation times along the diagonal of the slab using the different methods at fixed mesh size of $h_2 = 0.5 \text{ mm}$ (left) and $h_3 = 0.1 \text{ mm}$ (right plot).

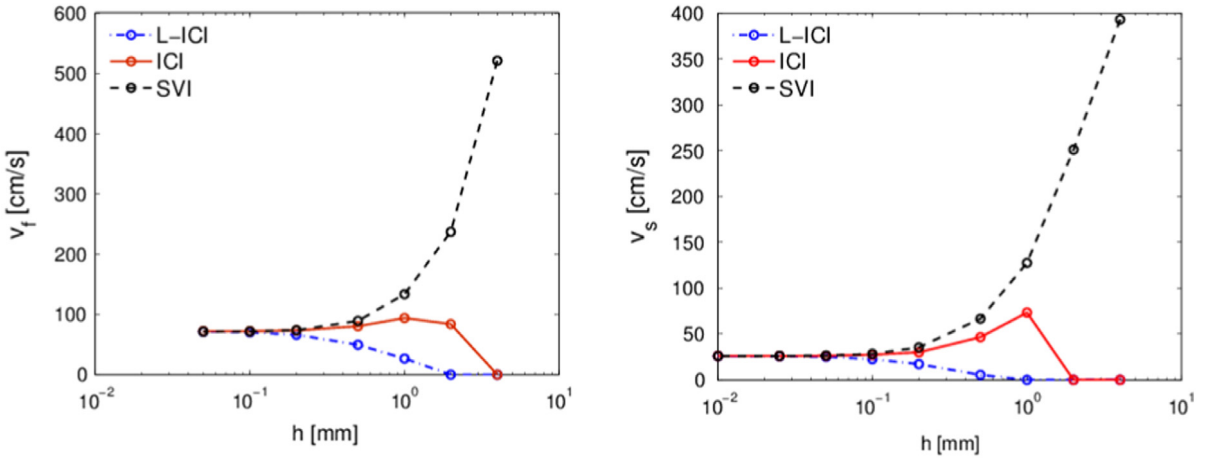


Fig. 6.5. Comparison of the convergence test in a pseudo-1D domain with different ionic current interpolations. Mesh refinement was stopped when the difference between the predicted conduction velocities differ less than 5%.

In conclusion, only for the L-ICI method (or operator splitting methods) we can conveniently modify the conductivity coefficients, capturing in this way a more accurate approximation of the conductivity velocities. We define the effective conductivity tensor, replacing definition (3.18) with $\mathbf{D}^* = \sigma_s^* \mathbf{I} + (\sigma_f^* - \sigma_s^*) \mathbf{f}_0 \otimes \mathbf{f}_0$, where σ_f^* and σ_s^* are modified conductivity coefficients, such that the conduction velocities in the longitudinal and transversal directions are captured also on coarse meshes. We show in Fig. 6.6 the values of the effective conductivity coefficients for different meshes corresponding to the physical coefficients $\sigma_f^0 = 1.3342 \text{ mS/cm}$ and $\sigma_s^0 = 0.17606 \text{ mS/cm}$.

Additional comparisons and analyses of the methods used above can be found in [213,156]. Although one can expect these methods to behave similarly when periodic electrical stimuli are applied, the interaction between waves, or the evolution of spiral waves, is affected by the dispersion error introduced in the system. For instance, in finite element computations, lumped mass matrices are well known to increase the dispersion error in comparison with consistent ones. The interested reader is referred to [156] for some examples in the specific context of cardiac electrophysiology.

6.3. Cardiac mechanics—recovery of the natural configuration

The constitutive law (3.8) describes the stress-strain relationship from the natural configuration to the deformed one. In actual applications, on the other hand, the stress free configuration is usually unknown and the computational

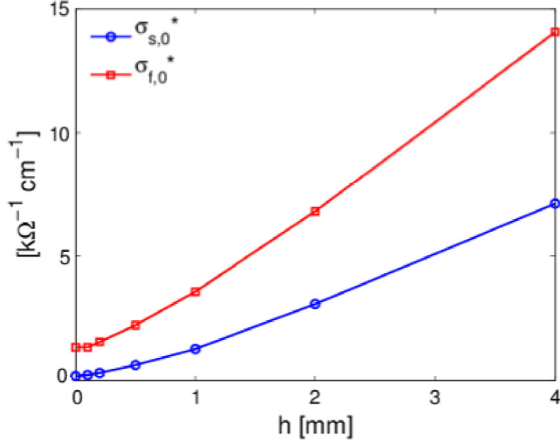


Fig. 6.6. Effective conductivity coefficients in order to keep conduction velocity constant in the L-ICI method.

domains derived from MRI data or other imaging techniques cannot predict experimentally observed and in-vivo deformations. It is therefore important to determine the natural configuration of the tissue in order to use the definition (3.8) and to numerically compute physiological deformations. This procedure can be carried out with several techniques such as the so-called inverse design (ID) analysis [224,225] or the modified updated Lagrangian formulation (MULF) [226]. A discussion on the two approaches can be found in [227]. Other methods include determining strains from 3D MRI or ultrasound, as in [228,229], respectively. It is clear that, to find out the natural configuration, the stresses acting on the material must be known. Generally, in cardiac mechanics, prestresses are not usually known, and under normal physiological conditions one can try to guess the preload pressure which may range between 4 and 20 mm Hg [19].

Here, we develop an iterative scheme alternative to ID and MULF. Although the simple method shown here has been developed independently, we have found that the same approach was already used in [230], without any considerations, however, on the convergence of the algorithm.

Consider the deformed domain Ω_S . Then the deformation map ϕ_S from the natural reference configuration and the prestressed configuration is given by

$$\mathbf{x}' = \phi_S(\mathbf{x}^0) = \mathbf{x}^0 + \mathbf{d}_S(\mathbf{x}^0), \quad (6.4)$$

where the displacement field $\mathbf{d}_S(\mathbf{x}^0)$ is the solution of the elastostatic problem

$$\begin{cases} -\nabla \cdot \boldsymbol{\sigma}_S = \mathbf{0}, & \text{in } \Omega_S, \\ \boldsymbol{\sigma}_S \mathbf{n}_S = \boldsymbol{\ell}, & \text{on } \Gamma_N, \\ \mathbf{d}_S = \mathbf{0}, & \text{on } \Gamma_D, \\ \boldsymbol{\sigma}_S \mathbf{n}_S + \alpha \mathbf{d}_S = \mathbf{0}, & \text{on } \Gamma_R, \end{cases} \quad (6.5)$$

with $\partial\Omega_S = \Gamma_D \cup \Gamma_N \cup \Gamma_R$, and Γ_D , Γ_N and Γ_R mutually disjoint. We have assumed the presence of possible homogeneous Robin boundary conditions and homogeneous Dirichlet boundary conditions. The boundary load $\boldsymbol{\ell}$ represents the preload acting on the material.

We identify the stress free domain Ω_R and the prestressed domain Ω_S with the coordinates of their material points \mathbf{x}^0 and \mathbf{x} , respectively. To evaluate \mathbf{x}^0 it is possible to directly use (6.4), such that

$$\mathbf{x}^0 = \mathbf{g}(\mathbf{x}^0) = \mathbf{x}' - \mathbf{d}_S(\mathbf{x}^0). \quad (6.6)$$

In (6.6), we stress the fact that \mathbf{x}^0 is a fixed point of the map \mathbf{g} . Assuming the existence of at least one displacement field \mathbf{d}_S solution of (6.5), the fixed point iteration scheme $\mathbf{x}_{k+1}^0 = \mathbf{g}(\mathbf{x}_k^0)$ is convergent if

$$\|\nabla \mathbf{g}(\mathbf{x}^0)\|_\infty < 1. \quad (6.7)$$

Since the known deformed configuration is a data of the problem, it is straightforward to show that condition (6.7) holds if

$$\|\nabla(\mathbf{x}^t - \mathbf{d}_S)\|_\infty = \|\nabla\mathbf{d}_S\|_\infty < 1. \quad (6.8)$$

The convergence of the fixed point scheme (6.6) depends on the amount of deformations the material has undergone. Although inequality (6.8) is a restriction on deformations, we note that it covers large deformations. By definition, condition (6.8) holds in the linear elasticity regime (where one assumes $\|\nabla\mathbf{d}_S\|_\infty \ll 1$). Moreover, (6.8) is valid for stretches and shears up to 100%. In physiological conditions, cardiac fiber stretches less than 30% during end diastole and wall thickening is typically smaller than 50% during systole.

Since the nonlinearity of the constitutive material law, solution of (6.5) must be carried out with incremental preload steps. Therefore we propose the following algorithm: given a tolerance ε , a preload ℓ with a ramp sequence $\{\ell_m\}_{m=0}^M$, with $\ell_{m+1} > \ell_m$ and $\ell_M = \ell$, and initial condition $\mathbf{x}^0 = \mathbf{x}^t$, that is $\mathbf{d}_S^0 = \mathbf{0}$ for all m

1. set the initial guess $\mathbf{d}_{S,m}^0 = \mathbf{d}_{S,m-1}$.
2. While $\|\mathbf{x}^t - \mathbf{x}_m^{0,k+1}\| < \varepsilon$
 - (a) find the solution $\mathbf{d}_{S,m}^{k+1}$ from
$$\nabla \cdot \boldsymbol{\sigma}_S(\mathbf{u}_{S,m}^{k+1}) = \mathbf{0}, \quad \text{in } \Omega_{m,k},$$

$$\boldsymbol{\sigma}_S \mathbf{n}_S = \ell_m, \quad \text{on } \Gamma_{N,m},$$

$$\mathbf{u}_m^{k+1} = \mathbf{0}, \quad \text{on } \Gamma_{D,m},$$

$$\boldsymbol{\sigma}_S \mathbf{n}_S + \alpha \mathbf{d}_{S,m}^{k+1} = \mathbf{0}, \quad \text{on } \Gamma_{R,m},$$
with a Newton–Krylov iterative scheme;
 - (b) update the computational domain to find $\Omega_{m,k+1}$ by setting
$$\mathbf{x}_m^{0,k+1} = \mathbf{x}^t - \mathbf{d}_{S,m}^{k+1}.$$

This algorithm generates a sequence of configurations $\{\Omega_m\}_{m=0}^M$, such that when $m = M$, $\Omega_R = \Omega_M$. In other words, when $m = M$, we found the stress-free reference configuration Ω_R on which the application of the given prestress ℓ gives the configuration Ω_S , as a solution of the forward nonlinear elastic problem.

We test the above algorithm on three dimensional traction cases starting from the deformed cubic domain $\Omega_S = (0, 1)^3$, as shown in Fig. 6.7. We consider loads of magnitude 2, 4 and 8 mm Hg applied in the fiber, sheet and cross fiber direction, respectively. In all cases, condition (6.8) was always strictly satisfied, as it can be seen in Fig. 6.7.

6.4. Electromechanics—a simple benchmark test

In this section we apply the electrophysiology benchmark from Section 6.2 to the orthotropic electromechanical model. In order to better identify the deformations in the orthogonal directions, we increase the domain size to consider a slab of $20 \times 16 \times 12$ mm³. The aim of such benchmark is to show the behavior of the activation model in simple settings. For this reason, we keep the same boundary conditions on the electrophysiology as in the original benchmark while imposing zero normal displacements, $\mathbf{d}_S \cdot \mathbf{n}_S = 0$, on the faces where the electrical stimulus is applied, and stress-free boundary conditions elsewhere. The fibers, sheets and cross-fibers directions are aligned with the axis, as shown in Fig. 6.8, where the orthotropy of the activation model is apparent. In fact, the shortening in the fibers direction is smaller than the shortening in the cross-fibers direction. On the other hand, the largest deformation takes place in the sheets direction, where the activation model induces expansion. This behavior of the activation model stands in contrast with other commonly used active stress model in orthotropic media where the largest deformations take place in the fibers direction (see [19] for an example of a similar test).

We have also proposed a more physiological benchmark test in [57], where a simple transmural slab is considered together with rotational anisotropy. We proved there that the activation model considered herein is capable of reproducing the desired wall thickening in a natural way under several loading conditions. A purely mechanical benchmark, under more physiological conditions, has also been recently published in [231] where the performances of different codes and discretization methods were thoroughly tested.

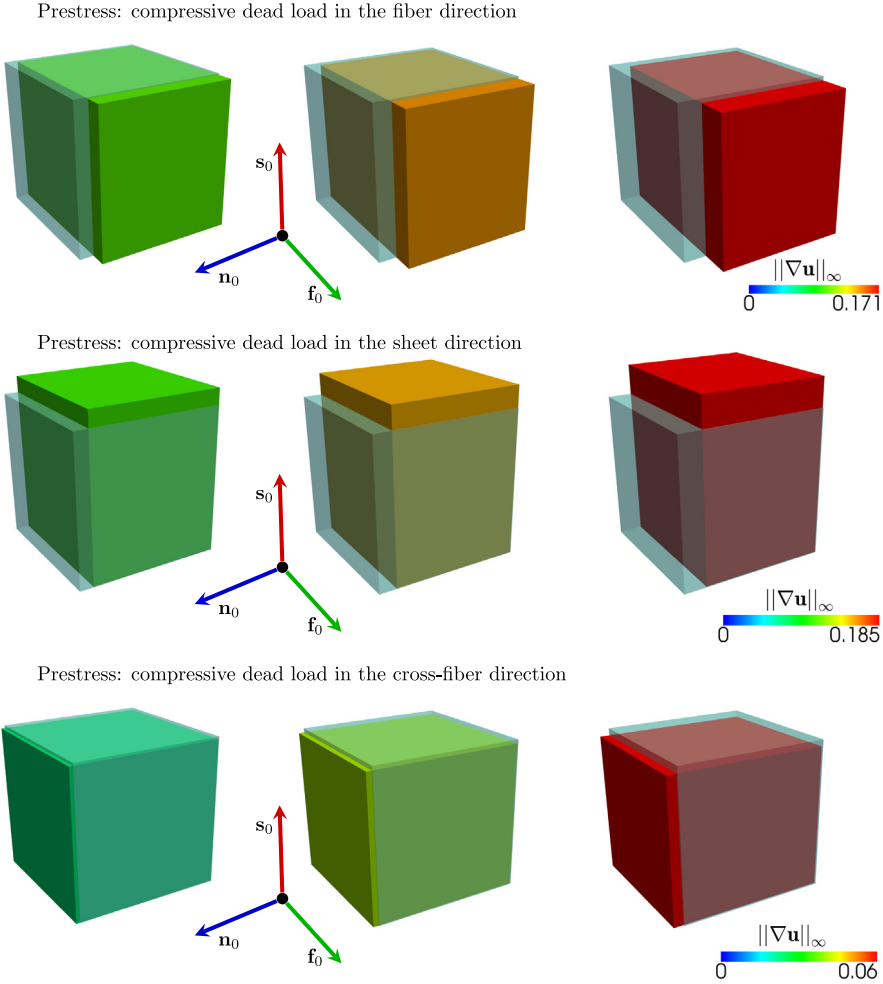


Fig. 6.7. Natural configurations corresponding to compressive dead loads of 2, 4, 6 mm Hg (left to right) in the fiber (top), sheet (center), cross-fiber (bottom) directions. The shadowed cubic domain is the prestressed configuration. Note that during compression the anisotropic contribution is switched off: a compressive load in the fiber direction tests the stiffness of the sheets; a compressive load in the sheet direction tests the stiffness of the fibers; a compressive load in the cross-fiber direction tests the stiffness of both fibers and sheets.

Here, our aim is to evaluate the effects of considering the term $J\mathbf{F}^{-1}\mathbf{D}_m\mathbf{F}^{-T}$ in the diffusion operator on the electrical activation times. If $J\mathbf{F}^{-1}\mathbf{D}_m\mathbf{F}^{-T} = \mathbf{D}_m^0$, that is \mathbf{D}_m is the push forward from the reference to the deformed configuration of \mathbf{D}_m^0 , then this term has no influence on the electromechanical system. On the other hand, if we consider $J\mathbf{F}^{-1}\mathbf{D}_m\mathbf{F}^{-T} = J\mathbf{F}^{-1}\mathbf{D}_m^0\mathbf{F}^{-T}$, then a one way electromechanical coupling may give different results than those from a two way coupling. As discussed in Section 3.5, the behavior of the traveling pulses under deformation is still controversial [91], and therefore, we focus our attention on the possible acceleration of the wave during mechanical deformations, which is clearly driven by the evolution of the mechanical activation. A sharp and sudden contraction would greatly influence conduction velocities. In our model, the tissue reaches maximum mechanical activation after 160–200 ms from electrical excitation. Since the considered slab is fully electrically excited in less than 40 ms, the active deformations are still small and therefore $\mathbf{F} = \mathbf{F}_E\mathbf{F}_A \approx \mathbf{F}_E$. This implies that under normal conditions conduction velocities are almost constant, and mainly depend on passive deformations. We recall that we are neglecting the action of stretch activated currents. Snapshots of the electromechanical benchmark on a 3M elements mesh are shown in Fig. 6.8.

In cardiac electromechanics it is usual to consider one spatial discretization for the electrophysiology and a different one for the mechanics because the mechanical system, which is solved quasi-statically, undergoes less mesh size restrictions than those typically associated with computational electrophysiology. In the left column of Fig. 6.9 we show

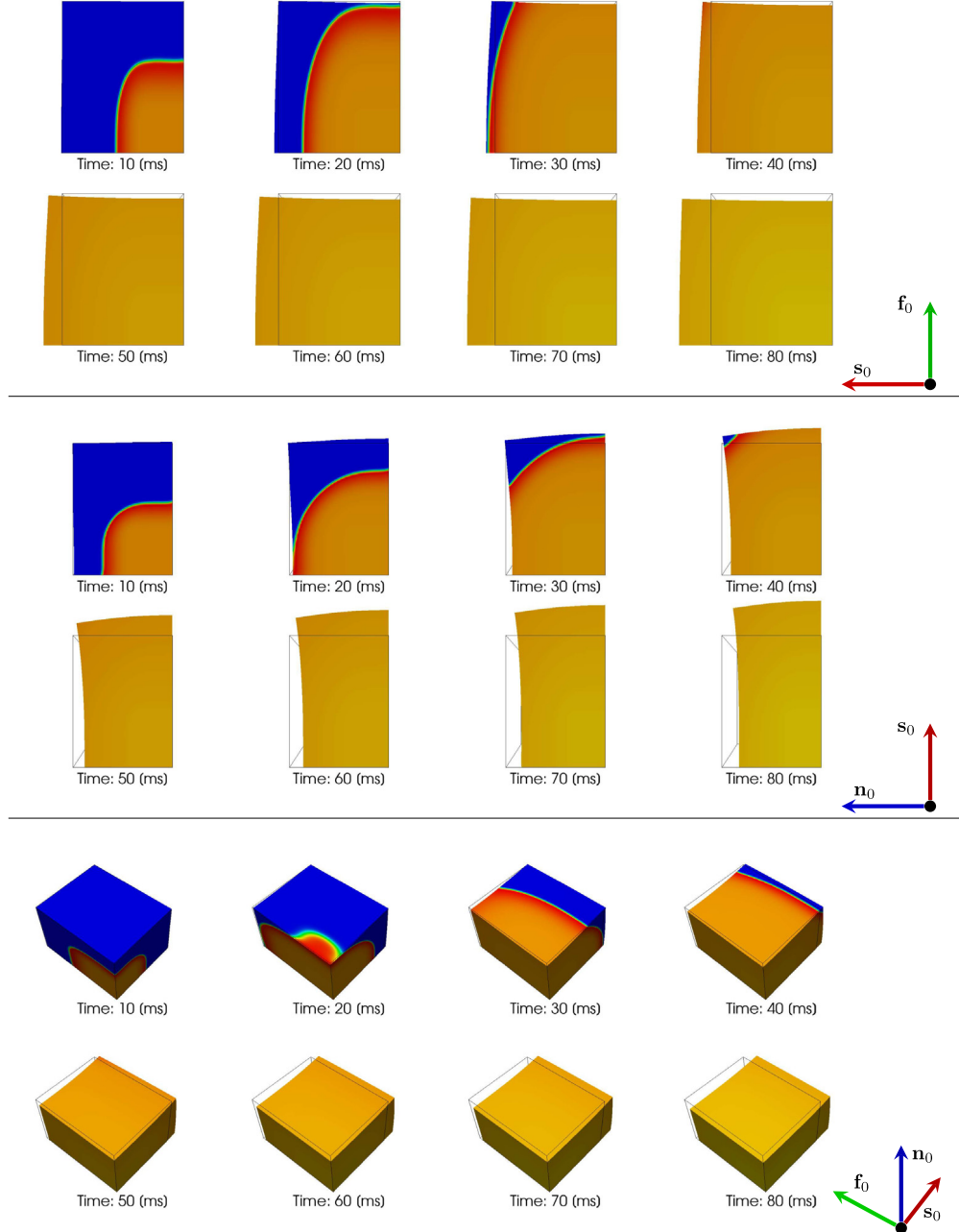


Fig. 6.8. Snapshots of the electromechanical benchmark from different views: transmembrane potential over deformed configurations. (Top two rows) fiber direction view (fibers vertical/sheets horizontal); (Middle rows) sheet direction view (sheets vertical/cross-fiber horizontal). (Bottom rows) isometric view: the fiber direction corresponds to the direction of faster propagation of the transmembrane potential. The largest contraction takes place in the cross-fiber direction, while the block expands in the sheet direction. The mechanical activation model is the main responsible factor for such deformations, as zero normal displacement boundary conditions are applied to the face where the tissue is electrically stimulated and stress-free boundary conditions are applied on the remaining faces.

the evolution of the active strain when the same mesh is used for all fields. On the center and right columns, different meshes have been used for the mechanics and for the electrophysiology problems. Since the evolution equation of the active strain directly depends on the calcium-like variable in the minimal model which is moderately stiff, we solve at each timestep the evolution equation on the electrophysiology mesh to avoid the mesh transfer operations at each time

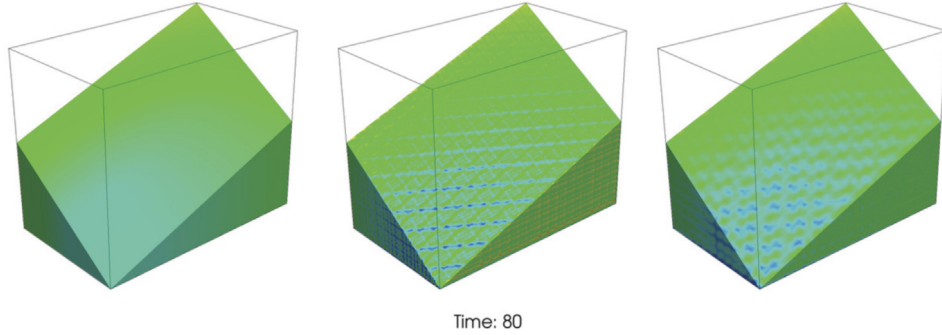


Fig. 6.9. Snapshots of the active strain in the electromechanical benchmark at time 80 ms, using different meshes. Left panel: activation field γ_f using the same mesh for all fields; center: activation field γ_f computed on the electrophysiology mesh with displacement evaluated on a coarser mesh; right plot: activation field γ_f evaluated with radial basis functions on the coarse mechanical mesh.

step. On the other hand we employ a recently developed RBF (radial basis function) interpolation method [232] that allows increased accuracy as well as good parallel performances. Using different meshes, the active strain is computed on the fine electrophysiological mesh and then transferred to the coarse mechanical mesh. Additionally, the displacement field computed in the coarse mesh must be transferred to the fine mesh to be coupled with the monodomain and to the active strain equations. The evolution of the active strain depends on a nonlinear function of the fiber stretch, namely the force–length relationship, which therefore depends on the gradient of the displacement. When the gradient is computed after interpolation, it leads to instabilities, as displayed in Fig. 6.9. In particular, we show in the center and right columns the computed active strain in the fine and coarse meshes, respectively. Notably, even in presence of these instabilities, the overall deformations do not greatly differ when using different meshes from the ones computed on the same mesh. In particular, denoting with \mathbf{d}_s the displacement solution of the electromechanical system using the same mesh and with \mathbf{d}_d the displacement solution obtained with different meshes we found that the norm of the difference of the two solutions satisfies $\|\mathbf{u}_s - \mathbf{u}_d\|_{L^2(\Omega)} < 10^{-5}$ at every timestep.

6.5. Electromechanics—idealized ventricular contraction

During a cardiac cycle four ventricular phases are recognized: (1) Isovolumetric ventricular contraction; (2) Ventricular ejection; (3) Isovolumetric ventricular relaxation; and (4) Ventricular filling.

In the first phase the ventricle starts contracting while both the mitral and aortic valves stay closed, hence the volume of blood contained in the ventricle in this phase is constant. When the ventricular pressure becomes higher than the aortic pressure, the aortic valve opens and the second phase starts. The volume decreases until the pressure decreases below the aortic valve pressure. At this point the aortic valve closes again and the muscle starts to relax. Again, in the third phase, both valves are closed, and muscle relaxation takes place at constant ventricular blood volume. When ventricular pressure decreases below atrial pressure the mitral valve opens and the blood starts filling the ventricle increasing the ventricular pressure. This fourth phase ends when the ventricular pressure becomes once again higher than atrial pressure so that the mitral valve closes and the cycle starts again.

To introduce the above relations in the ventricular simulations we follow the algorithm proposed in [233] and successfully applied in [19]. The endocardial boundary conditions are always set such that

$$\sigma \mathbf{n}_S = -p \mathbf{n}_S, \quad \text{on } \Gamma_{\text{endo}},$$

where p is the ventricular pressure. Note that the pressure is imposed in the actual configuration, introducing in this way a nonlinear boundary condition. We can pull back to the reference configuration the above condition to obtain

$$\mathbf{P} \mathbf{n}_S^0 = -p \mathbf{J} \mathbf{F}^{-T} \mathbf{n}_S^0, \quad \text{on } \Gamma_{0,\text{endo}}, \tag{6.9}$$

where \mathbf{n}_S^0 is the normal on the reference configuration and \mathbf{P} is the first Piola–Kirchhoff stress tensor defined as in (5.5) (recall that we are solving for the nonlinear deformations in the reference state). This condition can be further simplified using the approximation

$$\mathbf{P} \mathbf{n}_S^0 = -p \mathbf{n}_S^0, \quad \text{on } \Gamma_{0,\text{endo}}. \tag{6.10}$$

The error introduced using (6.10) instead of (6.9) is usually smaller than the modeling errors present in the system. For this reason, in the following we restrict ourselves to (6.10). In any case, (6.9) does not pose any particular difficulty and the algorithm discussed below can be coupled with such boundary condition in the same way.

The value of p at each timestep is unknown and the algorithm below will be used in order to find its approximation.

Consider a given value p_p of the preload pressure and fixed value p_a of the aortic pressure. Before applying the electrical stimulus, we preload the ventricle using an incremental step method until the actual pressure p attains the value p_p and the ventricular volume V reaches V_p . Then we apply the electrical stimulus on the full endocardium to initiate ventricular contraction.

During isovolumetric contraction, the ventricular volume remains constant while pressure increases. In practice, we will relax this constraint assuming the condition

$$\frac{|V - V_p|}{V_p} \leq \varepsilon, \quad (6.11)$$

to be a reasonably good approximation of volume conservation. Still, when mechanical contraction starts ventricular volume decreases and we therefore need to relate ventricular pressure with ventricular volume. Again, let the superscript n identify the temporal level. At fixed n , $p_0^n = p^{n-1}$, with $p_0^0 = p_p$, and we consider a fixed point scheme, as proposed in [233,19] from time-varying elastance models. Given the active strain γ_f^n at the current timestep, we solve for every k the quasi-static active nonlinear elastic problem

$$\begin{aligned} \nabla \cdot \mathbf{P}(\mathbf{d}_{S_n}^k, \gamma_f^n) &= \mathbf{0}, \quad \text{in } \Omega_0, \\ \mathbf{P}(\mathbf{d}_{S_n}^k) \mathbf{n}_S^0 &= -p_k^n \mathbf{n}_S^0, \quad \text{on } \Gamma_{0,\text{endo}}, \\ \mathbf{d}_{S_n}^k \cdot \mathbf{n}_S^0 &= 0, \quad \text{on } \Gamma_{0,\text{base}}, \\ \mathbf{P}(\mathbf{d}_{S_n}^k) \mathbf{n}_S^0 + \alpha \mathbf{d}_{S_n}^k &= \mathbf{0}, \quad \text{on } \Gamma_{0,\text{epi}}, \end{aligned}$$

and

$$p_{k+1}^n = p_k^n - \varsigma (V_k^n - V_p), \quad (6.12)$$

where $\varsigma > 0$ is a penalization parameter; until condition (6.11) is satisfied and we set $p^n = p_k^n$, from which V_k^n is computed. The fixed point scheme (6.12) is convergent if

$$\left| 1 - \varsigma \frac{\partial V}{\partial p} \right| < 1,$$

which leads to the conditions $\frac{\partial V}{\partial p} > 0$ and $\varsigma < 2/\frac{\partial V}{\partial p}$. Since $\frac{\partial V}{\partial p}$ is classically defined as the ventricular compliance C_v , which is always positive [234], we find that $\varsigma < 2/C_v$. Moreover the value of ς is also constrained by the Newton's scheme used to solve the nonlinear elasticity problem. In fact, if from (6.12) we obtain a new approximation for the endocardial load much bigger than the one at the previous iteration, we may need an additional incremental step method in order to ensure convergence. From [233], we set the left ventricular compliance to 11 ml kPa^{-1} , from which we find $\varsigma < 0.18 \text{ kPa ml}^{-1}$. This estimate for the penalty parameter is far too large and therefore we replace it with $\varsigma \approx 2/(3C_v) \approx 0.06$.

To evaluate (6.12) we also need to compute the inner volume of the ventricle, which is outside the computational domain. To this end, we note that,

$$V = \int_{\Omega_{\text{endo}}} dV = \int_{\Omega_{\text{endo}}} \nabla \cdot [(\mathbf{x} \cdot \mathbf{e}_1) \mathbf{e}_1] dV = \int_{\Gamma_{\text{endo}}} (\mathbf{x} \cdot \mathbf{e}_1) (\mathbf{e}_1 \cdot \mathbf{n}_S) dA, \quad (6.13)$$

where we assumed Ω_{endo} to be constrained by a flat lid at the base such that $\mathbf{e}_1 \cdot \mathbf{n}_S = 0$, with $\mathbf{e}_1 = (1, 0, 0)$. Pulling back to the reference configuration we obtain

$$V = \int_{\Gamma_{0,\text{endo}}} J \mathbf{X}_1 \cdot \mathbf{F}^{-T} \mathbf{n}_S dA, \quad (6.14)$$

with $\mathbf{X}_1 = (\mathbf{x} \cdot \mathbf{e}_1) \mathbf{e}_1$. Formula (6.14) provides a direct and easy to implement method to evaluate the volume of the LV.

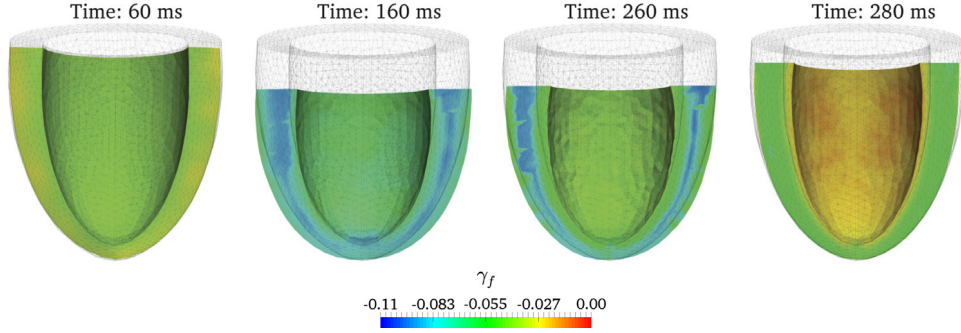


Fig. 6.10. Snapshots of the configurations taken during idealized ventricular contraction with pressure–volume relation on the endocardial surface. From 0 to 60 ms isovolumetric contraction; from 80 to 200 ms ejection phase; from 220 to 260 ms isovolumetric relaxation; from 280 to 300 ms ventricular filling. For visualization we shifted the deformed configuration such that the apex is fixed.

When $p_k^n \geq p_a$, the aortic valve opens and the volume is allowed to decrease. To model ejection we use a simple two element windkessel model [9,19] such that

$$C\dot{p} = -\dot{V} - \frac{p}{R}.$$

A more detailed description of the overall blood circulation can be obtained taking into account more elements as in [83,28,235].

When the muscle starts to relax, ventricular volume starts to increase. Therefore, when $\dot{V} > 0$, we start the isovolumetric relaxation phase. To keep the volume constant we use the same scheme used for the isovolumetric contraction phase (6.12) until the pressure reaches the preload value $p = p_p$. We do not take into account the ventricular filling and we just let the volume recover its preloaded initial value V_p while keeping constant pressure, that is $p = p_p$. When a new electrical stimulus is applied to the ventricle the volume starts to decrease, that is $\dot{V} < 0$, and we start the cycle again considering the isovolumetric contraction phase. Since in this case the ventricular pressure is increased at each timestep, the Robin boundary conditions on the epicardium are not sufficient to remove rigid motion. Since the coefficient α is unknown and its tuning is difficult we preferred in this case to set to zero the normal displacement at the base.

The pressure–volume loops with the above procedure are shown in Fig. 6.11 for three different preload values. The ejection fraction obtained was about 51%, 55% and 58% for 5 mm Hg, 10 mm Hg and 15 mm Hg preload, respectively. Although the model presented here has not been tuned to represent a specific set of data, the values obtained for the end systolic volume and the ejection fraction are in accordance with MRI measurements of normal subjects [236,237]. As expected, in normal conditions when afterload and contractility are held constant, the end systolic volume is relatively insensitive to the change in the preload. On the other hand, the initial increase in pressure is slower than expected, since blood volume during isovolumetric contraction is not perfectly conserved. Overall, the proposed idealized LV model is able to represent major key aspects of the systolic function, such as wall-thickening, apex-to-base shortening, ejection fraction and peak ventricular pressure. An in-depth validation of the model with respect to experimental will be postponed for a forthcoming study. A more detailed investigation on the pressure–volume loops will also help in better assessing the active strain model under both physiological and pathological conditions.

Some snapshots of the configurations assumed by the ventricle during the phases of a cardiac cycle are shown in Fig. 6.10.

6.6. Electromechanics—left bundle branch block

In this test case, we consider electromechanics simulation in a full biventricular model of the human heart. Our objective is to show that the proposed models are applicable also in more realistic setting and are able to reproduce some observed changes under cardiac conduction abnormalities.

A biventricular geometry segmented from CT scan data and a tetrahedral mesh consisting of 250k vertices and 1M elements [238] was modified to handle elasticity boundary value problems. On the final mesh consisting of 750k

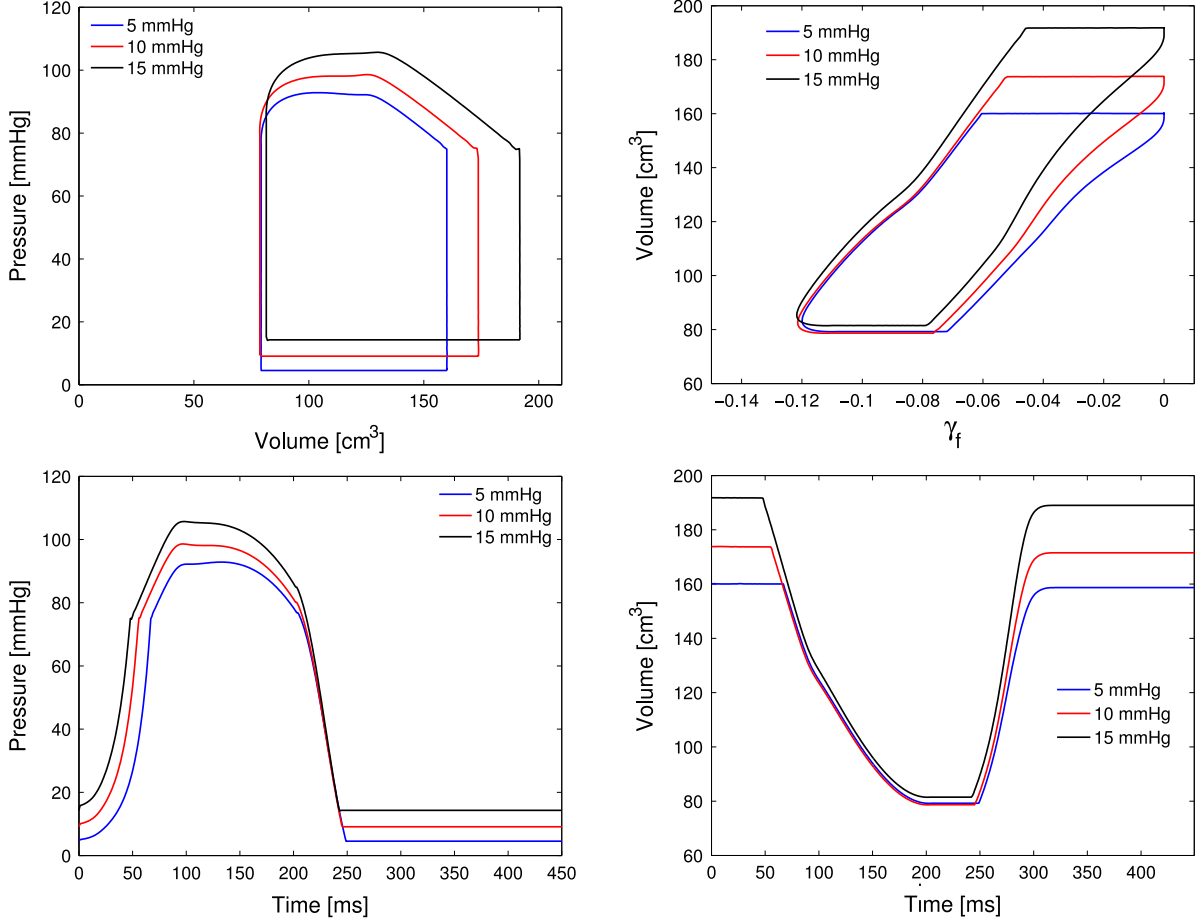


Fig. 6.11. Ventricular cycle on the idealized LV for three preload values: 5 mm Hg, 10 mm Hg and 15 mm Hg, corresponding to about 51%, 55% and 58% of ejection fraction, respectively. Pressure–volume loops (top left), volume–activation loops (top right) and time evolution of the ventricular pressure (bottom left) and volume (bottom right).

elements we employed the algorithm proposed in Section 6.1 to construct rule-based sheet and fiber fields (see other techniques in e.g. [19,239,240]).

We consider both a healthy and a pathological case. In the first case, the initial electrical stimulus has been applied in the apical region of the RV endocardium and in a central region of the LV endocardium. For the pathological case, we consider left bundle branch block (LBBB) which is an irreversible conduction defect that leads to delays in the electrical activation of the left ventricle [241]. LBBB is usually associated with a deterioration of LV function and an overall reduction in global ejection fraction. Several types of LBBB may exist and the mechanical effects may depend upon the site of block. Many computational studies are arising to study LBBB and to optimize cardiac resynchronization therapy (CRT) [242,243]. In simulating LBBB, our interest is exclusively in understanding if the proposed mechanical activation model could also be used to study pathological processes. We refer the interested reader to [241] for more information on LBBB and CRT. For our purposes LBBB will be modeled by stimulating only the RV in the same way as in the healthy case.

The electrical activation times in the two cases are shown in Fig. 6.12. While in the normal case the LV is fully activated in less than 100 ms, under LBBB conditions the signal propagates slowly from the right to the LV and the full electrical activation takes about 230 ms. For the elasticity problem, we set Robin boundary conditions on the epicardium, $\sigma_S \mathbf{n}_S + k \mathbf{d}_S = \mathbf{0}$, with $k = 3.75 \text{ mm Hg cm}^{-1}$, and constant preload pressure conditions on the endocardium, $\sigma_S \mathbf{n}_S = -p \mathbf{n}_S$. In particular we preloaded with 15 mm Hg the LV and 8 mm Hg the RV. This endocardial boundary conditions are not physiological, as discussed in the previous test. On the other hand two main difficulties arise when considering the domain shown in Fig. 6.12: the computation of the right ventricular volume,

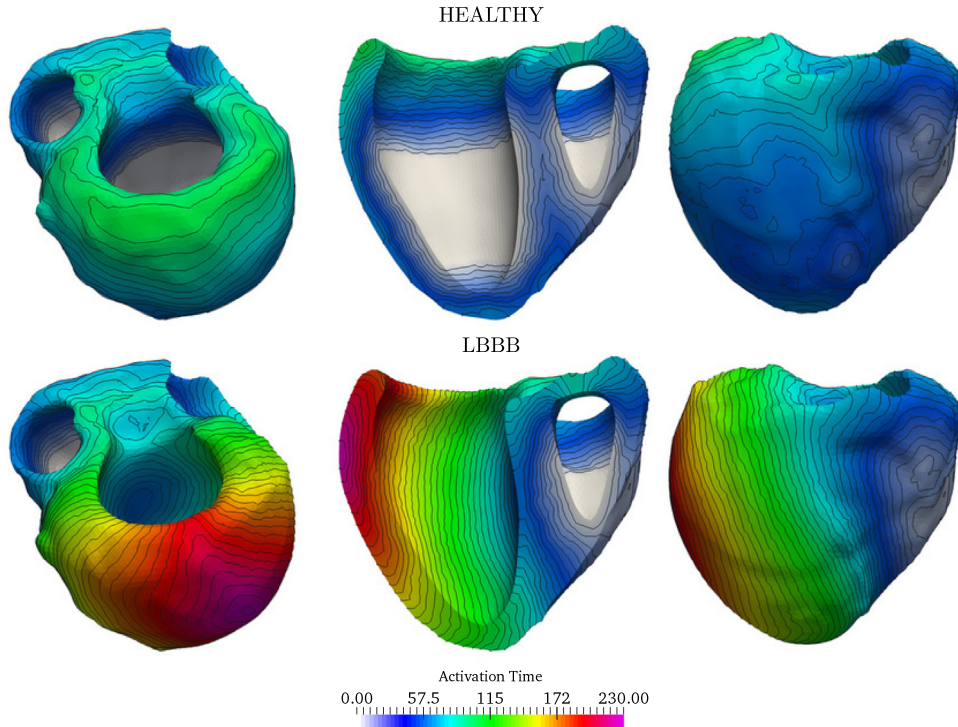


Fig. 6.12. Electrical activation times in the healthy case (top) and under LBBB (bottom). The isolines are plotted at 5 ms of distance.

which has now two disconnected boundary regions which are neither equally oriented nor part of the computational domain, and the distinction of the epicardial and endocardial boundaries. Therefore, for our current purposes, we neglect pressure–volume relationships.

We show in Fig. 6.13 the result of the full electromechanical coupling on the human heart for the healthy case (left) and for LBBB (right). Without change in the parameters, for both healthy and pathological cases, the model was able to recover roughly 40% of wall thickening and 13% of longitudinal shortening in the healthy case and uneven contraction pattern as well as a slightly reduced longitudinal shortening of 11%. On the other hand, the LBBB condition induces changes in the morphology of the tissue: for example, left ventricular hypertrophy and left ventricular dilation can be found in patients with this pathology. Such changes affect the conductivity as well as the stiffness of the tissue [244]. Electrophysiological simulations of the LBBB condition have also shown changes in the associated electrocardiograms when hypertrophy and dilation are considered [245]. Although we use an electrical activation pattern similar to other computational models of LBBB, fine tuning of the parameters as well as precise information about the fiber and sheet fields would be necessary to represent patient-specific situations. Nonetheless, this biventricular test case proves the potential of the model presented here for studies on normal and pathological cardiac functions.

6.7. Fluid dynamics in the LV—modeling of valve insufficiency

In what follows we provide an example of a patient-specific fluid dynamics simulation in the LV for a scenario of chronic mitral valve insufficiency that is modeled using the three different valve models of Section 3.8: Model A, Model B, and Model C. The scope is to show how potential numerical instabilities due to flow reversal and rapid local flow dynamics during valve opening/closure can be numerically avoided, and to show that simple lumped parameter models can correctly describe phenomena such as mitral valve regurgitation. The model used is that of Navier–Stokes equations in a moving domain—the motion of the LV is recovered from 4-D (space and time) images and, for purposes of numerical regularization, imposed on a thin elastic solid surrounding the LV rather than directly on the fluid domain. This is therefore a fluid–structure simulation. However, the structure deformation is known *a priori* (in all of it, as it is a thin structure) and need not be recovered from solving (3.21) in the present setting.

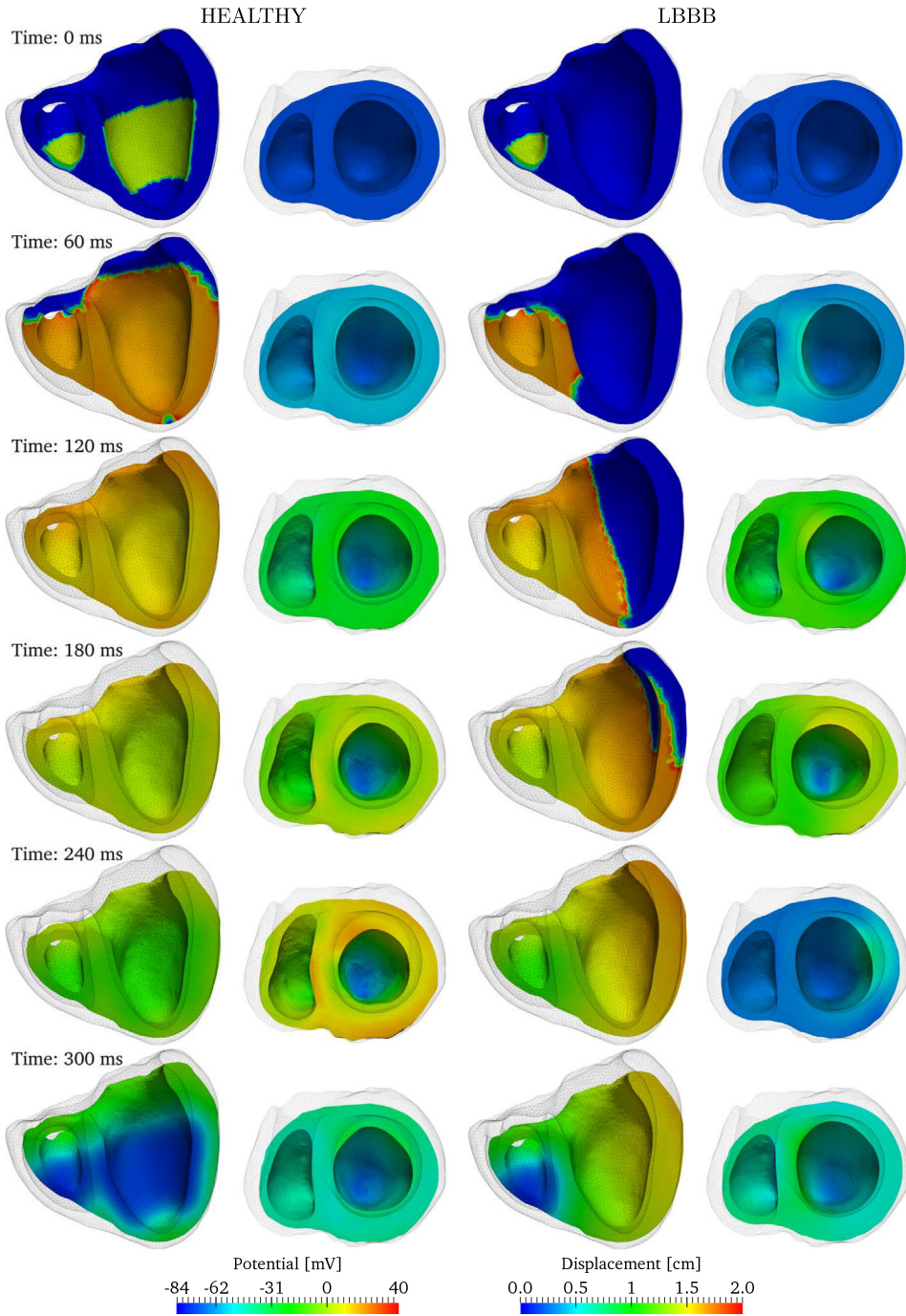


Fig. 6.13. In the simulation here reported, the left and right ventricles have been preloaded with a pressure of 8 mm Hg and 15 mm Hg, respectively, for both normal conditions (left columns) and LBBB (right columns). Snapshots of cardiac contraction: lateral views: evolution of the transmembrane potential over the deformed configuration and longitudinal shortening; top views; displacement field with respect to the preloaded configuration and wall thickening.

Imaging data were obtained from a 65-year-old female patient who had a hibernating myocardium and volume overload due to mitral regurgitation; the septal side of the LV was severely akinetic. Using a 1.5 T whole-body Siemens Avantoa MRI scanner, equipped with a commercial cardiac coil, electrocardiogram-gated breath-hold cine images of

the LV were acquired in multiple short axes using steady state free processing sequences (20 time frames/cardiac cycle, reconstruction matrix 256×256 pixels, in plane resolution $1.719 \times 1.719 \text{ mm}^2$, slice thickness 8 mm, gap 1.6 mm).

A model-based approach for constructing a computational LV geometry was used. The LV intracavitary volume mesh was obtained by morphing an idealized tetrahedral mesh representing the general LV shape by means of nonrigid deformations to fit the short-axis landmark points in the end-diastolic configuration. To represent the LV we used a truncated ellipsoid with short extruded sections extending from both valves, which were modeled as ellipsoidal surfaces. By an extrusion procedure a thin fictitious elastic structure around the endocardium was generated for the purpose of imposing the motion of the LV. The mitral valve annulus was approximated by an ellipsoid with major axis 3.5 cm and minor axis 2.6 cm at peak systole, whereas the aortic valve was approximated by a circle of diameter 1.8 cm.

The idealized LV was aligned and resized to match the position of the landmarks at end-diastolic configuration of the anatomically correct LV reconstructed from MRI. After alignment and resizing, the ideal LV geometry was nonrigidly deformed to fit the landmark points. This deformed configuration was then taken as the initial end-diastolic configuration. After the nonrigid deformation was applied to obtain the end-diastolic configuration that matched the position of the landmarks at the end-diastolic instant, the motion of the landmark points was extrapolated and used to drive the motion of the thin elastic structure of the LV in space and time to perform finite element simulations of the ventricular hemodynamics.

For mitral preload we imposed a constant pulmonary pressure of $p_{\text{pv}} = 10 \text{ mm Hg}$. For the ventricular afterload we used the standard three-element windkessel model (3.35). The venous pressure p_{ve} was fixed at 5 mm Hg. Valve Model A was used for the aortic valve in all three cases.

The LV FSI simulation was initialized at rest with zero velocity and pressure and driven for a few heartbeats at 75 bpm until pressure conditions stabilized into periodicity. The pulmonary pressure was ramped to 10 mm Hg in the course of the first 100 ms of the simulation to provide an impulse-free initialization, then kept constant for the rest of the run. No further initializations or regularizations needed to be performed. A fixed time step of 1 ms was used for the solution of the FSI problem with second-order backward differentiation formula in time. The finite element problem was discretized using 124 942 tetrahedral elements in the fluid domain and piecewise linear basis functions for both velocity and pressure approximation. Well-posedness of the problem was guaranteed by convective and pressure stabilization performed with the interior penalty method, see [246]. The peak Reynolds number inside the LV during the diastolic phase was around 2000, indicating transitional but not fully turbulent flow, and therefore no turbulence modeling was set up.

The velocity field and the diastolic jet for each of the three different valve models A, B and C is presented in Fig. 6.14 for three different time instances: early diastole, late diastole and early systole. In all three cases the diastolic jet is strongly driven towards the lateral wall and generates a large vortex near the aortic root that expands to fill the entire LV during the late diastolic A-wave. These features are independent of the inflow boundary condition applied (flow rate in Model A and pressure in Models B and C) and the opening dynamics of the mitral valve (MV). All three models exhibited vortical flow at the mitral inlet during early systole, but the numerical simulation remained stable and convergent throughout, indicating a successful stabilization of the inlet boundary condition during flow reversal. Failure to constrain the tangential velocity component according to (3.28) led to divergent solutions after a few heartbeats during either the opening or closing of the valve.

The mitral valve opening ratio, LV pressure and LV volume in time for the three different valve Models A, B and C are presented in Fig. 6.15. Model A stands apart from the other two due to the absence of mitral regurgitation, leading to larger systolic pressure and delayed opening of the MV by about 10 ms. The MV inflow is strongly bimodal and the A-wave is considerably stronger than the E-wave, which is consistent with clinical findings of chronic or compensated mitral regurgitation when the left atrium has to compensate for the diminished filling of the LV. Again, very little quantitative difference between Models B and C can be observed in terms of pressure and flow rate. This can be explained by the fact that the inflow/outflow volumetric flow rates are largely constrained by the imposed motion of the fictitious elastic structure that follows from the 4-D reconstruction. During valve closure each of the three models experienced severe local pressure oscillation.

Table 6.1 shows the regurgitant volume and its fraction of the total systolic outflow, the ejection fraction and the viscous dissipation. The predicted regurgitant volume is 9% higher in Model C, mainly due to the slower closure of the mitral valve. Peak viscous dissipation (PVD) is a quantity that can be used to measure the flow disturbance inside the LV. On the other hand, PVD during systole was slightly higher in Model A without regurgitation, but almost identical

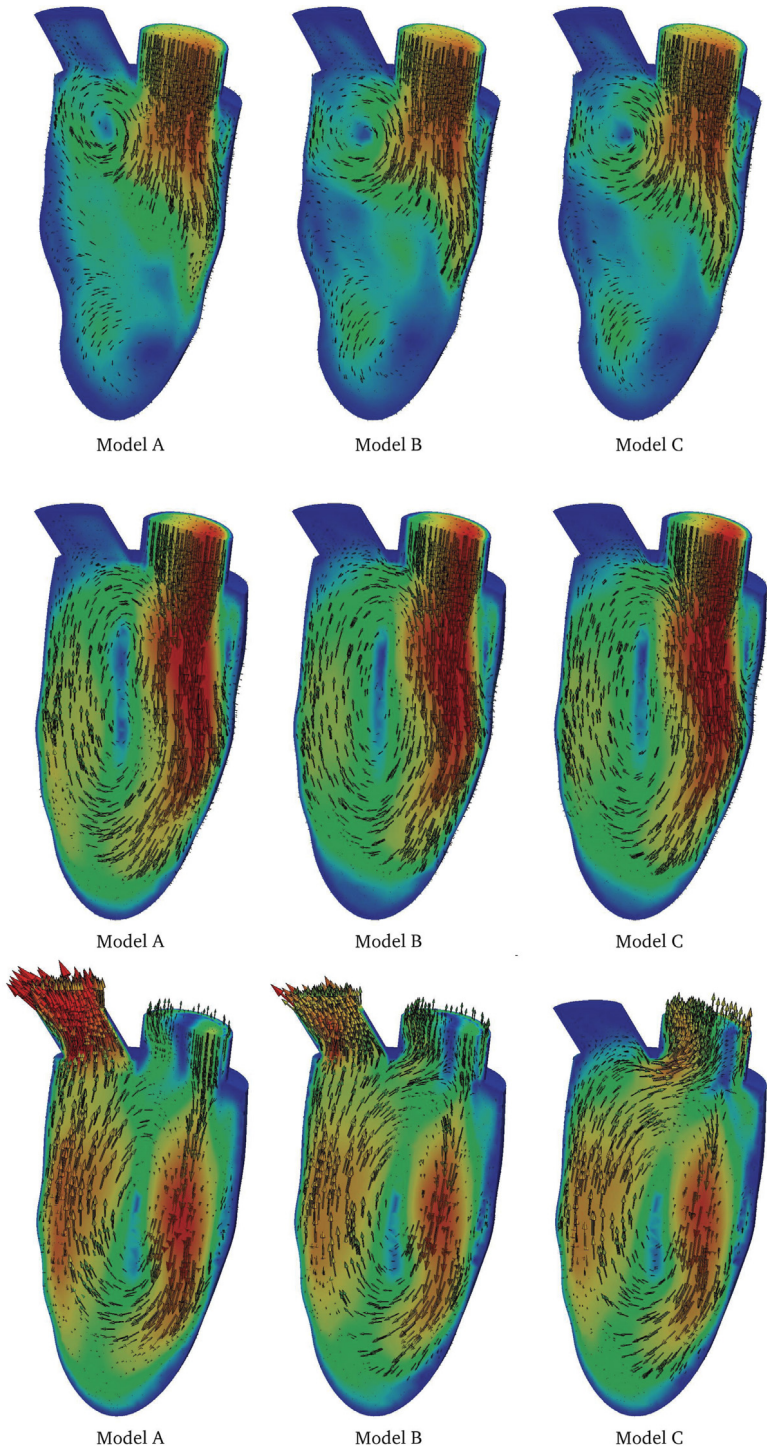


Fig. 6.14. Fluid dynamics of the LV under mitral valve insufficiency. Comparison of vortex jets for Models A, B and C. Top row: early diastolic velocity ($t = 550$ ms). Middle row: late diastolic velocity ($t = 750$ ms). Bottom row: early systolic velocity ($t = 800$ ms). Color bar ranges between 0 and 40 cm/s. (For interpretation of the references to colour in this figure legend, the reader is referred to the web version of this article.)

across all three models during diastole. The prediction of viscous dissipation depends on whether or not regurgitation is considered, but not on the specific opening/closing dynamics of the leaflets.

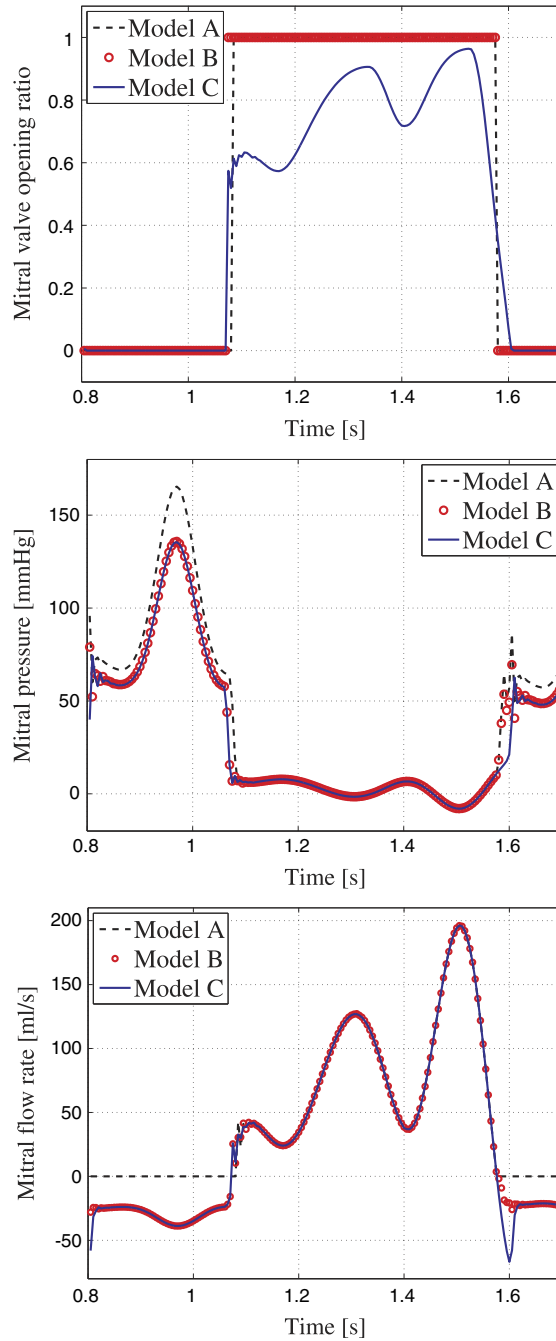


Fig. 6.15. Comparison of mitral valve characteristics for the valve Models A, B and C (top, center, bottom, respectively). The absence of mitral regurgitation in Model A leads to an increase of 19% in the prediction of systolic pressure peak pressure. The difference between the simple regurgitant valve (Model B) and the dynamic regurgitant valve (Model C) is negligible in terms of pressure and flow rate.

7. Discussion

In this article we have introduced some of the most basic components of what can be regarded as a mathematical model for the numerical simulation of heart functionality.

After a short description of the quantitative aspects of heart physiology we have first discussed the stand-alone mathematical models that are apt to represent the cardiac sub-systems: the propagation of the electric potential,

Table 6.1
Global indicators of mitral regurgitation as predicted by the different models.

Model	Regurgitant volume [ml]	Regurgitant fraction [%]	Ejection fraction [%]	Peak viscous dissipation [mW]
A	0.00	0.0%	28.9%	5.46 (s) / 0.666 (d)
B	8.02	19.7%	29.0%	4.21 (s) / 0.657 (d)
C	8.73	21.5%	28.9%	4.21 (s) / 0.659 (d)

the ionic current models for the action potential, the active contraction of individual cells for the generation of microscopic forces in the sarcomeres, the model that describes the passive mechanical response of the cardiac tissue, the fluid–structure interaction in the LV, and the mitral and aortic valve dynamics.

Integrating all these models together is essential to correctly describe the entire heart functionality. From a mathematical standpoint, the integration requires the set-up of suitable coupling conditions that can regulate the mechano-electrical feedback, the excitation–contraction process, the ventricular afterload, and the coupling with the systemic circulation.

The global coupled system is tremendously challenging to be analyzed mathematically and solved numerically. After recalling the most noticeable contributions to the mathematical analysis of the model components, we have proposed several instances of approximation methods and discussed their properties of stability and accuracy. In order to take advantage of the distinguishing features of each sub-component, we have addressed a possible strategy to design block preconditioners.

Finally, we have spanned a broad range of numerical simulations with the aim of verifying the numerical properties of the proposed algorithms and validating the suitability of our models to address situations of clinical relevance, both for physiological and pathological regimes.

We can readily identify several limitations of the models reviewed here, mainly in terms of physiological relevance. However our primary intention has been to introduce a prototype framework that could be progressively refined when required by a particular application. In this regard we first list some of the straightforward extensions to the model compartments we have been already studied in previous contributions [75,76,80]. Some specific aspects of modeling cardiac function that have not been covered include the fast conduction system (Purkinje network [247] and Purkinje-muscle junctions), cardiac perfusion [248] and its coupling with coronary flow [249,250], autoregulation aspects of heart rate [251], myocardial tissue damage and remodeling [252], the modeling of the atria [253–255], the heart-torso coupling that is needed for the simulation of an ECG [256,257,218], fluid dynamics in idealized ventricles [34,258,259], and many others. As discussed in Section 5.4, the outcome of multiphysics models strongly depends on the properties of the *coupling blocks* of the system. Here we have neglected some effects such as thermo-electric and size-dependent terms related to mechano-electric feedback, which could help in recovering fine features and common therapies associated to the electromechanical function, not obtained otherwise (such as therapeutic hypothermia, or the phenomenon where fibrillation is more easily performed low temperatures or the temperature-dependent minimum-size requirements in anti-arrhythmic therapies. See e.g. [56,260,261]). Another phenomenon not considered here, and affecting both ventricular contraction and hemodynamics, is the presence of papillary muscles or trabeculae. As discussed in [262], models including trabeculated tissue are characterized by a higher compliance with respect to the simpler models.

The current and future directions in computational modeling of total heart function are focused along several parallel tracks. Several groups around the world [263,264,5,265] are using massively parallel computing and especially graphics processing units to speed up the computations in realistic heart geometries using highly-detailed physiological electrophysiology models, with the ultimate goal of providing near real-time simulations. Alternatively, other efforts point to reducing the complexity of the underlying cellular models [266]. At the same time, high-order spatial approximations are actively studied [267–269] as an alternative to the low-order finite-element discretizations that lead to problem sizes in the hundreds of millions, and naturally provide a unified spatial approximation framework for electromechanics simulations. Recent multiscale models for the mechanics of cardiac tissue include [39,270].

If the challenge of computational complexity can be addressed, this would open new opportunities in the personalization of models to answer clinical questions, since we would be at a point where simulations and experiments agree at a large extent. Current ways of performing personalization include estimation of fiber directions from imaging modalities such as diffusion MRI [211], as well as data assimilation of cardiac motion from imaging into

electromechanics simulations through unscented Kalman filters [271,272]. Meanwhile, in the cardiac fluid dynamics community more and more advanced patient-specific valve models incorporating fluid–structure interaction are being developed [273,274,95,275–277,114], and may in the future be incorporated into full-heart computational models to study the joint effect of valve function and cardiac mechanics.

Despite these impressive recent advances, we believe that a clear and consistent understanding of the multiscale nature of the heart function involving heterogeneity and specific models for individual cells and integration with all salient scales of structural complexity, is still far beyond reach.

Acknowledgments

We gratefully acknowledge the support by the European Research Council through the advanced grant “MATHCARD, Mathematical Modelling and Simulation of the Cardiovascular System”, ERC-2008-AdG 227058 (<http://www.mathcard.eu>). We thank P. Tricerri, S. Pezzuto, and A.C.I. Malossi, for their valuable help in the implementation of the structural solver, orthotropic material law, multiscale framework, respectively, and A. Di Blasio for the stability assessment of coupling simplified models discussed in Section 5.4. The mitral valve insufficiency study of Section 6.7 was performed in collaboration with S. Deparis, A. Redaelli, M. Stevanella, and E. Votta, and clinical data was provided by the team of Prof. O. Parodi at Ospedale Niguarda, Milan, Italy with the support of the European Community 7th Framework Programme, Project FP7-224635 VPH2 (“Virtual Pathological Heart of the Virtual Physiological Human”) and the Swiss Platform for High-Performance and High-Productivity Computing (HP2C). All simulations presented in this paper have been carried out using the LGPL library LifeV (<http://www.lifev.org>).

References

- [1] A.L. Goldberger, L.A. Amaral, L. Glass, J.M. Hausdorff, P.C. Ivanov, R.G. Mark, J.E. Mietus, G.B. Moody, C.K. Peng, H.E. Stanley, Current perspective: Physiobank, physiotoolkit, and physionet components of a new research resource for complex physiologic signals, *Circulation* 101 (2000) e215–e220.
- [2] E.J. Vigmond, C. Clements, D. McQueen, C.S. Peskin, Effect of bundle branch block on cardiac output: a whole heart simulation study, *Prog. Biophys. Mol. Biol.* 97 (2) (2008) 520–542.
- [3] H. Watanabe, S. Sugiura, T. Hisada, Multiphysics simulation of left ventricular filling dynamics using fluid–structure interaction finite element method, *Biophys. J.* 87 (2004) 2074–2085.
- [4] D.A. Nordsletten, S.A. Niederer, M.P. Nash, P.J. Hunter, N.P. Smith, Coupling multi-physics models to cardiac mechanics, *Prog. Biophys. Mol. Biol.* 104 (2011) 77–88.
- [5] S. Sugiura, T. Washio, A. Hatano, J. Okada, H. Watanabe, T. Hisada, Multi-scale simulations of cardiac electrophysiology and mechanics using the University of Tokyo heart simulator, *Prog. Biophys. Mol. Biol.* 110 (2012) 380–389.
- [6] V. Mihailef, R.I. Ionasec, P. Sharma, B. Georgescu, I. Voigt, M. Suehling, D. Comaniciu, Patient-specific modelling of whole heart anatomy, dynamics and haemodynamics from four-dimensional cardiac CT images, *Interface Focus* 1 (3) (2011) 286–296.
- [7] T. Schenkel, M. Malve, M. Reik, M. Markl, B. Jung, H. Oertel, MRI-based CFD analysis of flow in a human left ventricle: methodology and application to a healthy heart, *Ann. Biomed. Eng.* 37 (3) (2009) 503–515.
- [8] D. Tang, C. Yang, T. Geva, P.J. del Nido, Image-based patient-specific ventricle models with fluid–structure interaction for cardiac function assessment and surgical design optimization, *Prog. Pediatr. Cardiol.* 30 (1) (2010) 51–62.
- [9] J.P. Keener, J. Sneyd, *Mathematical Physiology—Systems Physiology*, Springer-Verlag, Berlin, 1998.
- [10] F.H. Fenton, E.M. Cherry, L. Glass, Cardiac arrhythmia, *Scholarpedia* 3 (2008) 1665.
- [11] J. Lee, S. Niederer, D. Nordsletten, I. Le Grice, B. Smaill, D. Kay, N.P. Smith, Coupling contraction, excitation, ventricular and coronary blood flow across scale and physics in the heart, *Philos. Trans. R. Soc. Lond. Ser. A* 367 (2009) 2311–2331.
- [12] N.A. Trayanova, Whole-heart modeling: Applications to cardiac electrophysiology and electromechanics, *Circ. Res.* 108 (2011) 113–128.
- [13] O. Bergmann, R.D. Bhardwaj, S. Bernard, S. Zdunek, F. Barnabé-Heider, S. Walsh, J. Zupicich, K. Alkass, B.A. Buchholz, H. Druid, et al., Evidence for cardiomyocyte renewal in humans, *Science* 324 (5923) (2009) 98–102.
- [14] S. Ausoni, S. Sartore, The cardiovascular unit as a dynamic player in disease and regeneration, *Trends Mol. Med.* 15 (12) (2009) 543–552.
- [15] F. Torrent-Guasp, Sobre morfología y funcionalismo cardíacos, *Rev. Esp. Cardiol.* 20 (1967) 14.
- [16] F. Torrent-Guasp, M.J. Kocica, A.F. Corno, M. Komeda, F. Carreras-Costa, A. Flotats, J. Cosin-Aguilar, H. Wen, Towards new understanding of the heart structure and function, *Eur. J. Cardiothorac. Surg.* 27 (2) (2005) 191–201.
- [17] D.D. Streeter, W.E. Powers, M.A. Ross, F. Torrent-Guasp, Three dimensional fiber orientation in the mammalian left ventricular wall, in: J. Baan, A. Noordergraaf, J. Raines (Eds.), *Cardiovascular System Dynamics*, M.I.T. Press, Cambridge, 1978, pp. 73–84.
- [18] P. Colli Franzone, L.F. Pavarino, S. Scacchi, Mathematical and numerical methods for reaction–diffusion models in electrocardiology, in: D. Ambrosi, et al. (Eds.), *Modeling of Physiological Flows*, Springer, 2012.
- [19] T.S.E. Eriksson, A.J. Prassl, G. Plank, G.A. Holzapfel, Influence of myocardial fiber/sheet orientations on left ventricular mechanical contraction, *Math. Mech. Solids* 18 (2013) 592–606.
- [20] C.S. Peskin, Fiber architecture of the left ventricular wall: an asymptotic analysis, *Comm. Pure Appl. Math.* 42 (1989) 79–113.

- [21] S.F. Pravdin, V.I. Berdyshev, A.V. Panfilov, L.B. Katsnelson, O. Solovyova, V.S. Markhasin, Mathematical model of the anatomy and fibre orientation field of the left ventricle of the heart, *Biomed. Eng. Online* 12 (1) (2013) 54.
- [22] M. Sermesant, P. Moireau, O. Camara, J. Sainte-Marie, R. Andriantsimavona, R. Cimrman, D.L.G. Hill, D. Chapelle, R. Razavi, Cardiac function estimation from MRI using a heart model and data assimilation: advances and difficulties, *Med. Image Anal.* 10 (4) (2006) 642–656.
- [23] I.J. LeGrice, B.H. Smaill, L.Z. Chai, S.G. Edgar, J.B. Gavin, P.J. Hunter, Laminar structure of the heart: ventricular myocyte arrangement and connective tissue architecture in the dog, *Am. J. Physiol. Heart Circ. Physiol.* 269 (2) (1995) H571–H582.
- [24] M.R. Guevara, L. Glass, A. Shrier, Phase locking, period-doubling bifurcations, and irregular dynamics in periodically stimulated cardiac cells, *Science* 214 (1981) 1350–1353.
- [25] A.T. Winfree, *The Geometry of Biological Time*, Springer-Verlag, New York, 2000.
- [26] S. Walcott, S. Sun, Hysteresis in cross-bridge models of muscle, *Phys. Chem. Chem. Phys.* 11 (24) (2009) 4871–4881.
- [27] A.F. Huxley, Muscle structure and theories of contraction, *Prog. Biophys. Biophys. Chem.* 7 (1957) 255–318.
- [28] T. Washio, J.I. Okada, S. Sugiura, T. Hisada, Approximation for cooperative interactions of a spatially-detailed cardiac sarcomere model, *Cell Mol. Bioengrg.* 5 (1) (2012) 113–126.
- [29] M. Fink, S.A. Niederer, E.M. Cherry, F.H. Fenton, J.T. Koivumäki, G. Seemann, R. Thul, H. Zhang, F.B. Sachse, D. Beard, E.J. Crampin, N.P. Smith, Cardiac cell modelling: Observations from the heart of the cardiac physiome project, *Prog. Biophys. Mol. Biol.* 104 (2011) 2–21.
- [30] J.A. Negroni, E.C. Lascano, Simulation of steady state and transient cardiac muscle response experiments with a huxley-based contraction model, *J. Mol. Cell. Cardiol.* 45 (2008) 300–312.
- [31] J.J. Rice, F. Wang, D.M. Bers, P.P. de Tombe, Approximate model of cooperative activation and crossbridge cycling in cardiac muscle using ordinary differential equations, *Biophys. J.* 95 (2008) 2368–2390.
- [32] J. Bestel, F. Clément, M. Sorine, A biomechanical model of muscle contraction, in: W.J. Niessen, M.A. Viergever (Eds.), *Medical Image Computing and Computer Assisted Intervention*, Springer, Berlin, Heidelberg, 2001, pp. 1159–1161.
- [33] Z. Qu, G. Hub, A. Garfinkel, J.N. Weiss, Nonlinear and stochastic dynamics in the heart, *Phys. Rep.* 543 (2014) 61–162.
- [34] G. Pedrizzetti, F. Domenichini, Nature optimizes the swirling flow in the human left ventricle, *Phys. Rev. Lett.* 95 (10) (2005) 108101.
- [35] J.H. Seo, R. Mittal, Effect of diastolic patterns on the function of the left ventricle, *Phys. Fluids* 25 (2013) 110801.
- [36] H. Watanabe, S. Sugiura, T. Hisada, The looped heart does not save energy by maintaining the momentum of blood flowing in the ventricle, *Am. J. Physiol.-Heart C.* 294 (5) (2009) H2191–H2196.
- [37] G.W. Jones, S.J. Chapman, Modeling growth in biological materials, *SIAM Rev.* 54 (1) (2012) 52–118.
- [38] D. Sato, C.E. Clancy, Cardiac electrophysiological dynamics from the cellular level to the organ level, *Biomed. Eng. Comput. Biol.* 5 (2013) 69–75.
- [39] R. Chabiniok, V.Y. Wang, M. Hadjicharalambous, L. Asner, J. Lee, M. Sermesant, E. Kuhl, A.A. Young, P. Moireau, M.P. Nash, D. Chapelle, D.A. Nordsletten, Multiphysics and multiscale modeling, data-model fusion and integration of organ physiology in the clinic: ventricular cardiac mechanics, *Interface Focus* 6 (2016) 1–24.
- [40] M. Golob, R.L. Moss, N.C. Chesler, Cardiac tissue structure, properties, and performance: a materials science perspective, *Ann. Biomed. Eng.* 42 (2014) 2003–2013.
- [41] C.S. Peskin, Flow patterns around heart valves: a numerical method, *J. Comput. Phys.* 10 (1972) 252–271.
- [42] C.S. Peskin, The immersed boundary method, *Acta Numer.* 11 (2002) 479–517.
- [43] S. Severi, B. Rodriguez, A. Zaza, Computational cardiac electrophysiology is ready for prime time, *Europace* 16 (3) (2014) 382–383.
- [44] P. Colli Franzone, L.F. Pavarino, A parallel solver for reaction–diffusion systems in computational electro-cardiology, *Math. Models Methods Appl. Sci.* 14 (2004) 883–911.
- [45] R.J. Spiteri, R.C. Dean, Stiffness analysis of cardiac electrophysiological models, *Ann. Biomed. Eng.* 38 (12) (2010) 3592–3604.
- [46] W. Hundsdorfer, J. Verwer, *Numerical Solution of Time-Dependent Advection-Diffusion-Reaction Equations*, Springer-Verlag, Berlin, Heidelberg, 2003.
- [47] A. Quarteroni, R. Sacco, F. Saleri, *Numerical Mathematics*, second ed., in: *Texts in Applied Mathematics*, vol. 37, Springer-Verlag, Berlin, 2007.
- [48] S. Land, S.A. Niederer, N.P. Smith, Efficient computational methods for strongly coupled cardiac electromechanics, *IEEE Trans. Biomed. Eng.* 59 (5) (2012) 1219–1228.
- [49] K.H.W.J. Ten Tusscher, A.V. Panfilov, Cell model for efficient simulation of wave propagation in human ventricular tissue under normal and pathological conditions, *Phys. Med. Biol.* 51 (23) (2006) 6141–6156.
- [50] S. Rush, H. Larsen, A practical algorithm for solving dynamic membrane equations, *IEEE Trans. Biomed. Eng.* 4 (1978) 389–392.
- [51] P. Colli Franzone, L.F. Pavarino, S. Scacchi, *Mathematical Cardiac Electrophysiology*, Springer MS&A, 2014.
- [52] R.H. Clayton, O. Bernus, E.M. Cherry, H. Dierckx, F.H. Fenton, L. Mirabella, A.V. Panfilov, F.B. Sachse, G. Seemann, H. Zhang, Models of cardiac tissue electrophysiology: progress, challenges and open questions, *Prog. Biophys. Mol. Biol.* 104 (1) (2011) 22–48.
- [53] A. Bueno-Orovio, E.M. Cherry, F.H. Fenton, Minimal model for human ventricular action potential in tissue, *J. Theoret. Biol.* 253 (2008) 544–560.
- [54] T. Lassila, M. Lange, A.T. Porras, K. Lekadir, X. Alba, A.F. Frangi, Electrophysiology model for a human heart with ischemic scar and realistic Purkinje network, in: O. Camara, T. Mansi, M. Pop, K. Rhode, M. Sermesant, A. Young (Eds.), *Proceedings of 6th International Workshop, STACOM 2015, Held in Conjunction with MICCAI 2015, Munich, Germany, October 9, 2015, Revised Selected Papers*, in: LNCS, vol. 9534, Springer International Publishing, 2015.
- [55] F.H. Fenton, A. Gizzi, C. Cherubini, N. Pomella, S. Filippi, Role of temperature on nonlinear cardiac dynamics, *Phys. Rev. E* 87 (2013) 042717.
- [56] S. Filippi, A. Gizzi, C. Cherubini, S. Luther, F.H. Fenton, Mechanistic insights into hypothermic ventricular fibrillation: the role of temperature and tissue size, *Europace* 16 (2014) 424–434.
- [57] S. Rossi, T. Lassila, R. Ruiz-Baier, A. Sequeira, A. Quarteroni, Thermodynamically consistent orthotropic activation model capturing ventricular systolic wall thickening in cardiac electromechanics, *Eur. J. Mech. A Solids* 48 (2014) 129–142.

- [58] D. Romero, R. Sebastian, B.H. Bijnens, V. Zimmerman, P.M. Boyle, E.J. Vigmond, A.F. Frangi, Effects of the Purkinje system and cardiac geometry on biventricular pacing: a model study, *Ann. Biomed. Eng.* 38 (4) (2010) 1388–1398.
- [59] C. Vergara, S. Palamara, M. Lange, T. Lassila, A.F. Frangi, A. Quarteroni, A coupled 3D-1D numerical monodomain solver for cardiac electrical activation in the myocardium with detailed Purkinje network, *J. Comput. Phys.* 308 (2016) 218–238.
- [60] A. Bueno-Orovio, D. Kay, V. Grau, B. Rodriguez, K. Burrage, Fractional diffusion models of cardiac electrical propagation: role of structural heterogeneity in dispersion of repolarization, *J. R. Soc. Interface* 11 (2014) 97.
- [61] D.E. Hurtado, S. Castro, A. Gizzi, Computational modeling of non-linear diffusion in cardiac electrophysiology: A novel porous-medium approach, *Comput. Methods Appl. Mech. Engrg.* 300 (2016) 70–83.
- [62] U. Mehlhorn, H.J. Geissler, G.A. Laine, S.J. Allen, Myocardial fluid balance, *Eur. J. Cardiothoracic Surg.* 20 (6) (2001) 1220–1230.
- [63] H. Ashikaga, B.A. Coppola, K.G. Yamazaki, F.J. Villarreal, J.H. Omens, J.W. Covell, Changes in regional myocardial volume during the cardiac cycle: implications for transmural blood flow and cardiac structure, *Am. J. Physiol. Heart Circ. Physiol.* 295 (2008) H610–H618.
- [64] J.M. Guccione, K.D. Costa, A.D. McCulloch, Finite element stress analysis of left ventricular mechanics in the beating dog heart, *J. Biomech.* 28 (10) (1995) 1167–1177.
- [65] R.F. Janz, B.R. Kubert, T.F. Moriarty, A.F. Grimm, Deformation of the diastolic left ventricle II: Nonlinear geometric effects, *J. Biomech.* 7 (1974) 509–516.
- [66] G.A. Holzapfel, R.W. Ogden, Constitutive modelling of passive myocardium: a structurally based framework for material characterization, *Philos. Trans. R. Soc. Lond. Ser. A* 367 (2009) 3445–3475.
- [67] A. Goriely, M. Tabor, Rotation, inversion and perversion in anisotropic elastic cylindrical tubes and membranes, *Proc. Roy. Soc. A* 469 (2013) 20130011.
- [68] D.H. Cortes, D.M. Elliot, Accurate prediction of stress in fibers with distributed orientations using generalized high-order structure tensors, *Mech. Mater.* 75 (2014) 73–83.
- [69] A. Gizzi, A. Pandolfi, M. Vasta, Statistical characterization of the anisotropic strain energy in soft materials with distributed fibers, *Mech. Mater.* 92 (2016) 119–138.
- [70] C. Sansour, On the physical assumptions underlying the volumetric-isochoric split and the case of anisotropy, *Eur. J. Mech. A Solids* 27 (1) (2008) 29–39.
- [71] J. Helfenstein, M. Jabareen, E. Mazza, S. Govindjee, On non-physical response in models for fiber-reinforced hyperelastic materials, *Int. J. Solids Struct.* 47 (16) (2010) 2056–2061.
- [72] D. Ambrosi, S. Pezzuto, Active stress vs. active strain in mechanobiology: Constitutive issues, *J. Elasticity* 107 (2012) 199–212.
- [73] C. Cherubini, S. Filippi, P. Nardinocchi, L. Teresi, An electromechanical model of cardiac tissue: Constitutive issues and electrophysiological effects, *Prog. Biophys. Mol. Biol.* 97 (2008) 562–573.
- [74] P. Nardinocchi, L. Teresi, On the active response of soft living tissues, *J. Elasticity* 88 (2007) 27–39.
- [75] F. Nobile, A. Quarteroni, R. Ruiz-Baier, An active strain electromechanical model for cardiac tissue, *Int. J. Numer. Methods Biomed. Eng.* 28 (2012) 52–71.
- [76] S. Rossi, R. Ruiz-Baier, L.F. Pavarino, A. Quarteroni, Orthotropic active strain models for the numerical simulation of cardiac biomechanics, *Int. J. Numer. Meth. Biomed. Engrg.* 28 (2012) 761–788.
- [77] A.M. Katz, Ernest Henry Starling, his predecessors, and the “Law of the Heart”, *Circulation* 106 (23) (2002) 2986–2992.
- [78] A. Gizzi, C. Cherubini, S. Filippi, A. Pandolfi, Theoretical and numerical modeling of nonlinear electromechanics with applications to biological active media, *Commun. Comput. Phys.* 17 (2015) 93–126.
- [79] S. Göktepe, A. Menzel, E. Kuhl, Micro-structurally based kinematic approaches to electromechanics of the heart, in: *Computer Models in Biomechanics*, Springer, Netherlands, 2013, pp. 175–187.
- [80] R. Ruiz-Baier, A. Gizzi, S. Rossi, C. Cherubini, A. Laadhari, S. Filippi, A. Quarteroni, Mathematical modeling of active contraction in isolated cardiomyocytes, *Math. Medicine Biol.* 31 (3) (2014) 259–283.
- [81] J.E. Strobeck, E.H. Sonnenblick, Myocardial contractile properties and ventricular performance, in: H.A. Fozzard, et al. (Eds.), *The Heart and Cardiovascular System*, Raven Press, New York, 1986.
- [82] A.V. Hill, The heat of shortening and the dynamic constants of muscle, *Proc. R. Soc. B* 126 (843) (1938) 136–195.
- [83] J. Sainte-Marie, D. Chapelle, R. Cimrman, M. Sorine, Modeling and estimation of the cardiac electromechanical activity, *Comput. Struct.* 84 (28) (2006) 1743–1759.
- [84] B. Bhattacharya-Ghosh, S. Schievano, V. Diaz-Zuccarini, A multi-physics and multi-scale lumped parameter model of cardiac contraction of the left ventricle: A conceptual model from the protein to the organ scale, *Comput. Biol. Med.* 42 (10) (2012) 982–992.
- [85] F.E. Rademakers, W.J. Rogers, W.H. Guier, G.M. Hutchins, C.O. Siu, M.L. Weisfeldt, J.L. Weiss, E.P. Shapiro, Relation of regional cross-fiber shortening to wall thickening in the intact heart. Three-dimensional strain analysis by NMR tagging, *Circulation* 89 (1994) 1174–1182.
- [86] N.A. Trayanova, W. Li, J. Eason, P. Kohl, Effect of stretch-activated channels on defibrillation efficacy, *Heart Rhythm* 1 (1) (2004) 67–77.
- [87] R.H. Keldermann, M.P. Nash, A.V. Panfilov, Modeling cardiac mechano-electrical feedback using reaction-diffusion-mechanics systems, *Physica D* 238 (11) (2009) 1000–1007.
- [88] F. Bode, A. Katchman, R.L. Wooley, M.R. Franz, Gadolinium decreases stretch-induced vulnerability to atrial fibrillation, *Circulation* 101 (18) (2000) 2200–2205.
- [89] F. Sachs, Stretch-activated ion channels: What are they? *Physiol.* 25 (2010) 50–56.
- [90] G. Dominguez, H.A. Fozzard, Effect of stretch on conduction velocity and cable properties of cardiac Purkinje fibers, *Am. J. Physiol.-Cell. Ph.* 237 (3) (1979) C119–C124.
- [91] D. Sung, R.W. Mills, J. Schettler, S.M. Narayan, J.H. Omens, A.D. McCulloch, Ventricular filling slows epicardial conduction and increases action potential duration in an optical mapping study of the isolated rabbit heart, *J. Cardiovasc. Electrophysiol.* 14 (7) (2003) 739–749.
- [92] N.H.L. Kuijpers, H.M.M. ten Eikelder, P.H.M. Bovendeerd, S. Verheule, T. Arts, P.A.J. Hilbers, Mechanoelectric feedback leads to conduction slowing and block in acutely dilated atria: a modeling study of cardiac electromechanics, *Am. J. Physiol.-Cell Phys.* 61 (6) (2007) H2832.

- [93] R. Mills, S.M. Narayan, A.D. McCulloch, Mechanisms of conduction slowing during myocardial stretch by ventricular volume loading in the rabbit, *Am. J. Physiol. Heart Circ. Physiol.* 295 (3) (2008) H1270.
- [94] Y. Cheng, H. Oertel, T. Schenkel, Fluid–structure coupled CFD simulation of the left ventricular flow during filling phase, *Ann. Biomed. Eng.* 33 (2005) 567–576.
- [95] C. Chnafa, S. Mendez, F. Nicoud, Image-based large-eddy simulation in a realistic left heart, *Comput. Fluids* 94 (2014) 173–187.
- [96] L. Formaggia, A. Quarteroni, A. Veneziani, *Cardiovascular Mathematics*, in: *MS&A: Modeling, Simulation and Applications*, vol. I, Springer, Heidelberg, 2009.
- [97] B. Su, L. Zhong, X.-K. Wang, J.-M. Zhang, R.S. Tan, J.C. Allen, S.K. Tan, S. Kim, H.L. Leo, Numerical simulation of patient-specific left ventricular model with both mitral and aortic valves by FSI approach, *Comput. Methods Programs Biomed.* 113 (2) (2014) 474–482.
- [98] S.J. Kovács, D.M McQueen, C.S. Peskin, Modelling cardiac fluid dynamics and diastolic function, *Philos. Trans. R. Soc. Lond. Ser. A* 359 (1783) (2001) 1299–1314.
- [99] V.Y. Wang, H.I. Lam, D.B. Ennis, B.R. Cowan, A.A. Young, M.P. Nash, Modelling passive diastolic mechanics with quantitative MRI of cardiac structure and function, *Med. Image Anal.* 13 (5) (2009) 773–784.
- [100] P. Moireau, N. Xiao, M. Astorino, C.A. Figueiredo, D. Chapelle, C.A. Taylor, J.-F. Gerbeau, External tissue support and fluid–structure simulation in blood flows, *Biomech. Model. Mechanobiol.* 11 (1–2) (2012) 1–18.
- [101] T. Fritz, C. Wieners, G. Seemann, H. Steen, O. Dössel, Simulation of the contraction of the ventricles in a human heart model including atria and pericardium, *Biomech. Model. Mechanobiol.* 3 (3) (2014) 627–641.
- [102] L. Formaggia, J.-F. Gerbeau, F. Nobile, A. Quarteroni, Numerical treatment of defective boundary conditions for the Navier–Stokes equation, *SIAM J. Numer. Anal.* 40 (1) (2002) 376–401.
- [103] A. Quarteroni, A. Veneziani, C. Vergara, Geometric multiscale modelling of the cardiovascular system, between theory and practice, *Comput. Methods Appl. Mech. Engrg.* 302 (2016) 193–252.
- [104] M.E. Moghadam, Y. Bazilevs, T.-Y. Hsia, I.E. Vignon-Clementel, A.L. Marsden, A comparison of outlet boundary treatments for prevention of backflow divergence with relevance to blood flow simulations, *Comput. Mech.* 48 (2011) 277–291.
- [105] J.P. Mynard, M.R. Davidson, D.J. Penny, J.J. Smolich, A simple, versatile valve model for use in lumped parameter and one-dimensional cardiovascular models, *Int. J. Numer. Methods Biomed. Eng.* 28 (6–7) (2012) 626–641.
- [106] M. Nakamura, S. Wada, T. Yamaguchi, Influence of the opening mode of the mitral valve orifice on intraventricular hemodynamics, *Ann. Biomed. Eng.* 34 (6) (2006) 927–935.
- [107] B. Baccani, F. Domenichini, G. Pedrizzetti, G. Tonti, Model and influence of mitral valve opening during the left ventricular filling, *J. Biomech.* 36 (3) (2003) 355–361.
- [108] M. Astorino, J. Hamers, S.C. Shadden, J.-F. Gerbeau, A robust and efficient valve model based on resistive immersed surfaces, *Int. J. Numer. Methods Biomed. Eng.* 28 (9) (2012) 937–959.
- [109] X. Ma, H. Gao, B.E Griffith, C. Berry, X. Luo, Image-based fluid–structure interaction model of the human mitral valve, *Comput. Fluids* 71 (2013) 417–425.
- [110] A. Aggarwal, G. Ferrari, E. Joyce, M.J. Daniels, R. Sainger, J.H. Gorman, R. Gorman, M.S. Sacks, Architectural trends in the human normal and bicuspid aortic valve leaflet and its relevance to valve disease, *Ann. Biomed. Eng.* 42 (5) (2014) 986–998.
- [111] R.M. Buchanan, M.S. Sacks, Interlayer micromechanics of the aortic heart valve leaflet, *Biomech. Model. Mechanobiol.* 13 (4) (2014) 813–826.
- [112] M.C. Hsu, D. Kamensky, Y. Bazilevs, M.S. Sacks, T.J.R. Hughes, Fluid–structure interaction analysis of bioprosthetic heart valves: significance of arterial wall deformation, *Comput. Mech.* 54 (2014) 1055–1071.
- [113] D. Kamensky, M.-C. Hsu, D. Schillinger, J.A. Evans, A. Aggarwal, Y. Bazilevs, M.S. Sacks, T.J.R. Hughes, A variational immersed boundary framework for fluid–structure interaction: isogeometric implementation and application to bioprosthetic heart valves, *Comput. Methods Appl. Mech. Engrg.* 284 (2015) 1005–1053.
- [114] E. Votta, T.B. Le, M. Stevanella, L. Fusini, E.G. Caiani, A. Redaelli, F. Sotiropoulos, Toward patient-specific simulations of cardiac valves: State-of-the-art and future directions, *J. Biomech.* 46 (2) (2013) 217–228.
- [115] N. Westerhof, G.I.J.S. Elzinga, P. Sipkema, An artificial arterial system for pumping hearts, *J. Appl. Physiol.* 31 (5) (1971) 776–781.
- [116] N. Stergiopoulos, B.E. Westerhof, N. Westerhof, Total arterial inertance as the fourth element of the windkessel model, *Am. J. Physiol.-Heart C* 276 (1) (1999) H81–H88.
- [117] Y. Shi, P. Lawford, R. Hose, Review of zero-D and 1-D models of blood flow in the cardiovascular system, *Biomed. Engrg. Online* 10 (2011) 33.
- [118] J. Alastruey, K.H. Parker, J. Peiró, S.J. Sherwin, Lumped parameter outflow models for 1-D blood flow simulations: Effect on pulse waves and parameter estimation, *Commun. Comput. Phys.* 4 (2008) 317–336.
- [119] P.J. Blanco, P.R. Trenhago, L.G. Fernandes, R.A. Feijóo, On the integration of the baroreflex control mechanism in a heterogeneous model of the cardiovascular system, *Int. J. Numer. Methods Biomed. Eng.* 28 (4) (2012) 412–433.
- [120] P.J. Blanco, S.M. Watanabe, M.A. Passos, P.A. Lemos, R.A. Feijóo, An anatomically detailed arterial network model for one-dimensional computational hemodynamics, *IEEE Trans. Biomed. Eng.* 62 (2) (2015) 736–753.
- [121] L. Grinberg, T. Anor, J.R. Madsen, A. Yakhot, G.E. Karniadakis, Large-scale simulation of the human arterial tree, *Clinical Exper. Pharmacol. Physiol.* 36 (2) (2008) 194–205.
- [122] N. Xiao, J.D. Humphrey, A.C. Figueiredo, Multi-scale computational model of three-dimensional hemodynamics within a deformable full-body arterial network, *J. Comput. Phys.* 244 (2013) 22–40.
- [123] N.J.B. Driessens, M.A.J. Cox, C.V.C. Bouting, F.P.T. Baaijens, Remodelling of the angular collagen fiber distribution in cardiovascular tissues, *Biomech. Model. Mechanobiol.* 7 (2008) 93–103.
- [124] F.P.T. Baaijens, C.V.C. Bouting, N.J.B. Driessens, Modeling collagen remodeling, *J. Biomech.* 43 (2010) 166–175.
- [125] L. Formaggia, A. Quarteroni, C. Vergara, On the physical consistency between three-dimensional and one-dimensional models in haemodynamics, *J. Comput. Phys.* 244 (2013) 97–112.

- [126] P. Colli Franzone, G. Savaré, Degenerate evolution systems modeling the cardiac electric field at micro- and macroscopic level, in: Evolution Equations, Semigroups and Functional Analysis, Milano (2000), in: Progr. Nonlinear Differential Equations Appl., vol. 50, Birkhäuser, 2002, pp. 49–78.
- [127] M. Bendahmane, K.H. Karlsen, Analysis of a class of degenerate reaction–diffusion systems and the bidomain model of cardiac tissue, *Netw. Heterog. Media* 1 (2006) 185–218.
- [128] M. Boulakia, M.A. Fernández, J.-F. Gerbeau, N. Zemzemi, A coupled system of PDEs and ODEs arising in electrocardiograms modeling, *Appl. Math. Res. Express. AMRX* 2 (2008) 28.
- [129] Y. Bourgault, Y. Coudière, C. Pierre, Existence and uniqueness of the solution for the bidomain model used in cardiac electrophysiology, *Nonlinear Anal. RWA* 10 (2009) 458–482.
- [130] H. Matano, Y. Mori, Global existence and uniqueness of a three-dimensional model of cellular electrophysiology, *Discrete Contin. Dyn. Syst.* 29 (2011) 1573–1636.
- [131] J. Sundnes, G.T. Lines, X. Cai, B.F. Nielsen, K.-A. Mardal, A. Tveito, Computing the electrical activity in the heart, in: Monographs in Computational Science and Engineering, vol. 1, Springer-Verlag, Berlin, 2006.
- [132] M. Veneroni, Reaction–diffusion systems for the macroscopic bidomain model of the cardiac electric field, *Nonl. Anal.: Real World Appl.* 10 (2009) 849–868.
- [133] D.E. Hurtado, D. Henao, Gradient flows and variational principles for cardiac electrophysiology: toward efficient and robust numerical simulations of the electrical activity of the heart, *Comput. Methods Appl. Mech. Engrg.* 273 (2014) 238–254.
- [134] D.G. Ebin, Global solutions of the equations of elastodynamics of incompressible neo-hookean materials, *Proc. Natl. Acad. Sci. USA* 90 (1993) 3802–3805.
- [135] P. Le Tallec, Existence and approximation results for nonlinear mixed problems: Application to incompressible finite elasticity, *Numer. Math.* 38 (1982) 365–382.
- [136] J.M. Ball, Convexity conditions and existence theorems in nonlinear elasticity, *Arch. Ration. Mech. Anal.* 63 (1976/77) 337–403.
- [137] D. Baroli, A. Quarteroni, R. Ruiz-Baier, Convergence of a stabilized discontinuous galerkin method for incompressible nonlinear elasticity, *Adv. Comput. Math.* 39 (2013) 425–443.
- [138] P. Krejčí, J. Sainte-Marie, M. Sorine, J.M. Urquiza, Solutions to muscle fiber equations and their long time behaviour, *Nonlinear Anal. RWA* 7 (2006) 535–558.
- [139] M.P. Nash, P.J. Hunter, Computational mechanics of the heart, *J. Elasticity* 61 (2000) 113–141.
- [140] J. Sundnes, S. Wall, H. Osnès, T. Thorvaldsen, A.D. McCulloch, Improved discretisation and linearisation of active tension in strongly coupled cardiac electro-mechanics simulations, *Comput. Methods Biomed. Eng.* 17 (6) (2014) 604–615.
- [141] P. Pathmanathan, S.J. Chapman, D.J. Gavaghan, J.P. Whiteley, Cardiac electromechanics: the effect of contraction model on the mathematical problem and accuracy of the numerical scheme, *Quart. J. Mech. Appl. Math.* 63 (2010) 375–399.
- [142] P. Pathmanathan, C. Ortner, D. Kay, Existence of solutions of partially degenerate visco-elastic problems, and applications to modelling muscular contraction and cardiac electro-mechanical activity, (2013) submitted for publication.
- [143] B. Andreianov, M. Bendahmane, A. Quarteroni, R. Ruiz-Baier, Solvability analysis and numerical approximation of linearized cardiac electromechanics, *Math. Models Methods Appl. Sci.* 25 (05) (2015) 959–993.
- [144] M. Holzer, N. Doelman, T.J. Kaper, Existence and stability of traveling pulses in a reaction–diffusion–mechanics system, *J. Nonlinear Sci.* 23 (2013) 129–177.
- [145] K. Piechór, Reaction–diffusion equation modelling calcium waves with fast buffering in visco-elastic environment, *Arch. Mech.* 64 (5) (2012) 477–509.
- [146] Y. Maday, Analysis of coupled models for fluid–structure interaction of internal flows, in: L. Formaggia, A. Quarteroni, A. Veneziani (Eds.), *Cardiovascular Mathematics*, in: Modeling, Simulation and Applications, vol. 1, Springer, Milan, 2009.
- [147] J.-L. Lions, Quelques méthodes de résolution des problèmes aux limites non linéaires, (1969), Dunod Paris.
- [148] A. Chambolle, B. Desjardins, M.J. Esteban, C. Grandmont, Existence of weak solutions for the unsteady interaction of a viscous fluid with an elastic plate, *J. Math. Fluid Mech.* 7 (3) (2005) 368–404.
- [149] C. Grandmont, Analyse mathématique et numérique de problèmes d’interaction fluide-structure. Application à la modélisation de l’appareil respiratoire, Habilitation à Diriger des Recherches, Université Paris 6, (2009).
- [150] G.N. Gatica, N. Hsiao, S. Meddahi, A residual-based a posteriori error estimator for a two-dimensional fluid-solid interaction problem, *Numer. Math.* 114 (1) (2009) 63–106.
- [151] G.N. Gatica, A. Marquez, S. Meddahi, Analysis of the coupling of lagrange and arnold-falk-winther finite elements for a fluid-solid interaction problem in 3d, *SIAM J. Numer. Anal.* 50 (3) (2012) 1648–1674.
- [152] T. Chacón Rebollo, V. Girault, F. Murat, O. Pironneau, Analysis of a coupled fluid–structure model with applications to hemodynamics, *SIAM J. Numer. Anal.* 54 (2) (2016) 994–1019.
- [153] J.P. Keener, Propagation and its failure in coupled systems of discrete excitable cells, *SIAM J. Appl. Math.* 47 (3) (1987) 556–572.
- [154] M. Bendahmane, R. Bürger, R. Ruiz-Baier, A multiresolution space–time adaptive scheme for the bidomain model in electrocardiology, *Numer. Methods Partial Differential Equations* 26 (6) (2010) 1377–1404.
- [155] P. Colli Franzone, P. Deuflhard, B. Erdmann, J. Lang, L.F. Pavarino, Adaptivity in space and time for reaction–diffusion systems in electrocardiology, *SIAM J. Sci. Comput.* 28 (3) (2006) 942–962.
- [156] S. Krishnamoorthi, M. Sarkar, W.S. Klug, Numerical quadrature and operator splitting in finite element methods for cardiac electrophysiology, *Int. J. Numer. Methods Biomed. Eng.* 29 (11) (2013) 1243–1266.
- [157] S.A. Niederer, E. Kerfoot, A.P. Benson, M.O. Bernabeu, O. Bernus, C. Bradley, E.M. Cherry, R. Clayton, F.H. Fenton, A. Garny, et al., Verification of cardiac tissue electrophysiology simulators using an *N*-version benchmark, *Phil. Trans. R. Soc. A* 369 (1954) (2011) 4331–4351.
- [158] P. Pathmanathan, M.O. Bernabeu, S.A. Niederer, D.J. Gavaghan, D. Kay, Computational modelling of cardiac electrophysiology: explanation of the variability of results from different numerical solvers, *Int. J. Numer. Methods Biomed. Eng.* 28 (8) (2012) 890–903.

- [159] A. Patelli, L. Dedè, T. Lassila, A. Barozzagli, A. Quarteroni, Isogeometric approximation of cardiac electrophysiology models on surfaces, *Mathicse report* 20 (2015).
- [160] D. Kuzmin, M.J. Shashkov, D. Svyatskiy, A constrained finite element method satisfying the discrete maximum principle for anisotropic diffusion problems, *J. Comput. Phys.* 228 (9) (2009) 3448–3463.
- [161] S. Göltepe, S.N.S. Acharya, J. Wong, E. Kuhl, Computational modeling of passive myocardium, *In. J. Numer. Methods Biomed. Engrg.* 27 (2011) 1–12.
- [162] M. Hadjicharalambous, J. Lee, N.P. Smith, D.A. Nordsletten, A displacement-based finite element formulation for incompressible and nearly-incompressible cardiac mechanics, *Comput. Methods Appl. Mech. Engrg.* 274 (2014) 213–236.
- [163] R. Ruiz-Baier, Primal-mixed formulations for reaction–diffusion systems on deforming domains, *J. Comput. Phys.* 299 (2015) 320–338.
- [164] P. Jung, S. Leyendecker, J. Linn, M. Ortiz, A discrete mechanics approach to the Cosserat rod theory—Part I: static equilibria, *Int. J. Numer. Methods Engrg.* 85 (2011) 31–60.
- [165] S. Pezzuto, D. Ambrosi, A. Quarteroni, An orthotropic active-strain model for the myocardium mechanics and its numerical approximation, *Eur. J. Mech. A Solids* 48 (2014) 83–96.
- [166] S. Rossi, Anisotropic modeling of cardiac mechanical activation (Ph.D. thesis), Ecole Polytechnique Fédérale de Lausanne, 2014.
- [167] E.L. Allgower, K. Georg, Introduction to numerical continuation methods, in: *Classics in Applied Mathematics*, SIAM, 2003.
- [168] J. Pitt-Francis, P. Pathmanathan, M.O. Bernabeu, R. Bordas, J. Cooper, A.G. Fletcher, G.R. Mirams, P. Murray, J.M. Osborne, A. Walter, et al., Chaste: a test-driven approach to software development for biological modelling, *Comput. Phys. Commun.* 180 (12) (2009) 2452–2471.
- [169] D.A. Knoll, D.E. Keyes, Jacobian-free Newton-Krylov methods: a survey of approaches and applications, *J. Comput. Phys.* 193 (2) (2004) 357–397.
- [170] V. Shamanskii, A modification of Newton's method, *Ukrainian Math. J.* 19 (1967) 133–138.
- [171] S.C. Eisenstat, H.F. Walker, Choosing the forcing terms in an inexact Newton method, *SIAM J. Sci. Comput.* 17 (1) (1996) 16–32.
- [172] T.J.R. Hughes, L.P. Franca, M. Balestra, A new finite element formulation for computational fluid dynamics: V. Circumventing the Babuška–Brezzi condition: A stable Petrov–Galerkin formulation of the Stokes problem accommodating equal-order interpolations, *Comput. Methods Appl. Mech. Engrg.* 59 (1) (1986) 85–99.
- [173] G. Scovazzi, B. Carnes, X. Zeng, S. Rossi, A simple, stable, and accurate linear tetrahedral finite element for transient, nearly, and fully incompressible solid dynamics: a dynamic variational multiscale approach, *Internat. J. Numer. Methods Engrg.* (2015) <http://dx.doi.org/10.1002/nme.5138>.
- [174] B.P. Lamichhane, E.P. Stephan, A symmetric mixed finite element method for nearly incompressible elasticity based on biorthogonal systems, *Numer. Methods Partial Differential Equations* 28 (4) (2012) 1336–1353.
- [175] F.Y. Liang, S. Takagi, R. Himeno, H. Liu, Biomechanical characterization of ventricular–arterial coupling during aging: A multi-scale model study, *J. Biomech.* 42 (2009) 692–704.
- [176] Y. Shi, Y. Shi, T. Korakianitis, Physiological control of an in-series connected pulsatile VAD: Numerical simulation study, *Comput. Methods Biomed. Engrg.* 14 (11) (2011) 995–1007.
- [177] N. Stergiopoulos, B.E. Westerhof, N. Westerhof, Physical basis of pressure transfer from periphery to aorta: A model-based study, *Am. J. Physiol.* 274 (1998) H1386–H1392.
- [178] P. Moin, Advances in large eddy simulation methodology for complex flows, *Int. J. Heat Fluid Flow* 23 (5) (2002) 710–720.
- [179] S.B. Pope, *Turbulent Flows*, Cambridge University Press, 2000.
- [180] P. Sagaut, *Large Eddy Simulation for Incompressible Flows*, Vol. 3, Springer-Verlag, Berlin, 2000.
- [181] T.J.R. Hughes, G. Scovazzi, L.P. Franca, Multiscale and stabilized methods, in: E. Stein, R. de Borst, T.J.R. Hughes (Eds.), *Encyclopedia of Comput. Mech.*, in: *Computational fluid dynamics*, vol. 3, Wiley Chichester, 2004.
- [182] T.J.R. Hughes, G. Sangalli, Variational multiscale analysis: the fine-scale Green's function, projection, optimization, localization, and stabilized methods, *SIAM J. Numer. Anal.* 45 (2007) 539–557.
- [183] Y. Bazilevs, V.M. Calo, J.A. Cottrell, T.J.R. Hughes, A. Reali, G. Scovazzi, Variational multiscale residual-based turbulence modeling for large eddy simulation of incompressible flows, *Comput. Methods Appl. Mech. Engrg.* 197 (2007) 173–201.
- [184] Y.G. Motlagh, H.T. Ahn, T.J.R. Hughes, V.M. Calo, Simulation of laminar and turbulent concentric pipe flows with the isogeometric variational multiscale method, *Comput. & Fluids* 71 (2013) 146–155.
- [185] R. Codina, J. Principe, O. Guasch, S. Badia, Time dependent subscales in the stabilized finite element approximation of incompressible flow problems, *Comput. Methods Appl. Mech. Engrg.* 196 (21) (2007) 2413–2430.
- [186] A. Quarteroni, *Numerical Models for Differential Problems*, second ed., Springer-Verlag, Berlin, 2014.
- [187] J. Chung, G.M. Hulbert, A time integration algorithm for structural dynamics with improved numerical dissipation: The generalized- α method, *J. Appl. Mech.* 60 (2) (1993) 371–375.
- [188] K.E. Jansen, C.H. Whiting, G.M. Hulbert, A generalized- α method for integrating the filtered Navier–Stokes equations with a stabilized finite element method, *Comput. Methods Appl. Mech. Engrg.* 190 (3–4) (2000) 305–319.
- [189] D. Forti, L. Dedè, Semi-implicit BDF time discretization of the Navier–Stokes equations with VMS-LES modelling in a high performance computing framework, *Comput. Fluids* 117 (2015) 168–182.
- [190] Y. Bazilevs, K. Takizawa, T.E. Tazdalar, *Computational Fluid-Structure Interaction: Methods and Applications*, Wiley, 2013.
- [191] M. Caruel, R. Chabiñok, P. Moireau, Y. Lecarpentier, D. Chapelle, Dimensional reduction of cardiac models for effective validation and calibration, in: S. Ourselin, D. Rueckert, N. Smith (Eds.), *Functional Imaging and Modeling of the Heart*, Springer Berlin Heidelberg, 2013, pp. 259–267.
- [192] A. Di Blasio, Coupled mathematical models for heart integration: a stability study (Master's thesis), EPFL, 2014.
- [193] R.R. Aliev, A.V. Panfilov, A simple two-variable model of cardiac excitation, *Chaos Solitons Fractals* 7 (3) (1996) 293–301.
- [194] M.P. Nash, A.V. Panfilov, Electromechanical model of excitable tissue to study reentrant cardiac arrhythmias, *Prog. Biophys. Mol. Biol.* 85 (2) (2004) 501–522.

- [195] M.E. Marsh, S.T. Ziaratgahi, R.J. Spiteri, The secrets to the success of the Rush-Larsen method and its generalizations, *IEEE Trans. Biomed. Eng.* 59 (9) (2012) 2506–2515.
- [196] J. Sundnes, R. Artebrant, O. Skavhaug, A. Tveito, A second-order algorithm for solving dynamic cell membrane equations, *IEEE Trans. Biomed. Eng.* 56 (10) (2009) 2546–2548.
- [197] U.M. Ascher, S.J. Ruuth, B.T.R. Wetton, Implicit-explicit methods for time-dependent partial differential equations, *SIAM J. Numer. Anal.* 32 (3) (1995) 797–823.
- [198] H. Elman, V.E. Howle, J. Shadid, R. Shuttleworth, R. Tuminaro, A taxonomy and comparison of parallel block multi-level preconditioners for the incompressible Navier–Stokes equations, *J. Comput. Phys.* 227 (3) (2008) 1790–1808.
- [199] A. Quarteroni, F. Saleri, A. Veneziani, Factorization methods for the numerical approximation of Navier–Stokes equations, *Comput. Methods Appl. Mech. Engrg.* 188 (1) (2000) 505–526.
- [200] S. Badia, A. Quaini, A. Quarteroni, Splitting methods based on algebraic factorization for fluid–structure interaction, *SIAM J. Sci. Comput.* 30 (4) (2008) 1778–1805.
- [201] P. Crosetto, S. Deparis, G. Fourestey, A. Quarteroni, Parallel algorithms for fluid–structure interaction problems in haemodynamics, *SIAM J. Sci. Comput.* 33 (4) (2011) 1598–1622.
- [202] H.G. Matthies, J. Steindorf, Partitioned strong coupling algorithms for fluid–structure interaction, *Comput. Struct.* 81 (8) (2003) 805–812.
- [203] T.F. Chan, T.P. Mathew, Domain decomposition algorithms, *Acta Numer.* 3 (1994) 61–143.
- [204] A. Toselli, O. Widlund, *Domain Decomposition Methods: Algorithms and Theory*, Springer, Berlin, 2005.
- [205] O. Axelsson, *Iterative Solution Methods*, Cambridge University Press, 1996.
- [206] R.S. Varga, *Matrix Iterative Analysis*, Prentice Hall, Englewood Cliffs, NJ, 1962.
- [207] D.E. Keyes, L.C. McInnes, C. Woodward, W. Gropp, E. Myra, M. Pernice, J. Bell, J. Brown, A. Clo, J. Connors, et al., Multiphysics simulations: Challenges and opportunities, *Int. J. High Perform. Comput. Appl.* 27 (1) (2013) 4–83.
- [208] U. Kötter, M. Gee, Ch. Förster, A. Comerford, W.A. Wall, Coupling strategies for biomedical fluid–structure interaction problems, *Int. J. Numer. Methods Biomed. Eng.* 26 (3–4) (2010) 305–321.
- [209] J.D. Bayer, R.C. Blake, G. Plank, N.A. Trayanova, A novel rule-based algorithm for assigning myocardial fiber orientation to computational heart models, *Ann. Biomed. Eng.* 40 (10) (2012) 2243–2254.
- [210] J. Wong, E. Kuhl, Generating fibre orientation maps in human heart models using Poisson interpolation, *Comput. Methods Biomed. Eng.* 17 (11) (2014) 1217–1226.
- [211] A. Nagler, C. Bertoglio, M. Gee, W. Wall, Personalization of cardiac fiber orientations from image data using the unscented Kalman filter, in: S. Ourselin, D. Rueckert, N. Smith (Eds.), *Functional Imaging and Modeling of the Heart*, Springer, Berlin, Heidelberg, 2013, pp. 132–140.
- [212] F. Sahli Costabal, D.E. Hurtado, E. Kuhl, Generating Purkinje networks in the human heart, *J. Biomech.* (2015) in press <http://dx.doi.org/10.1016/j.jbiomech.2015.12.025>.
- [213] P. Pathmanathan, G.R. Mirams, J. Southern, J.P. Whiteley, The significant effect of the choice of ionic current integration method in cardiac electro-physiological simulations, *Int. J. Numer. Methods Biomed. Eng.* 27 (11) (2011) 1751–1770.
- [214] B.J. Caldwell, M.L. Trew, G.B. Sands, D.A. Hooks, I.J. LeGrice, B.H. Smaill, Three distinct directions of intramural activation reveal nonuniform side-to-side electrical coupling of ventricular myocytes, *Circ.: Arrythm. Electrophysiol.* 2 (4) (2009) 433–440.
- [215] N. Walker, F. Burton, S. Kettlewell, G. Smith, S. Cobbe, Mapping of epicardial activation in a rabbit model of chronic myocardial infarction, *J. Cardiovasc. Electrophysiol.* 18 (8) (2007) 862–868.
- [216] F.H. Fenton, S.J. Evans, H.M. Hastings, Memory in an excitable medium: a mechanism for spiral wave breakup in the low-excitability limit, *Phys. Rev. Lett.* 83 (1999) 3964–3967.
- [217] F.H. Fenton, A. Karma, Vortex dynamics in three-dimensional continuum myocardium with fiber rotation: Filament instability and fibrillation, *Chaos* 8 (1998) 20–47.
- [218] M. Dupraz, S. Filippi, A. Gizzi, A. Quarteroni, R. Ruiz-Baier, Finite element and finite volume-element simulation of pseudo-ECGs and cardiac alternans, *Math. Methods Appl. Sci.* 38 (6) (2015) 1046–1058.
- [219] G. Plank, L. Zhou, J.L. Greenstein, S. Cortassa, R.L. Winslow, B. O'Rourke, N.A. Trayanova, From mitochondrial ion channels to arrhythmias in the heart: computational techniques to bridge the spatio-temporal scales, *Philos. Trans. R. Soc. Lond. Ser. A Math. Phys. Eng. Sci.* 366 (1879) (2008) 3381–3409.
- [220] T. Dickopf, D. Krause, R. Krause, M. Potse, Design and analysis of a lightweight parallel adaptive scheme for the solution of the monodomain equation, *SIAM J. Sci. Comput.* 36 (2) (2014) C163–C189.
- [221] E.M. Cherry, H.S. Greenside, C.S. Henriquez, A space–time adaptive method for simulating complex cardiac dynamics, *Phys. Rev. Lett.* 84 (2000) 1343–1346.
- [222] E.M. Cherry, F.H. Fenton, Effects of boundaries and geometry on the spatial distribution of action potential duration in cardiac tissue, *J. Theoret. Biol.* 285 (2011) 164–176.
- [223] J.P. Whiteley, Physiology driven adaptivity for the numerical solution of the bidomain equations, *Ann. Biomed. Eng.* 35 (9) (2007) 1510–1520.
- [224] R.T. Shield, Inverse deformation results in finite elasticity, *Z. Angew. Math. Phys.* 18 (4) (1967) 490–500.
- [225] P. Chadwick, Applications of an energy–momentum tensor in non-linear elasto-statics, *J. Elasticity* 5 (3–4) (1975) 249–258.
- [226] M.W. Gee, Ch. Förster, W.A. Wall, A computational strategy for prestressing patient-specific biomechanical problems under finite deformation, *Int. J. Numer. Methods Biomed. Eng.* 26 (1) (2010) 52–72.
- [227] M.W. Gee, C. Reeps, H.H. Eckstein, W.A. Wall, Prestressing in finite deformation abdominal aortic aneurysm simulation, *J. Biomech.* 42 (11) (2009) 1732–1739.
- [228] N. Lanconelli, S. Masetti, P. Nardinocchi, L. Teresi, P.E. Puddu, C. Torromeo, V. Giglio, Strain analysis of cardiac tissues from 3D ultrasound images using snakes and speckle tracking, *J. Mech. Med. Biol.* 15 (2015) 1540012.

- [229] L. Asner, M. Hadjicharalambous, R. Chabiniok, D. Peresutti, E. Sammut, J. Wong, G. Carr-White, P. Chowienczyk, J. Lee, A. King, N. Smith, R. Razavi, D. Nordsletten, Estimation of passive and active properties in the human heart using 3D tagged MRI, *Biomech. Model. Mechanobiol.* (2015) in press <http://dx.doi.org/10.1007/s10237-015-0748-z>.
- [230] A. Pandolfi, G.A. Holzapfel, Three-dimensional modeling and computational analysis of the human cornea considering distributed collagen fibril orientations, *J. Biomech. Eng.* 130 (6) (2008) 061006.
- [231] S. Land, et al., Verification of cardiac mechanics software: benchmark problems and solutions for testing active and passive material behaviour, *Proc. R. Soc. Lond. Ser. A Math. Phys. Eng. Sci.* 471 (2184) (2015).
- [232] S. Deparis, D. Forti, A. Quarteroni, A rescaled localized radial basis function interpolation on non-Cartesian and nonconforming grids, *SIAM J. Sci. Comput.* 36 (6) (2014) A2745–A2762.
- [233] T.P. Usyk, I.J. LeGrice, A.D. McCulloch, Computational model of three-dimensional cardiac electromechanics, *Comput. Vis. Sci.* 4 (4) (2002) 249–257.
- [234] J.L. Palladino, J.P. Mulier, A. Noordergraaf, Defining ventricular elastance, *Proc. IEEE Eng. Med. Biol. Soc.* (1998) 383–386.
- [235] R.C. Kerckhoffs, M.L. Neal, Q. Gu, J.B. Bassingthwaite, J.H. Omens, A.D. McCulloch, Coupling of a 3D finite element model of cardiac ventricular mechanics to lumped systems models of the systemic and pulmonic circulation, *Ann. Biomed. Eng.* 35 (1) (2007) 1–18.
- [236] S. Clay, K. Alfaikah, A. Radjenovic, T. Jones, J.P. Ridgway, Normal range of human left ventricular volumes and mass using steady state free precession MRI in the radial long axis orientation, *Magn. Reson. Mater. Phys.* 19 (1) (2006) 41–45.
- [237] A.M. Maceira, S.K. Prasad, M. Khan, D.J. Pennell, Normalized left ventricular systolic and diastolic function by steady state free precession cardiovascular magnetic resonance, *J. Cardiov. Magn. Reson.* 8 (3) (2006) 417–426.
- [238] O. Rousseau, Geometrical modeling of the heart (Ph.D. thesis), Université d’Ottawa, 2010.
- [239] A. Evangelista, P. Nardinocchi, P.E. Puddu, L. Teresi, C. Torromeo, V. Varano, Torsion of the human left ventricle: Experimental analysis and computational modelling, *Prog. Biophys. Mol. Biol.* 107 (2011) 112–121.
- [240] K. Lekadir, B. Ghafaryasl, E. Muñoz-Moreno, C. Butakoff, C. Hoogendoorn, A.F. Frangi, Predictive modeling of cardiac fiber orientation using the Knutsson mapping, in: *Medical Image Computing and Computer-Assisted Intervention—MICCAI*, Springer, Berlin, Heidelberg, 2011, pp. 50–57.
- [241] F. Zannad, E. Huvelle, K. Dickstein, D.J. van Veldhuisen, C. Stellbrink, L. Kober, S. Cazeau, P. Ritter, A.P. Maggioni, R. Ferrari, P. Lechat, Left bundle branch block as a risk factor for progression to heart failure, *Eur. J. Heart Fail.* 9 (1) (2007) 7–14.
- [242] J. Constantino, Y. Hu, N.A. Trayanova, A computational approach to understanding the cardiac electromechanical activation sequence in the normal and failing heart, with translation to the clinical practice of CRT, *Prog. Biophys. Mol. Biol.* 110 (2) (2012) 372–379.
- [243] M. Potse, D. Krause, L. Bacharova, R. Krause, F.W. Prinzen, A. Auricchio, Similarities and differences between electrocardiogram signs of left bundle-branch block and left-ventricular uncoupling, *Europace* 14 (suppl 5) (2012) v33–v39.
- [244] R.C. Kerckhoffs, A.D. McCulloch, J.H. Omens, L.J. Mulligan, Effects of biventricular pacing and scar size in a computational model of the failing heart with left bundle branch block, *Med. Image Anal.* 13 (2) (2009) 362–369.
- [245] L. Galeotti, P.M. van Dam, Z. Loring, D. Chan, D.G. Strauss, Evaluating strict and conventional left bundle branch block criteria using electrocardiographic simulations, *Europace* 15 (12) (2013) 1816–1821.
- [246] E. Burman, M.A. Fernández, P. Hansbo, Continuous interior penalty finite element method for Oseen’s equations, *SIAM J. Numer. Anal.* 44 (3) (2006) 1248–1274.
- [247] E.J. Vigmond, C. Clements, Construction of a computer model to investigate sawtooth effects in the Purkinje system, *IEEE Trans. Biomed. Eng.* 54 (3) (2007) 389–399.
- [248] D. Chapelle, J.-F. Gerbeau, J. Sainte-Marie, I.E. Vignon-Clementel, A poroelastic model valid in large strains with applications to perfusion in cardiac modeling, *Comput. Mech.* 46 (1) (2010) 91–101.
- [249] A.N. Cookson, J. Lee, C. Michler, R. Chabiniok, E. Hyde, D.A. Nordsletten, M. Sinclair, M. Siebes, N.P. Smith, A novel porous mechanical framework for modelling the interaction between coronary perfusion and myocardial mechanics, *J. Biomech.* 45 (5) (2012) 850–855.
- [250] C. Michler, A.N. Cookson, R. Chabiniok, E. Hyde, J. Lee, M. Sinclair, T. Sochi, A. Goyal, G. Vigueras, D.A. Nordsletten, et al., A computationally efficient framework for the simulation of cardiac perfusion using a multi-compartment Darcy porous-media flow model, *Int. J. Numer. Methods Biomed. Eng.* 29 (2) (2013) 217–232.
- [251] H.J. Kim, K.E. Jansen, C.A. Taylor, Incorporating autoregulatory mechanisms of the cardiovascular system in three-dimensional finite element models of arterial blood flow, *Ann. Biomed. Eng.* 38 (7) (2010) 2314–2330.
- [252] S. Göktepe, O.J. Abilez, K.K. Parker, E. Kuhl, A multiscale model for eccentric and concentric cardiac growth through sarcomerogenesis, *J. Theoret. Biol.* 265 (3) (2010) 433–442.
- [253] D. Chapelle, A. Collin, J.-F. Gerbeau, A surface-based electrophysiology model relying on asymptotic analysis and motivated by cardiac atria modeling, *Math. Models Methods Appl. Sci.* 23 (14) (2013) 2749–2776.
- [254] M.A. Colman, S.J. Castro, E.A. Perez Alday, J.C. Hancox, C. Garratt, H. Zhang, Recent progress in multi-scale models of the human atria, *Drug Discov. Today Dis. Models* 14 (2014) 23–32.
- [255] C. Tobón, C.A. Ruiz-Villa, E. Heidenreich, L. Romero, F. Hornero, A three-dimensional human atrial model with fiber orientation. Electrograms and arrhythmic activation patterns relationship, *PLoS ONE* 8 (2013) 1–13.
- [256] M. Boulakia, S. Cazeau, M.A. Fernández, J.-F. Gerbeau, N. Zemzemi, Mathematical modeling of electrocardiograms: a numerical study, *Ann. Biomed. Eng.* 38 (3) (2010) 1071–1097.
- [257] R.H. Clayton, A.V. Holden, Computational framework for simulating the mechanisms and ECG of re-entrant ventricular fibrillation, *Physiol. Meas.* 23 (4) (2002) 707–726.
- [258] A. Tagliabue, L. Dedé, A. Quarteroni, Fluid dynamics of an idealized left ventricle: the extended Nitsche’s method for the treatment of heart valves as mixed time varying boundary conditions, *Mathicse report* 31 (2015).
- [259] A. Tagliabue, Mathematical and numerical modelling of blood flow in an idealized left ventricle (Ph.D. thesis), Politecnico di Milano, 2016.
- [260] R. FitzHugh, Theoretical effect of temperature on threshold in the Hodgkin–Huxley nerve model, *J. Gen. Physiol.* 49 (5) (1966) 989–1005.

- [261] B. Hille, Ion Channels of Excitable Membranes, Sinauer Associates, Inc., 2001.
- [262] V. Vedula, J.-H. Seo, A.C. Lardo, R. Mittal, Effect of trabeculae and papillary muscles on the hemodynamics of the left ventricle, *Theoret. Comput. Fluid Dyn.* 30 (1) (2016) 3–21.
- [263] D. Krause, T. Dickopf, M. Potse, R. Krause, Towards a large-scale scalable adaptive heart model using shallow tree meshes, *J. Comput. Phys.* 298 (1) (2015) 79–94.
- [264] D.F. Richards, J.N. Glosli, E.W. Draeger, A.A. Mirin, B. Chan, J.L. Fattebert, et al., Towards real-time simulation of cardiac electrophysiology in a human heart at high resolution, *Comput. Methods Biomed. Engrg.* 16 (7) (2013) 802–805.
- [265] M. Vázquez, R. Arís, J. Aguado-Sierra, G. Houzeaux, A. Santiago, M. López, P. Córdoba, M. Rivero, J.C. Cajas, Alya Red CCM: HPC-Based Cardiac Computational Modelling, in: J. Klapp, G. Ruiz Chavarría, A. Medina Ovando, A. López Villa, L.D.G. Sigalotti (Eds.), *Selected Topics of Computational and Experimental Fluid Mechanics*, Springer International Publishing, 2015, pp. 189–207.
- [266] M.A. Islam, A. Murthy, E. Bartocci, E.M. Cherry, F.H. Fenton, J. Glimm, S.A. Smolka, R. Grosu, Model-order reduction of ion channel dynamics using approximate bisimulation, *Theoret. Comput. Sci.* 599 (2015) 34–46.
- [267] C.J. Arthurs, M.J. Bishop, D. Kay, Efficient simulation of cardiac electrical propagation using high order finite elements, *J. Comput. Phys.* 231 (10) (2012) 3946–3962.
- [268] C.J. Arthurs, M.J. Bishop, D. Kay, Efficient simulation of cardiac electrical propagation using high order finite elements II: Adaptive p -version, *J. Comput. Phys.* 253 (15) (2013) 443–470.
- [269] K.P. Vincent, M.J. Gonzales, A.K. Gillette, C.T. Villongco, S. Pezzuto, J.H. Omens, M.J. Holst, A.D. McCulloch, High-order finite element methods for cardiac monodomain simulations, *Front Physiol.* 6 (2015) 00217.
- [270] V. Gurev, P. Pathmanathan, J.L. Fattebert, H.F. Wen, J. Magerlein, R.A. Gray, D.F. Richards, J.J. Rice, A high-resolution computational model of the deforming human heart, *Biomech. Model. Mechanobiol.* 14 (2015) 829–849.
- [271] S. Marchesseau, H. Delingette, M. Serresant, R. Cabrera-Lozoya, C. Tobon-Gomez, P. Moireau, R.F. Ventura, K. Lekadir, A. Hernandez, M. Garreau, E. Donal, Personalization of a cardiac electromechanical model using reduced order unscented Kalman filtering from regional volumes, *Med. Image Anal.* 17 (7) (2013) 816–829.
- [272] M. Serresant, R. Chabinik, P. Chinchapatnam, T. Mansi, F. Billet, P. Moireau, J.M. Peyrat, K. Wong, J. Relan, K. Rhode, M. Ginks, Patient-specific electromechanical models of the heart for the prediction of pacing acute effects in CRT: A preliminary clinical validation, *Med. Image Anal.* 16 (1) (2012) 201–215.
- [273] A. Aggarwal, V.S. Aguilar, C.H. Lee, G. Ferrari, J.H. Gorman, R.C. Gorman, M.S. Sacks, Patient-specific modeling of heart valves: from image to simulation, in: S. Ourselin, D. Rueckert, N. Smith (Eds.), *Functional Imaging and Modeling of the Heart*, Springer, Berlin, Heidelberg, 2013, pp. 141–149.
- [274] A. Drach, A.H. Khalighi, F.M. ter Huurne, C.H. Lee, C. Bloodworth, E.L. Pierce, M.O. Jensen, A.P. Yoganathan, M.S. Sacks, Population-averaged geometric model of mitral valve from patient-specific imaging data, *J. Med. Devices* 9 (3) (2015) 030952.
- [275] M. Fedele, A patient-specific aortic valve model based on moving resistive immersed surfaces (Master thesis), Politecnico di Milano, 2014.
- [276] A. Laadhari, A. Quarteroni, Numerical modeling of heart valves using resistive Eulerian surfaces, *Int. J. Numer. Methods Biomed. Eng.* 32 (5) (2016) e02743.
- [277] S. Morganti, F. Auricchio, D.J. Benson, F.I. Gambarin, S. Hartmann, T.J.R. Hughes, A. Reali, Patient-specific isogeometric structural analysis of aortic valve closure, *Comput. Methods Appl. Mech. Engrg.* 284 (2015) 508–520.